12-2008

Modeling and Control of Piezoactive Micro and Nano Systems

Saeid Bashash
Clemson University, saeid_bashash@yahoo.com

MODELING AND CONTROL OF PIEZOACTIVE MICRO AND NANO SYSTEMS

A Dissertation
Presented to
the Graduate School of
Clemson University

In Partial Fulfillment
of the Requirements for the Degree
Doctor of Philosophy
Mechanical Engineering

---

by
Saeid Bashash
December 2008

Accepted by
Dr. Nader Jalili, Committee Chair
Dr. Thomas R. Kurfess
Dr. Darren M. Dawson
Dr. Ardalan Vahidi

ABSTRACT

Piezoelectrically-driven (piezoactive) systems such as nanopositioning platforms, scanning probe microscopes, and nanomechanical cantilever probes are advantageous devices enabling molecular-level imaging, manipulation, and characterization in disciplines ranging from materials science to physics and biology. Such emerging applications require precise modeling, control and manipulation of objects, components and subsystems ranging in sizes from few nanometers to micrometers. This dissertation presents a comprehensive modeling and control framework for piezoactive micro and nano systems utilized in various applications.

The development of a precise memory-based hysteresis model for feedforward tracking as well as a Lyapunov-based robust-adaptive controller for feedback tracking control of nanopositioning stages are presented first. Although hysteresis is the most degrading factor in feedforward control, it can be effectively compensated through a robust feedback control design. Moreover, an adaptive controller can enhance the performance of closed-loop system that suffers from parametric uncertainties at high-frequency operations. Comparisons with the widely-used PID controller demonstrate the effectiveness of the proposed controller in tracking of high-frequency trajectories. The proposed controller is then implemented in a laser-free Atomic Force Microscopy (AFM) setup for high-speed and low-cost imaging of surfaces with micrometer and nanometer scale variations. It is demonstrated that the developed AFM is able to produce high-quality images at scanning frequencies up to 30 Hz, where a PID controller is unable to present acceptable results.

To improve the control performance of piezoactive nanopositioning stages in tracking of time-varying trajectories with frequent stepped discontinuities, which is a common problem in SPM systems, a supervisory switching controller is designed and integrated with the proposed robust adaptive controller. The controller switches between two control modes, one mode tuned for stepped trajectory tracking and the other one tuned for continuous trajectory tracking. Switching conditions and compatibility conditions of the control inputs in switching instances are derived and analyzed. Experimental implementation of the proposed switching controller indicates significant improvements of control performance in tracking of time-varying discontinuous trajectories for which single-mode controllers yield undesirable results.

Distributed-parameters modeling and control of rod-type solid-state actuators are then studied to enable accurate tracking control of piezoactive positioning systems in a wide frequency range including several resonant frequencies of system. Using the extended Hamilton's principle, system partial differential equation of motion and its boundary conditions are derived. Standard vibration analysis techniques are utilized to formulate the truncated finite-mode state-space representation of the system. A new state-space controller is then proposed for asymptotic output tracking control of system. Integration of an optimal state-observer and a Lyapunov-based robust controller are presented and discussed to improve the practicability of the proposed framework. Simulation results demonstrate that distributed-parameters modeling and control is inevitable if ultra-high bandwidth tracking is desired.

The last part of the dissertation, presents new developments in modeling and system identification of piezoelectrically-driven Active Probes as advantageous nanomechanical cantilevers in various applications including tapping mode AFM and biosensors. Due to the discontinuous cross-section of Active Probes, a general framework is developed and presented for multiple-mode vibration analysis of system. Application in precise pico-gram scale mass detection is then presented using frequency-shift method. This approach can benefit the characterization of DNA solutions or other biological species for medical applications.

DEDICATION

I dedicate this work to my dear family for their unconditional kindness and to all my dear friends for their continuous support.

ACKNOWLEDGEMENTS

I sincerely thank my advisor, Dr. Nader Jalili for his continuous support and guidance during my Masters and PhD studies in every aspect. I truly think that these four and half years I spent as his student have brought in me many wonderful qualities. The helpful suggestions from my advisory committee members, Dr. Darren Dawson, Dr. Thomas Kurfess and Dr. Ardalan Vahidi and the financial supports through National Science Foundation CAREER Award program (grant # CMMI–0238987) and MRI Program (grant # CMMI-0619739) are greatly appreciated as well.

I would also like to truly thank my fellow labmates and major collaborators, Dr. Amin Salehi-Khojin, Mr. Reza Saeidpourazar, Mr. Kushan Vora, Mr. Calvin Bradley and Dr. Seyed Nima Mahmoodi at Clemson University SSNEMS Laboratory. Special thanks to Dr. Maren Müller and Dr. Rudieger Berger from Max Planck Institute for Polymer Research in Germany, who directly contributed to this dissertation, Mr. Gary Lee Thompson and Dr. Alexey Vertegel from Clemson University Department of Bioengineering, Mr. Philip Evans and Dr. Marcelo Dapino from Ohio State University Department of Mechanical Engineering, and Dr. Beshah Ayalew, Dr. Mohammad Daqaq, Mr. Peiman Mossadegh and Mr. Joshua Tarbutton, my other colleagues at Clemson University Department of Mechanical Engineering whose accompany helped me significantly to develop my research and expand my knowledge in different aspects.

TABLE OF CONTENTS

Page

Page

Table of Contents (Continued)

Page

LIST OF FIGURES

Page

Page

Page

Page

List of Figures (Continued)

Page

List of Figures (Continued)

Page

Page

Page

LIST OF TABLES

Page

CHAPTER ONE

INTRODUCTION AND OVERVIEW

1.1. Introduction

The discovery of piezoelectricity over a century ago has now enabled the extensive growth of state-of-the-art technologies in demanding areas such as molecular and atomic level imaging, manipulation and instrumentation. Piezoactive micro and nano systems are referred to a class of dynamic systems driven by piezoelectric materials being able to generate controlled motions up to several millimeters with micrometer and nanometer resolutions. From engineering perspective, an application can only lead to meaningful results if a certain level of precision can be acquired from its subsystems. This has attracted the attention of numerous research groups and organizations worldwide with the interest of piezoactive systems toward multidisciplinary research on the subjects of material processing and property enhancement, design improvement and manufacturing, and system modeling and precision control. The focus of this work is on the modeling and control aspects of piezoactive micro and nano systems which suffer from hysteresis and creep nonlinearities in feedforward control, and parametric uncertainties and dynamical effects in both feedforward and feedback schemes. In the following sections, brief history of piezoelectricity, molecular structure of piezoelectric materials, potential applications of piezoactive system and their substantial research challenges are described in further detail.

1.1.1. History of Piezoelectricity

Piezoelectricity is referred to phenomenon in particular solid-state materials which demonstrate a coupling between their electrical, mechanical, and thermal states generated by applying mechanical stress to dielectric crystals. The word "piezo" originates from a Greek word meaning for pressure. The first experimental demonstration of a connection between the macroscopic piezoelectric phenomenon and the crystallographic structure was published in 1880 by Curie brothers, Pierre and Jacques [1]. They discovered that when subjected to a mechanical pressure, the crystals become electrically polarized; tension and compression generates voltages of opposite polarity, and proportional to the applied force. Later, they also verified that an electrical field applied to the crystal would lead to a deformation of the material. This effect was referred to as the *inverse piezo* effect.

In 1893, Kelvin made a significant contribution to piezoelectricity by presenting analogy models and laying out some of the basic framework that led to the modern theory of piezoelectricity [2]. After this discovery, it took several decades to utilize the piezoelectric phenomenon for practical applications. The first commercial applications were ultrasonic submarine detectors developed during World War I. After the end of World War II, barium titanate oxide ($BaTiO_3$) ceramic was first produced and by the early 1950s was well established as a piezoelectric transducer material [3]. In 1954, lead zirconate titanate ($PbZrTiO_3$–$PbTiO_3$) or PZT ceramics were developed and replaced the barium titanate in all fields of piezoelectric applications. Today, PZT ceramics are the most widely used of all ceramic materials because of their excellent properties [4].

Much of the work carried out from the 1960s to present has been in developing applications for PZT materials (such as in ceramic capacitors). However, research continues into the development of new materials with exciting potential as piezoelectrics. For example, in 1997 Grupp and Goldman found a giant piezoelectric effect in strontium titanate ($SrTiO_3$) at very low temperatures [5], or recently the piezoelectricity in boron nitride nanotubes [6, 7].

1.1.2. Structure of Piezoceramic Materials [8]

Piezoelectric ceramics are considered as a mass of minute crystals. They have a tetragonal shape very close to cubic, and obey the general formula $A^{2+}B^{4+}O_3^{2-}$, in which *A* denotes a large divalent metal ion such as lead or barium, *B* denotes a tetravalent metal ion such as zirconium or titanium, and *O* denotes oxygen. A piezoelectric ceramic is prepared by mixing specific proportions of fine powders of the component metal oxides and then, heating up to form a uniform powder. The powder is mixed with an organic binder, and then formed into desired shape such as disc, rod, and plate. The elements are heated up in a specific temperature for a certain time, during which the particles sinter and form a dense crystalline structure. The elements are then cooled, trimmed and shaped into their final configuration.

There is a certain temperature known as the Curie point above which these crystals exhibit a simple symmetrical cubic shape as shown in Figure 1.1(a), this structure is centrosymmetric and does not contain dipoles because the positive and negative charges site coincide. However, blow the Curie point the crystals take on the tetragonal shape as shown in Figure 1.1(b), in which positive and negative charges site no longer coincide. Therefore, each unit represents a built-in electric dipole, which is a desirable property of the piezoelectric ceramics. Such materials are labeled ferroelectric because of their similar electrical behavior in analogy with magnetic behavior of ferromagnetic materials.

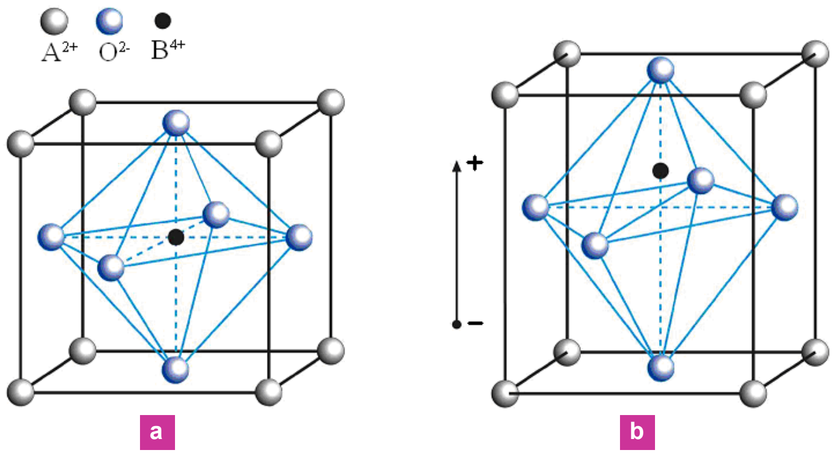

Figure 1.1. Piezoelectric crystal elementary cell: (a) Cubic lattice above Curie temperature, and (b) tetragonal lattice below Curie temperature [8].

The dipoles are not primarily in the same orientation throughout the material. Neighboring dipoles align to each other to make regions of local alignment known as *Weiss* domains. These domains are randomly oriented, and primarily, the material does not exhibit overall polarization or piezoelectric effect. However, it is possible to make the material piezoelectric by exposing it to a strong field at a temperature slightly below the Curie point. This will make the dipoles to be aligned in the direction of the applied field. Due to the ferroelectric property, dipoles approximately maintain their orientation after the electric field is removed. This polling treatment gives the material so-called *remanent* polarization and permanent deformation. Figure 1.2 depicts the electric diploes before, during, and after the polarization.

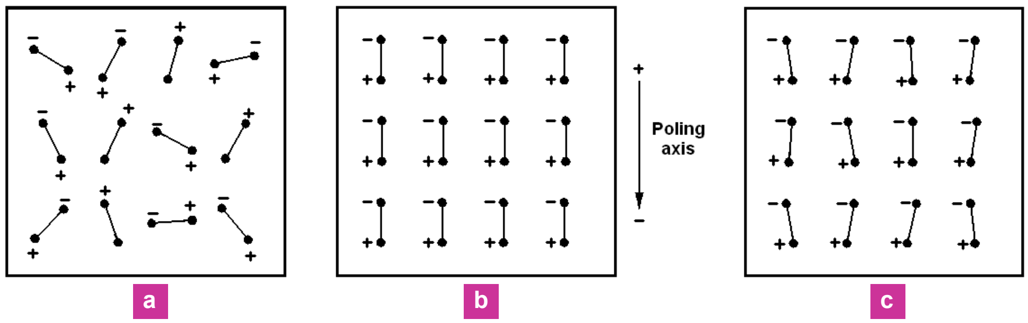

Figure 1.2. Electric dipoles in Weiss domains: (a) before polarization, (b) during polarization, and (c) after polarization.

1.1.3. Piezoactive Micro and Nanopositioning Stages

Piezoactive stages typically consist of a stack of many layers of electro-active solid-state piezoelectric ceramics, alternatively connected to the positive and negative terminals of a voltage source, as shown in Figure 1.3(a). They have very fast response and repeatable nanometer and sub-nanometer motion at high frequencies, because their motion is derived through solid state crystals. There are no moving parts, and no "stick-slip" effect occurs and therefore, they present unlimited resolution in theory, making them advantageous tools for micro/nano-scale metrology and manipulation applications. On the other hand, piezoactive stages can be designed to move heavy loads up to several tons, however, they are very sensitive to pulling forces. In order to reduce such sensitivity, they are internally preloaded with spring configuration as shown in Figure 1.3(b).

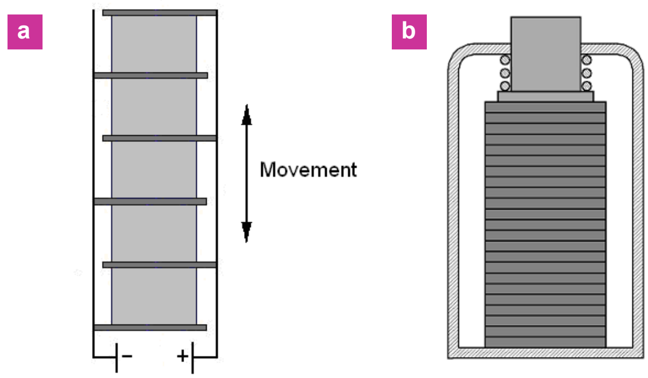

Figure 1.3. Structure of piezoactive positioning stages: (a) piezoelectric ceramics separated with metallic electrodes, and (b) stack preloaded with spring.

A typical piezoactive stack stage is comprised of hundreds of piezoceramic disks with thickness on the order of a hundred microns. Piezoactive stages can achieve a strain on the order of 1/1000 (0.1%) and the total displacement of the stage is determined as the superposition of each individual ceramic layer elongation. For example, a 100 mm long stack can expand up to 100 micrometers, by applying the maximum allowable field. However, there exist several amplification methods to increase the stage displacement range by a factor of 2 to 20. To keep the sub-nanometer resolution, friction-free flexures are utilized. Examples of such mechanisms are shown in Figure 1.4.

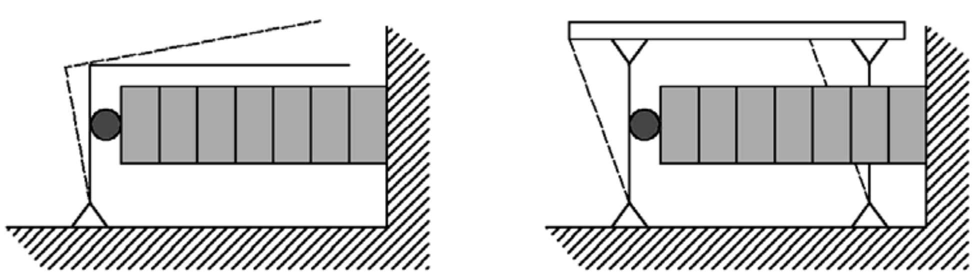

Figure 1.4. Flexural mechanisms for amplification of piezoelectric actuator displacement [8].

1.1.4. Piezoactive Nano Mechanical Cantilever Probes

Recently, NanoMechanical Cantilevers (NMCs) have been extensively utilized in Atomic Force Microscopy (AFM) and ultrasmall mass sensors in various applications from biological sciences to chemistry and physics [9-12]. The sensitivity of the NMC resonant frequencies to an added mass can be utilized to measure the amount of that mass. In order to enhance the sensitivity and resolution of dynamic mode measurement at pico-gram or smaller levels, the piezoactive NMCs, the so-called “Active Probes” can be a promising alternative for the replacement of commonly used base excited NMC sensors. Since the Active Probe is covered by a uniformly distributed piezoelectric layer on the top surface (Figure 1.5), the cantilever can be actuated with higher amplitude and uniformity when compared to based-excited systems. This results in higher resolution of frequency shifts as a result of added tiny mass to the probe. Additionally, it is possible to operate the Active Probes in self-sensing mode in order to obtain portable NMC-based mass detectors [11]. In this approach, the same piezoelectric patch layer used for probe actuation is utilized to detect the resonant frequencies.

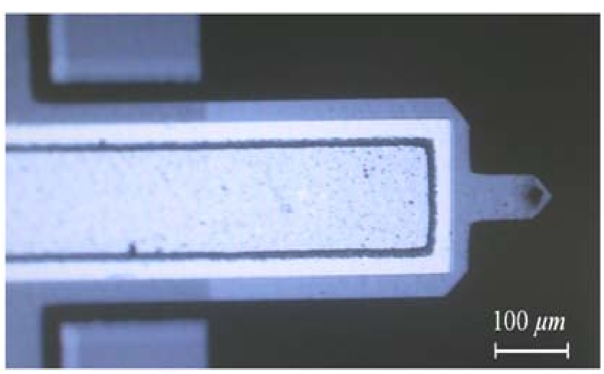

Figure 1.5. Piezoactive NMC beam with cross-sectional discontinuity.

Nevertheless, NMC Active Probes suffer from the cross-sectional discontinuities due to the piezoelectric layer attachment and the cross sectional step the tip zone. This would necessitate using discontinuous beam theory in the analysis and modeling such systems.

1.1.5. Applications of Piezoactive Systems

Piezoelectric ceramics can be utilized in four general applications: generators, sensors, transducers, and actuators. As generators, they covert mechanical impulse or pressure into electrical power that could be utilized as spark igniter systems or power harvesting applications [13, 14]. As sensors, they convert the mechanical force or movement into a proportional electric signal that could be used as acceleration and pressure sensors [15, 16]. When operated in high frequencies (>10 kHz), piezoelectric ceramics could be utilized as sonic and ultrasonic transducers to generate high frequency sounds for different testing and measurement applications [17, 18].

Piezoactive stages with their ultra-fine resolution and fast frequency response are utilized in variety of micro and nanopositioning applications. Many emerging applications could be found for piezoactive stages in today's research and technology. Based on the Physik Instrumente (PI)® catalog [8], the following various categories for piezoelectric actuator applications could be listed; In *Life Science, Medicine* and *Biology* category they are utilized for scanning microscopy, patch clamping, gene manipulation, micromanipulation, cell penetration, and microdispersing. In *Semiconductors* and *Microelectronics* they are implemented for nanometrology, wafer and mask positioning and alignment, critical dimension measurement, microlithography and nanolithography, inspection systems, and vibration cancellation. In *Optics* and *Photonics* technologies they are used for fiber optic alignment and switching, image stabilization, adaptive optics, scanning microscopy, auto-focus systems, interferometry, laser tuning and mirror positioning. In *Precision Machines* and *Mechanical Engineering* they are employed for vibration cancellation, wear correction, needle-valve actuation, micropumps, knife edge control in extrusion tools, and micro-engraving systems.

1.1.6. Nonlinearities in Piezoelectric Materials

Piezoelectric materials suffer from material-level nonlinearities such as *hysteresis* and *creep* that drastically degrade their performance in precision positioning. Hysteresis is referred to a complex input/output multi-loop phenomenon with a memory-dominant nature [19-22]. That is, the future value of the output depends not only on the instantaneous value of the input but also on the history of its operation, especially the extremum values. Hysteresis nonlinearity originates from the material crystalline polarization and molecular effects. Figure 1.6 demonstrates a typical hysteresis response of a piezoactive stage to an alternating triangular input profile.

Creep is defined as unwanted changes, generally in logarithmic shape, in the displacement of piezoelectric actuator over time. This phenomenon is related to the effect of the applied voltage on the remanent polarization of the piezo ceramics. Generally, creep is the expression of the slow realignment of the crystal domains in a constant electric field over time [8]. Figure 1.7 demonstrates a creep response of a piezoelectric actuator to a step input.

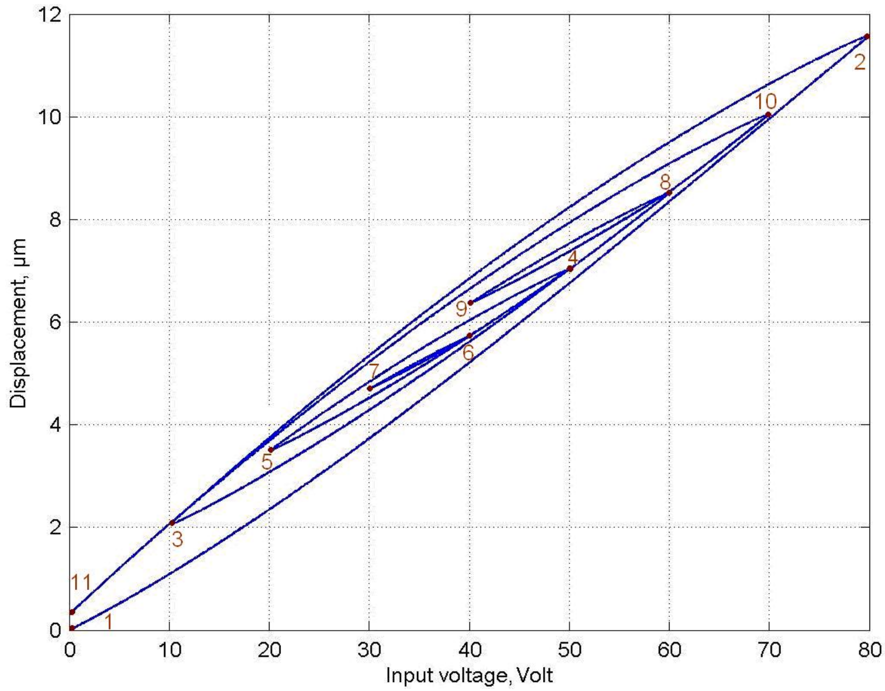

Figure 1.6. Hysteresis response of a piezoactive nanopositioning stage to an arbitrarily alternating input.

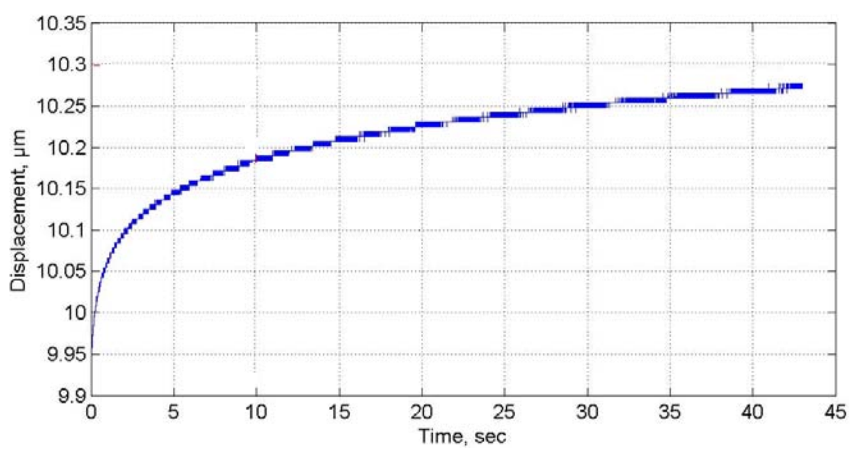

Figure 1.7. Creep response of a piezoactive nanopositioning stage to a step input.

1.1.7. Modeling and Control of Piezoactive Stages

Modeling of piezoactive systems can be divided into two parts (see Figure 1.8): (i) modeling of material-level nonlinearities which mainly include creep and hysteresis phenomena, and (ii) modeling the combined dynamics of piezoelectric element and the attached mechanical compartments (e.g. flexures). Over time, there has been a continuous interest on the modeling and compensation of hysteresis nonlinearity for various dynamic systems. This has led to invention of numerous methodologies ranging from classical phenomenological methods such as Preisach [23, 24] and Prandtl-Ishlinskii [25, 26] operators, to recently developed constitutive methods including the Lining method [27, 28] and the memory-based frameworks [20-22].

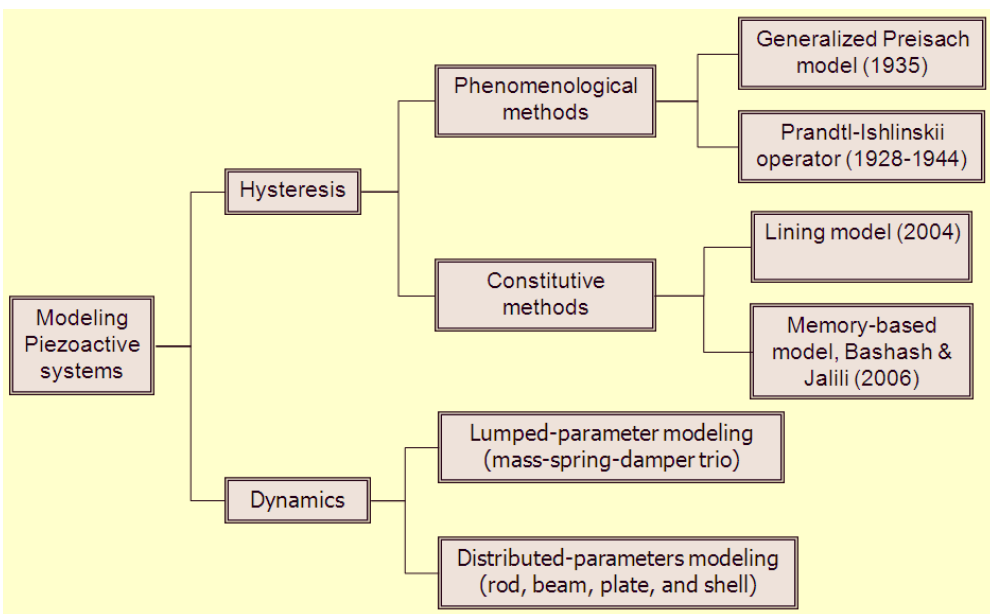

Figure 1.8. Modeling strategy for piezoactive systems.

Derivation of dynamic models for piezoactive systems depends on their structural and geometrical configurations. For example, piezostack actuators and flexures can be modeled by rod-type structures with appropriate boundary conditions. On the other hand, piezopatch actuators can be attached to flexible beams, plates, and shells whose structures determine the dynamics of system. In general, the dynamics of piezoactive systems can be well described by distributed-parameters representation expressed by partial differential equations. However, depending on the frequency of operation, system can be safely simplified to lumped-parameters representation. Although a few works have adopted distributed-parameters models for piezostack systems [29, 30], many others have considered lumped-parameters representation [31-33]. Their justification relies on the fact that piezostack systems usually have higher resonant frequencies than the operational frequency. Hence, the need for modeling of higher modes is eliminated when working below the first resonance. Conversely, piezopatch systems are generally attached to flexible structures whose resonant modes may fall within the operational frequencies. Thus, a well formulated distributed-parameters representation is required to account for the dynamics. Examples of piezopatch systems attached to different flexible structure are given in [34-36].

While piezopatch actuators are widely used for vibration control purposes, piezostack actuators are mostly used for precision positioning and trajectory tracking tasks. Tracking control of piezoelectric stack actuators have been extensively carried out in both feedforward and feedback control schemes. Most feedforward controllers cascade an inverse hysteresis model in series with plant to cancel out the effect of nonlinearity and achieve a relatively linear response [21, 24, 27]. There are a few references that have accounted for plant dynamics as well as hysteresis nonlinearity in feedforward control scheme [26]. However, for ultra-accurate positioning and tracking of high-frequency trajectories, the use of feedback controller is inevitable. Examples of such techniques could include time-optimal motion control [37], proportional-integral control with inverse model compensation [38], sliding mode [39, 40], adaptive [41], and neural network-based control [42].

Although extensive references are available on the modeling and control of piezoactive micro and nano systems, with the complexity in the dynamic behavior of such systems and the required level of precision and bandwidth, there is need for fundamental and innovative research in this area to enhance the present frameworks or generate new methodologies that meet the increasing demands of today's research and industry. The next subsection presents the driving motivations of this effort.

1.2. Research Motivation

With an ongoing growth of demand to piezoactive systems, accurate modeling and high-performance control methods play substantial roles on acquiring cutting-edge results in various technologies and applications. Along this line, we aim to address important issues on precision modeling and control of piezoactive systems. More specifically, the objectives of this research are:

- To compare various modeling and control schemes for specific configurations of piezoactive systems such as piezo-flexural nanopositioning stages and Active Probes.

- To improve accuracy and speed of control processes involving piezoactive systems.
- To develop novel modeling and control frameworks which not only benefit this specific area but also could be applied to a broad class of dynamic systems.

1.3. Contributions

The major contributions of this dissertation could be summarized as:

- Development of a new memory-based hysteresis modeling and control framework for piezoactive micro and nanopositioning systems
- Development of a Lyapunov-based robust adaptive control strategy for single and coupled parallel piezoactive nanopositioning stages
- Development of a switching controller for high performance tracking control of time-varying discontinuous trajectories with application to probe-based imaging and nanopositioning
- Development of a laser free Atomic Force Microscopy for high-speed imaging of micro and nano scale surface topographies
- Development of a distributed-parameters modeling and state-space control frameworks for rod-type solid state actuators

- Development of a modeling and vibration analysis framework for Euler-Bernoulli beams with cross-sectional discontinuities with application to piezoactive NMC Probes
- Modeling and experimental vibration analysis of NMC Active Probes with application to ultrasmall mass detection

1.4. Dissertation Overview

The rest of the dissertation is organized as follows:

In Chapter two, modeling and control of hysteresis nonlinearity in piezoactive nanopositioning systems is discussed. A modification is proposed for the widely-used Prandtl-Ishlinskii hysteresis operator for the enhancement of its accuracy in the prediction of nonsymmetrical hysteresis loops. A novel memory-based hysteresis modeling framework is then presented for more accurate and computationally efficient implementation. Experimental verifications for both frameworks are presented.

In Chapter three, addition of a lumped-parameters dynamic model to the hysteresis nonlinearity is introduced to achieve high-bandwidth feedforward and feedback tracking control of piezoactive nanopositioning systems. A model-based feedforward and a Lyapunov-based robust adaptive feedback control strategies are presented and implemented in the piezoactive nanopositioning systems. Results indicate that hysteresis modeling is an essential part of a feedforward control process. However, it has a minor impact in the feedback control scheme, where a robust adaptive controller developed based on the system real-time feedback enables achieving a good level of performance in the absence of hysteresis model and despite the parametric uncertainties. The application of the proposed framework on a non-laser Atomic Force Microscopy (AFM) system is presented for low-cost and high-speed imaging of surface topographies with micro and nano scale variations. It is shown that the bulky expensive laser utilized in typical AFMs can be effectively replaced by piezoresistive-based microcantilevers.

Chapter four focuses on a special case of interest where tracking control of time-varying trajectories are desired while frequent stepped discontinuities appear in the desired trajectory. It has been shown that when the feedback controller gains are tuned for high-performance tracking of continuous trajectories, the presence of the steps could generate substantial oscillations in the response. Vice versa, when controller gains are tuned for step tracking, the overall performance is decreased in tracking of continuous trajectories. Hence, a switching controller is proposed to control the continuous and stepped trajectories with separately tuned controllers. Switching conditions and continuity laws of control input are presented and discussed.

Chapter five presents a distributed-parameters modeling and a state-space control framework for rod-type solid-state actuators such as piezoelectric, magnetostrictive and electrostrictive actuators. Fundamental vibration analysis methods have been utilized to derive the distributed-parameters state-space representation of such actuators. A new state-space control law is then developed for asymptotic and robust output tracking control of actuator under uncertainties and unknown disturbances. Integration of the optimal observer is discussed for practical implementation of this framework. It is shown that for ultrahigh bandwidth tracking control of rod-type actuators including piezoactive nanopositioning stages, utilization of a distributed-parameters controller is inevitable.

Finally, Chapter 6 presents modeling and experimental vibration analysis of Active Probes with application to ultrasmall mass detection. Using the piezoelectric constitutive relations and a new modeling framework proposed for stepped beams, the state-space formulation of the present configuration of Active Probes is derived. The proposed model is validated on a real probe indicating the strength and accuracy of the proposed discontinuous beam modeling framework. Using the Focused Ion Beam (FIB) technique, a narrow thin layer is then deposited on the cantilever tip. The developed model along with a system identification technique are utilized to estimate to amount of the added mass based on the shifts observed in the resonant frequencies of the probe. A mass of in the order of a few hundred pico-grams was detected for the deposited layer, as a result.

CHAPTER TWO

HYSTERESIS MODELING AND COMPENSATION IN PIEZOACTIVE MICRO- AND NANO-POSITIONING SYSTEMS

2.1. Introduction

Piezoactive micro and nanopositioning systems suffer from hysteresis nonlinearity when utilized for ultra-high precision positioning, imaging, and manufacturing applications. Although numerous research works have been conducted during the past couple of decades on the nonlinear modeling, identification and compensation of hysteresis, thus far there are no universally accepted rules to describe this phenomenon. Hysteresis is a complex input/output multi-loop phenomenon affected by the existence of non-local memories [19-22]. That is, the future value of the output depends not only on the instantaneous value of the input but also on the history of its operation, especially the extremum values.

Hysteresis models are classified into two conceptually different types. One class consists of the constitutive approaches that are inspired from the underlying physics of the phenomenon and are derived based on the empirical observations. The second type includes phenomenological approaches, which essentially employ mathematical structures to describe the phenomenon without considering its underlying physics.

Extensive research work has been carried out to develop effective hysteresis models using constitutive approaches. For instance, Adriaens *et al.* [29] used an electromechanical model combined with nonlinear first order differential equations to describe both hysteresis and the systems dynamics. A generalized Maxwell resistive capacitor model was utilized as a lumped-parameters casual representation of hysteresis by Goldfarb *et al.* [43]. However, the constitutive approaches have limited performance characteristics as the underlying physics of the hysteresis phenomenon has not been completely understood.

Phenomenological approaches for hysteresis modeling have also been extensively developed. The most well-known phenomenological approach, known as Preisach model [23, 24], has found widespread acceptance in modeling of hysteresis in piezoactive materials. Although Preisach model provides a purely mathematical tool for modeling complex hysteresis loops, it does not provide a physical insight into the phenomenon. Furthermore, the numerical implementation of Preisach and other phenomenological models requires considerable numerical efforts.

Among the phenomenological method the Prandtl-Ishlinskii (PI) hysteresis operator has recently attracted significant attention due to its straightforward and effective implementation [25, 26]. PI is a discretized sub-class of Preisach operator which nearly presents the same level of accuracy in practice. The structure of PI operator is in such a way that a set of weighted backlash operators with different threshold values is superposed to predict the multiple-loop hysteresis response. However, similar to other phenomenological models, the conventional PI operator lacks accuracy due to its rigid structure. Consequently, several modifications have been proposed to improve this methodology [26, 44]. Yet, further improvements are needed for effective implementation of the PI operator.

In this chapter, both phenomenological and constitutive methodologies are investigated for possible improvements in the accuracy and the computational efficiency of hysteresis phenomenon. First, a new modification is proposed for the conventional PI operator to improve its accuracy. It is demonstrated that by interleaving a new parameter in the primary backlash operators, the shape of ascending and descending curves can be independently tuned leading to improved response. The proposed modification has been experimentally validated on a piezoactive nanopositioning stage with hysteretic behavior.

A new constitutive modeling and feedforward control framework is then presented for hysteresis compensation in piezoactive actuators. A set of memory-based hysteresis properties are observed using a set of experimental runs. These properties, namely, targeting turning points, curve alignment and wiping-out effect, are then applied in an exponential and a linear mapping strategy to develop two mathematical frameworks for modeling of hysteresis phenomenon. More specifically, the locations of turning points are detected and recorded for the prediction of future hysteresis trajectory. An internal trajectory is assumed to follow a multiple-segment path via a continuous connection of several curves passing through every two consequent turning points. These curves adopt their shapes from the reference hysteresis curves with exponential and polynomial configurations. Experimental implementation of the proposed method demonstrates significant improvement compared to the PI hysteresis operator. However to maintain the level of precision during the operation, a sufficient number of memory units must be included to record the turning points. The proposed modeling framework is adopted in an inverse model-based control scheme for feedforward compensation of hysteresis nonlinearity in piezoactive nanopositioning systems.

2.2. PI Hysteresis Operator

PI hysteresis operator is a phenomenological method for describing Input/Output (I/O) static hysteresis with the effect of memory. This method employs a combination of several rate-independent backlash or linear-play operators as shown in Figure 2.1, with the mathematical representation given by:

$$\begin{gathered} y(t) = H_{r,w_h}[x, y_0](t) = w_h \max\{x(t) - r, \min\{x(t) + r, y(t-T)\}\} \\ y(0) = w_h \max\{x(0) - r, \min\{x(0) + r, y(0)\}\} \end{gathered} \tag{2.1}$$

where $x(t)$ denotes the backlash input, $y(t)$ is the output of the operator, r is the input threshold value or the magnitude of the backlash, w_h is the weighting value and T is the sampling period. A PI hysteresis operator is then modeled by a linearly weighted superposition of several backlash operators with different threshold and weighting values as follows:

$$y(t) = \sum_{i=0}^{n} H^{i}_{r,w_h}[x, y_0](t) = \sum_{i=0}^{n} w_h^i \max\{x(t) - r^i, \min\{x(t) + r^i, y(t-T)\}\} \tag{2.2}$$

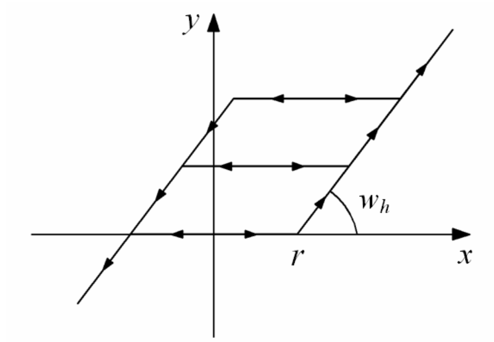

Figure 2.1. Primary backlash operator utilized in the PI hysteresis model.

Figure 2.2 depicts a typical hysteresis response obtained from the superposition of four backlash operators with different threshold and weighting values.

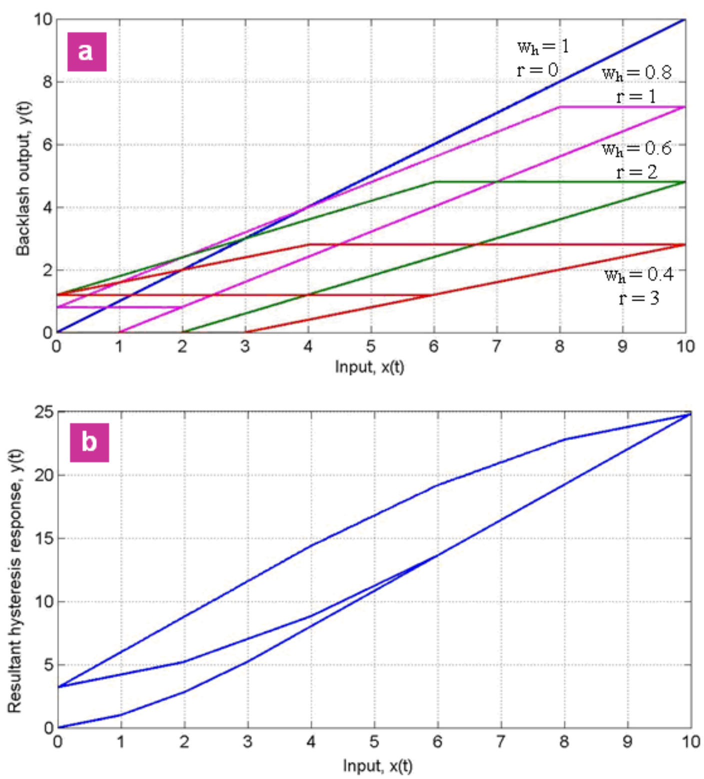

Figure 2.2. A sample hysteresis obtained by superposition of four backlash operators with different threshold values and weighting values.

2.2.1. Modified PI Hysteresis Operator [26]

Modeling of system using the conventional PI hysteresis operator lacks accuracy due to the rigid structure of the primary backlash operator. For example, PI hysteresis operator has the property of symmetry around the center of the loop, while hysteresis response of an actual piezoactive system is not symmetric. The other shortfall of this operator is its lack of accuracy in adjusting the residual displacement around the origin. One solution is to design and integrate new operators with the PI operator in order to compensate for the described deficiencies. However, this would increase the model complexity, and limit its practical implementation [25].

A modification is proposed in this section to simultaneously compensate the symmetry and the residual displacement problems associated with the primary PI operator [26]. For this, a new parameter $\eta > 0$ is proposed to be interleaved in the primary backlash operators of the PI hysteresis model resulting in the following equation:

$$\begin{aligned} y(t) = H_{r,\eta,w_h}[x, y_0](t) = w_h \max\{x(t)-r, \min\{x(t)+\eta r, y(t-T)\}\} \\ y(0) = w_h \max\{x(0)-r, \min\{x(0)+\eta r, y(0)\}\} \end{aligned} \tag{2.3}$$

Parameter η alters the threshold of the backlash in the descending state. That is, the larger η is chosen, the more delay appears in the descending state. With proper selection of η for every individual backlash operator, the flexibility and accuracy of the model can be significantly enhanced. Figure 2.3 demonstrates the response of the modified backlash operator with different values of η. The modified PI hysteresis operator can then be written as:

$$y(t) = \sum_{i=0}^{n} w_h^i \max\{x(t) - r^i, \min\{x(t) + \eta^i r^i, y(t-T)\}\} \tag{2.4}$$

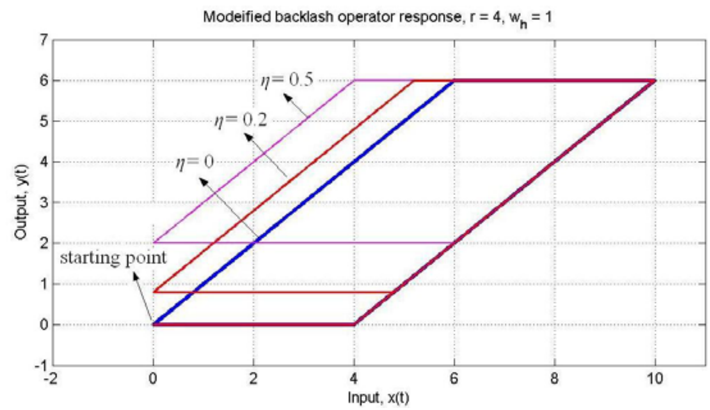

Figure 2.3. Modified backlash with different delay values in the descending state.

2.2.2. Inverse PI Hysteresis Operator

One of the advantages of the PI hysteresis model is that its inverse is also of PI type, however, with different threshold and weighting values. The inverse PI operator could be analytically obtained from [25]:

$$z(t) = \sum_{i=0}^{n} H_i^{-1}[y, z_0](t) = \sum_{i=0}^{n} w_h^{'i} \max\{y(t) - r^{'i}, \min\{y(t) + \eta^i r^{'i}, z(t-T)\}\}$$

$$w_h^{'0} = \frac{1}{w_h^0}; \; w_h^{'i} = \frac{-w_h^i}{(\sum_{j=0}^{i} w_h^j)(\sum_{j=0}^{i-1} w_h^j)}, \; i = 1 \ldots n \tag{2.5}$$

$$r^{'i} = \sum_{j=0}^{i} w_h^j (r^i - r^j), \; z_0^i = \sum_{j=0}^{i} w_h^j y_0^i + \sum_{j=i+1}^{n} w_h^j y_0^j, \; i = 1 \ldots n$$

Graphically, the inverse model is the reflection of the resultant hysteresis curves about the 45° line.

2.2.3. Experimental Setup

The validation of the proposed hysteresis model is investigated by a set of experimental tests on a Physik Instrumente P-753.11c PZT-driven nanopositioning stage with high resolution capacitive position sensor (see Figure 2.4). Experimental data interfacing is carried out through a Physik Instrumente E-500 chassis for actuator amplifier and position servo-controller along with dSPACE® DS1104 data acquisition controller board. The position of the nanopositioning stage is reflected by a sub-nanometer resolution built-in capacitive sensor.

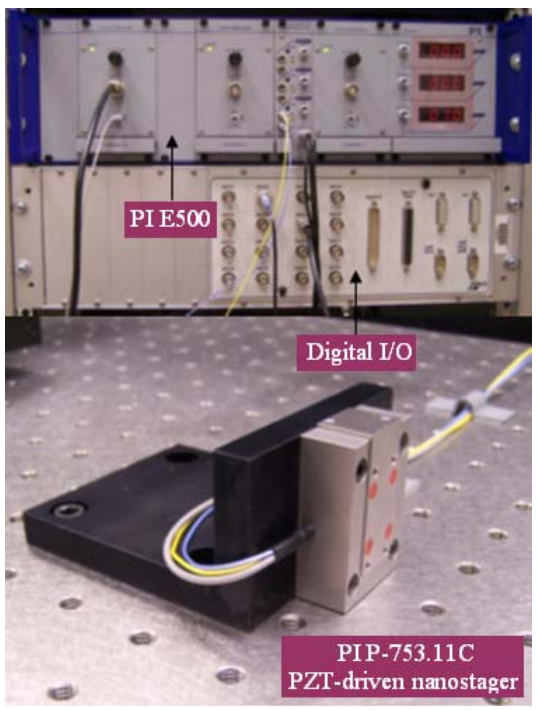

Figure 2.4. Experimental setup: the Physik Instrumente P-753.11C nanopositioning stage with built-in capacitive position sensor connected to the DS1104 controller board through a Physik Instrumente E-500 amplification and acquisition system.

2.2.4. Identification of the Hysteresis Model

The accurate identification of the hysteresis operator between the input voltage and the stage displacement is a crucial step in achieving effective control. The objective here is to identify the weighting parameters and η values, for a set of backlash operators with predefined thresholds, in order to obtain a minimal error between the experimental data and the model responses. 26 backlash operators are exploited here to cover the input range of 0 to 60 Volts. Threshold values are chosen in an orderly increasing sequence, with fine intervals for the initial and course intervals for the large input values to maintain a fair balance between the model accuracy and computational efficiency.

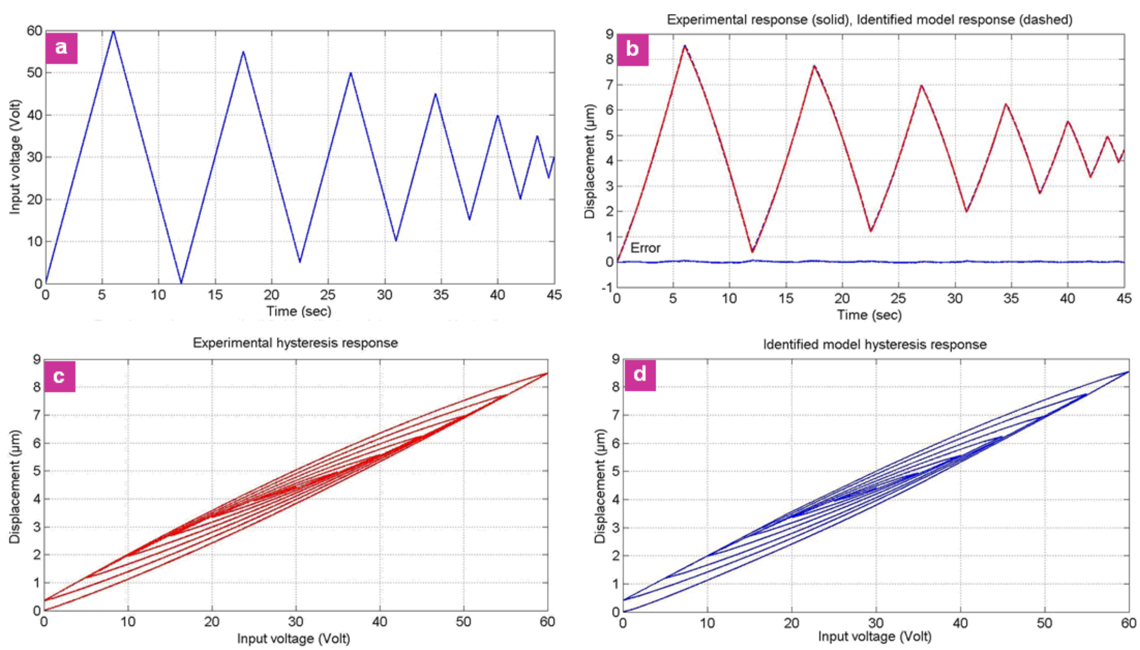

Figure 2.5. Hysteresis model identification; (a) input signal, (b) experiment and identified model responses; hysteresis response of (c) experiment and (d) identified model.

A least-square optimization technique is utilized here for the error minimization. The identification input is designed in such a way that it covers the entire span of the actuator input. Figure 2.5 and Table 2.1 demonstrate the identification results and estimated parameter values. For the given input, the maximum and mean-square identification error values are obtained as $e_{\max} / x_{\max} = 0.82\%$ and $\frac{1}{T}\int_0^T |e(t)|\,dt = 0.015\mu m$, respectively.

Table 2.1. Parameter values of the identified hysteresis model.

i	w_h^i	r^i	η^i	i	w_h^i	r^i	η^i
0	0.0824	0	0.35	13	0.0018	16	0.26
1	0.0178	1	1.04	14	0.0011	18	0.18
2	0.0071	2	1.74	15	0.0009	20	0.19
3	0.0048	3	1.87	16	0.0031	22	0.17
4	0.0041	4	3.13	17	0.0023	24	0.15
5	0.0025	5	0.97	18	0.0038	26	0.15
6	0.0012	6	2.27	19	0.0012	28	0.07
7	0.0022	7	0.69	20	0.0043	30	0.29
8	0.0010	8	0.75	21	0.0101	35	0.16
9	0.0007	9	0.51	22	0.0009	40	0.35
10	0.0011	10	0.54	23	0.0006	45	0.35
11	0.0003	12	0.31	24	0.0004	50	0.35
12	0.0033	14	0.49	25	0.0079	55	0.35

To demonstrate the effectiveness of the modified PI model over the conventional approach, a representative model for the conventional approach is developed by setting η^i to zero in Eq. (2.4) and identifying the weighing parameters for the same experiment described above. The same number of backlash elements with the same threshold values is utilized. For the sake of accuracy, an adjustable offset is added to the operator to locate the hysteresis loops as close as possible to the experimental response. Figure 2.6(a) depicts the hysteresis response of the conventional PI model to the same input shown in Figure 2.5(a). Comparisons of the modeling errors between conventional and modified approaches are depicted in Figure 2.6(b). It is clearly observed that the modified PI model demonstrates improved response over the conventional approach. The maximum and mean-square error values for the conventional model are obtained as 4.1% and 0.04 μm, respectively.

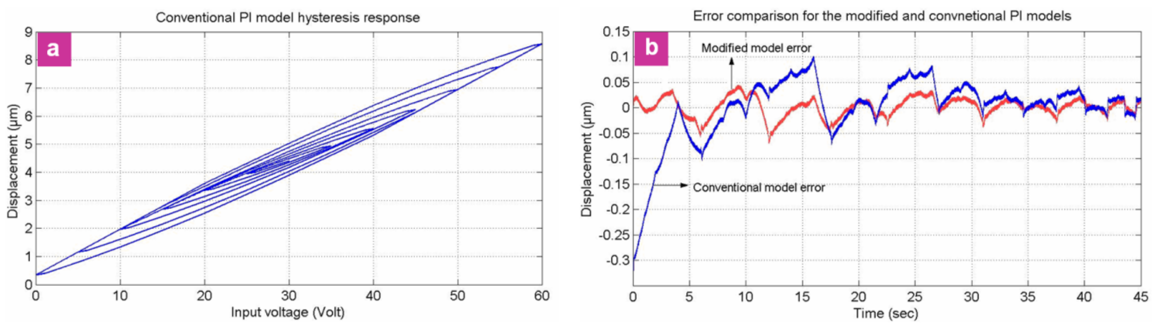

Figure 2.6. (a) Hysteresis response of the conventional PI model, and (b) modeling error comparisons for the conventional and modified PI models.

The threshold and weighting values of the inverse hysteresis model are identified using Eq. (2.5). We remark here that parameter η is the coefficient of the backlash threshold in the descending state, and is identical in both direct and inverse models. The parameters of the inverse hysteresis model are listed in Table 2.2.

Table 2.2. Identified inverse hysteresis model parameters.

i	w_h^i	r^i	i	w_h^i	r^i
0	12.13	0	13	-0.11	1.887
1	-2.16	0.082	14	-0.06	2.148
2	-0.66	0.183	15	-0.05	2.412
3	-0.39	0.290	16	-0.17	2.678
4	-0.31	0.402	17	-0.12	2.950
5	-0.18	0.518	18	-0.19	3.226
6	-0.09	0.637	19	-0.06	3.510
7	-0.15	0.757	20	-0.20	3.796
8	-0.07	0.880	21	-0.43	4.534
9	-0.05	1.003	22	-0.04	5.322
10	-0.07	1.127	23	-0.02	6.114
11	-0.02	1.378	24	-0.02	6.909
12	-0.21	1.629	25	-0.29	7.706

2.3. Memory-based Hysteresis Modeling [20-22]

In this subsection, a novel constitutive modeling framework is presented for precise compensation of hysteresis in piezoactive systems. The underlying memory-dominant properties of hysteresis are identified through several experimental observations. Then, two mathematical frameworks are developed and presented to adopt these properties and produce systematic models that could be utilized for precision control of piezoactive nanopositioning systems.

2.3.1. Memory-based Hysteresis Properties

The memory-based properties of hysteresis are investigated here by a set of experimental tests on the PZT-driven nanopositioning stage depicted in Figure 2.4. In order to study the pure hysteresis response and avoid the effects of mechanical compartments such as material damping and inertia, the input is designed and implemented at a constant rate.

Figure 2.7 depicts the hysteresis response of the actuator for a set of triangular input signals. Hysteresis curves are encompassed by two so-called “major” or “reference” curves. These curves are obtained by raising the input signal from zero to its maximum permitted value and then decreasing it to its minimum extreme. As seen from the figure, all ascending curves starting from zero follow an identical path on the ascending reference curve, and all the descending curves branching from different locations are similar in shape and approach a particular point. Therefore, the behavior of hysteresis for the first ascending and the first descending input signals can be characterized by identifying the configuration of reference curves and the lower converging point.

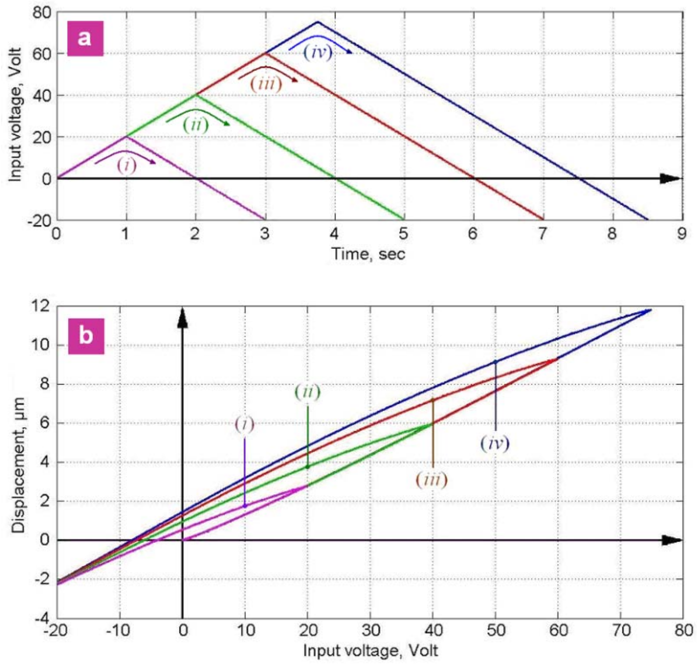

Figure 2.7. Hysteresis response of the Physik Instrumente P-753.11C nanopositioning stage to triangular input signals; (a) input profiles and (b) stage response.

The behavior of hysteresis for the rest of input alternations (other than first two alternations) is, however, quite complicated. The clues for prediction of the hysteresis path for multiple internal loops can be found by realizing the behavior of the response around turning points at which the direction of input changes. Figure 2.8 demonstrates the hysteretic response of the PZT-driven actuator to a set of four alternating continuous input profiles. Inputs are designed in such a way that the effects of turning points in the hysteresis trajectory become visual. To make the graphs and the hysteresis paths more comprehensible, the initial, internal turning, and the end points are spotted and marked by numbers. Three out of four input signals have four segments: After moving up to Point #2 the direction of the input changes, where the upper turning point is recorded. Then, the input signal descends to Point #3 where the lower turning point is recorded. The input goes up one more time to Point #4, and finally descends to its zero ending point (Point #5). Three different locations are considered as Point #4 for the generalization of observations around the turning Point #3. A closer look at Figure 2.8(b) clearly demonstrates that the hysteresis track, branching from a turning point, approaches the previous turning point, in a manner that the configuration of the curve remains similar to the related reference curve. For example, tracks that are originated from Points #3 and #4 in Figure 2.8(b) approach Points #2 and #3, respectively, maintaining their shape similar to the ascending and descending reference curves, correspondingly.

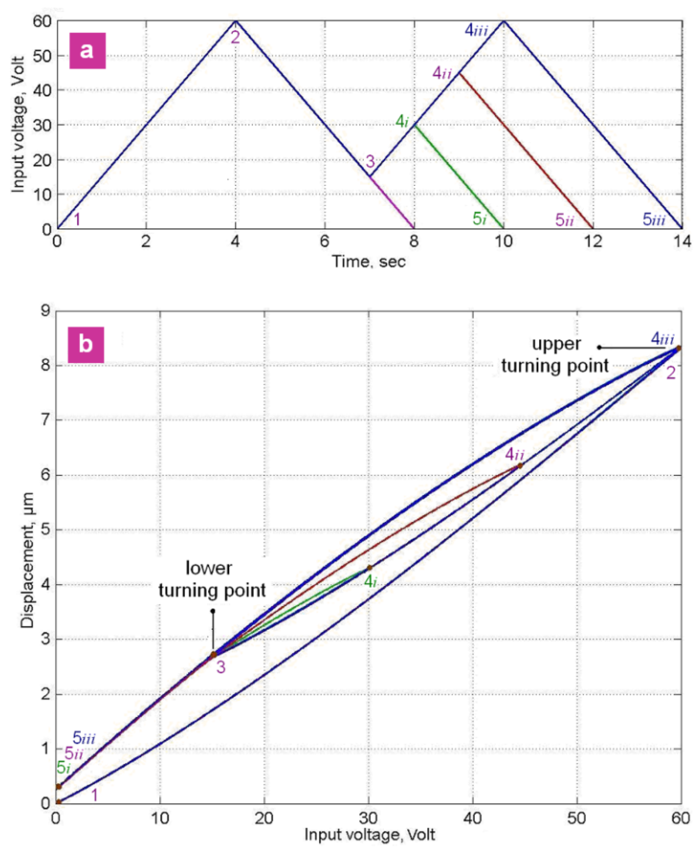

Figure 2.8. Hysteresis response to a set of four alternating continuous input profiles; (a) input signals and (b) stage response.

The direction of hysteresis path slightly changes after intersecting a turning point. Hence, the effect of “curve alignment” property is seen from Figure 2.8b, where curves approaching Point #3 from three different points marked as #4 merge together after passing the turning point, and continue on an identical path. The physical interpretation of this hysteresis property is interesting; *there is no way for an internal path to break the hysteresis bounds and escape from the borders sketched by other hysteresis trails; all hysteresis tracks arriving to a turning point unite together and align themselves to the previously broken curve associated with that turning point*.

An internal turning point is created when the path of a hysteresis track is broken from approaching a target point. Consequently, after curve alignment in a crossed turning point, the new trajectory continues the path of previously broken track toward the intact target point. The label of “smart” for the piezoelectric materials is better realized when it is observed that for any number of untouched internal loops, the location of turning points and the path of hysteresis trajectory are recorded in the material memory.

One of the important properties of hysteresis is the wiping-out effect. Based on this property, only the alternating series of dominant internal loops, which are not crossed by other hysteresis tracks, are stored in the memory and all other loops are wiped out. Figure 2.9 demonstrates the wiping-out property when the input signal surpasses a dominant extremum. Dominant extrema are the maximum or minimum points that have respectively greater or less values than the subsequent values of input signal. It is evident that the dominancy property of an extremum is eliminated when it is passed by the subsequent signal.

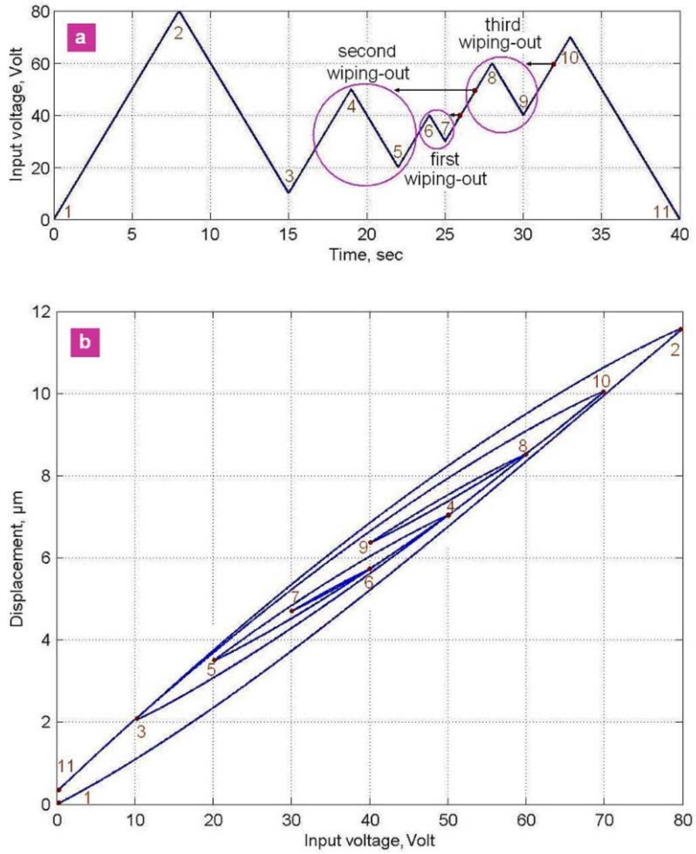

Figure 2.9. Wiping-out and curve alignment properties of hysteresis; (a) arbitrarily alternating input profile, and (b) the resultant hysteresis response.

As the input signal alternates up and down to reach Point #7 in Figure 2.9(a), one surrounding and two minor loops are generated in the input/output (I/O) hysteretic domain as the result of these alternations (see Figure 2.9(b) for the I/O domain). Starting from Point #7, the input signal is increased to a point with the same magnitude as the extremum #6. At this point, which is marked by a spot in the input domain (Figure 2.9(a)), the effect of turning Points #6 and #7 and the properties of the crossed minor loop are no longer useful for the remaining hysteresis track, and hence, are wiped out. In the

I/O domain, hysteresis trajectory aligns and continues the path of previously broken rising curve associated with Points #5 and #6 (curve 5-6) towards the target Point #4.

The second internal loop associated with Points #4 and #5 is wiped out when the input value exceeds the extremum #4. Similarly, the trajectory aligns and continues the path of the broken curve 3-4. The direction of input changes at Point #8 and trajectory targets down toward turning Point #3, since turning Points #5 and #7 have been wiped out. Descending input is stopped in the midway at Point #9 and increased to a value equal to that of extremum #8. At this point, the third wiping-out effect occurs with the trajectory aligning and continuing the path of curve 3-8 up to Point #10, where the direction of input changes one more time. The trajectory initiating from turning Point #10 approaches and hits Point #3 and continues the path of curve 2-3 until the input reaches its zero ending value at Point #11. Although the hysteresis path from Point #3 to Point #10 (3-4-5-6-7-6-4-8-9-8-10) is an alternating multi-loop trajectory, the hysteresis track follows path 3-4-8-10 and stands at the same terminating point, even if the input directly increase from Point #3 to Point #10.

In conclusion, although hysteresis seems to be an unpredictable and chaotic phenomenon in piezoelectric materials, by realizing the underlying physics of its intrinsic behavior, an intellectual harmony can be observed in the manner this phenomenon performs. In the following subsection, an exponential mapping strategy is proposed for development of a mathematical modeling framework for this phenomenon.

2.3.2. Memory-based Hysteresis Model with Exponential Mapping

As discussed earlier, hysteresis curves belonging to the same class of ascending or descending states are similar in shape with difference being in their slope of convergence. An exponential expression is proposed here for fitting a uniform hysteresis curve between two arbitrary points (v_1, x_1) and (v_2, x_2) in voltage-displacement plane as follows:

$$x(v) = F(v, v_1, x_1, v_2, x_2) = k(1 + ae^{-\tau(v-v_1)})(v - v_1) + x_1 \qquad (2.6)$$

a and τ are constant parameters that shape the hysteresis curves, and *k* represents the slope of exponential hysteresis mapping between two initial and ultimate points given by:

$$k = \frac{x_2 - x_1}{v_2 - v_1}(1 + ae^{-\tau(v_2 - v_1)})^{-1} \qquad (2.7)$$

Parameters a and τ are identified for the ascending and the descending reference curves and kept unchanged for any other internal curves, while parameter *k* is calculated for every individual curve between two initial and ultimate points. Based on this mapping technique, the hysteresis path becomes predictable for any trajectory between known initial and target turning points.

Figure 2.10 demonstrates a typical hysteretic response consisting of *n* internal loops. Lower and upper turning points are labeled by *L* and *U* subscripts, while the ascending and descending curves are labeled with *A* and *D* subscripts, respectively. The numbering sequence starts from the smallest internal loop to the largest surrounding loop. Regarding the curve alignment in the turning points, for the ascending curve starting from point (v_{L1}, x_{L1}) and shown with a dashed configuration and labeled by F_{A0} in Figure 2.10, the prediction of hysteresis path is expanded to:

$$x_A(v) = F_{A0}(v) = F(v, v_{L1}, x_{L1}, v_{U1}, x_{U1}) H(v, v_{L1}, v_{U1}) + \sum_{i=1}^{n} F_{Ai}(v) H(v, v_{Ui}, v_{U(i+1)}) \qquad (2.8)$$

where n is the number of intact internal loops recorded by hysteresis trajectory, and H represents the bilateral unit heaviside function expressed as:

$$H(x,a,b) = \begin{cases} 1 & a \le x \le b \\ 0 & x > b \ or \ x < a \end{cases} \qquad (2.9)$$

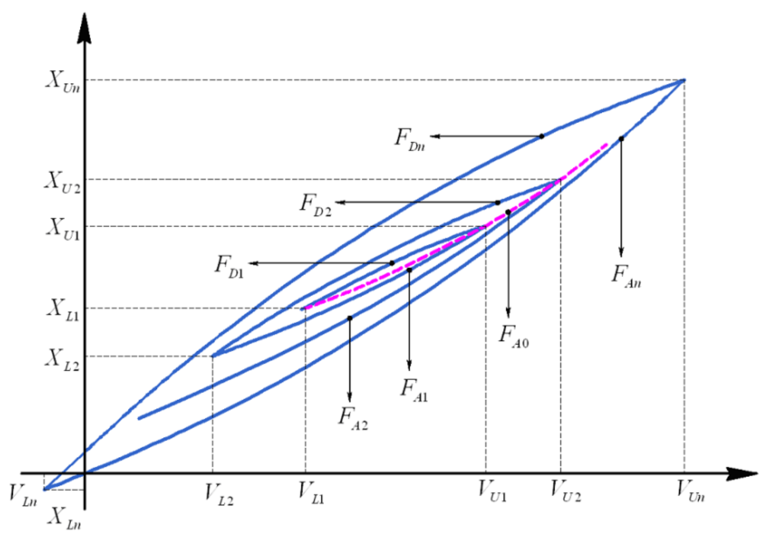

Figure 2.10. Typical input/output (V/X) hysteresis response with n internal loops.

Equation (2.8) states that hysteresis path is composed of a sequential set of different hysteretic curves that are separated by intervals and distinguished by turning points. Except for the first segment of the path, the other segments are the continuation of the previously broken hysteresis curves. Therefore, the proposed formulation satisfies curve alignment property in turning points. Similarly, for a descending curve starting from point (v_{U1}, x_{U1}), the hysteresis path is expressed as:

$$x_D(v) = F(v, v_{U1}, x_{U1}, v_{L1}, x_{L1}) H(v, v_{L1}, v_{U1}) + \sum_{i=1}^{n} F_{Di}(v) H(v, v_{L(i+1)}, v_{Li}) \tag{2.10}$$

Note that $(v_{U(n+1)}, x_{U(n+1)})$ and $(v_{L(n+1)}, x_{L(n+1)})$ are the locations of the upper and lower hysteresis extreme points on the reference curves, respectively.

The implementation of the described formulation requires a number of memory units to store the intact turning points. As an advantageous property, the wiping-out effect enables the prediction of the hysteresis path with a finite number of memory units even for infinite number of input fluctuations. Once the trajectory intersects with a turning point, that point is eliminated from the memory. Contrarily, if the trajectory changes its direction, the new turning point is recorded in the memory. It is obvious that for an input with a known profile, the minimum number of required memory units is identified by counting the maximum number of dominant extrema before the wiping-out effect occurs. However, for an unknown input profile, a reasonable number of memory units must be allocated so that the trajectory of hysteresis could be accurately predicted. If the memory capacity is not sufficiently assigned, the trajectory diverges from the actual hysteresis response when it surpasses the last stored turning point. Although by increasing the capacity of the memory the reliability of the prediction may increase, the computational efficiency is degraded. Depending on the application, a reasonable number of memories should be assigned so that a reliable and efficient prediction is achieved.

To demonstrate the model performance and study the memory-dominant behavior of hysteresis, a ± 10 Volt/sec input profile is designed such that the model requires at least three memory units for accurate prediction of hysteresis trajectory. The developed model is simulated with one, two and three memory unites separately. Parameters a and τ are identified as 0.37 and -0.019 for the ascending and 0.58 and 0.0074 for the descending reference curves, respectively.

Simulation and experimental results are depicted in Figure 2.11. Model responses with one, two and three memory units along with the actual actuator response to the input profile shown in Figure 2.11(a) are depicted in Figures 2.11(d), 2.11(c) and 2.11(d), respectively. As predicted before, model response with one memory unit diverges from the actual hysteresis response after input passes the first dominant extremum, in the same manner that the model response with two memory units diverges as the input overtakes the second dominant extremum. Model with three or more memory units demonstrates perfect performance with the modeling error sliding slightly up and down around the zero line.

Figures 2.11(f) to 2.11(h) demonstrate that model hysteresis response gets closer to the actual hysteresis response shown in Figure 2.11(e) as the number of memory units increase from one in Figure 2.11(f) to three in Figure 2.11(h), which is the minimum required number for the given trajectory here.

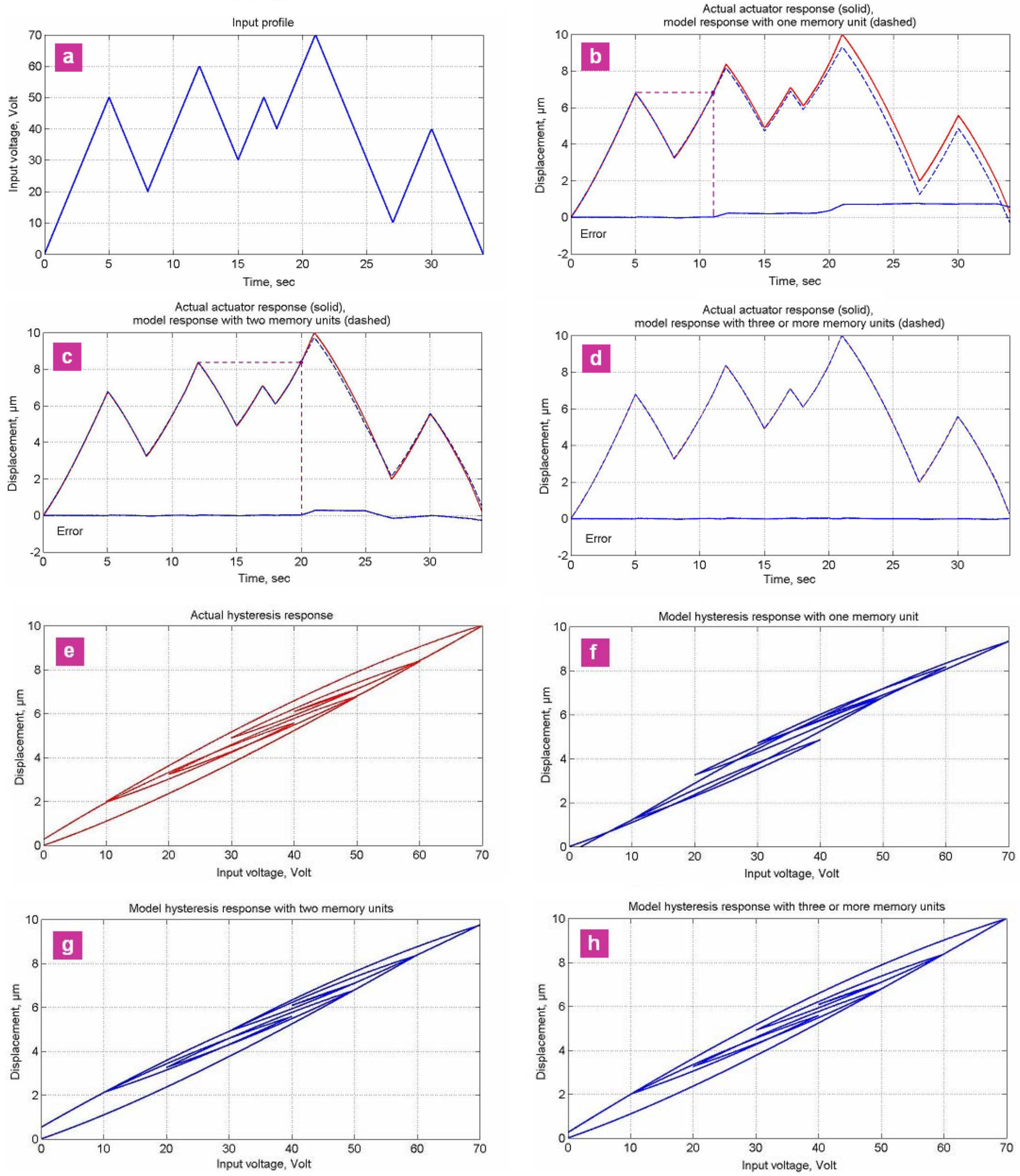

Figure 2.11. Experimental verification of the memory-based hysteresis model with exponential mapping strategy; (a) input signal, experimental and model responses with (b) one memory unit, (c) two memory units, and (d) three memory units, (e) actual hysteresis response, hysteresis response of the model with (f) one memory unit, (g) two memory units, and (h) three memory units.

2.3.3. Memory-based Hysteresis Model with Linear Mapping

In another mathematical representation of the memory-based hysteresis modeling, a polynomial-based linear mapping technique can be considered here. For this, the approximate functions for the ascending and descending loading curves are identified first, and then mapped between the two consequent points such that targeting turning points and curve alignment properties are fulfilled.

Assume that the ascending and the descending loading curves are identified by two piecewise continuously differentiable, monotonically increasing functions, $f_a(v)$ and $f_d(v)$, respectively. The rest of internal hysteresis curves adopt their shape from these reference curves. Here, as shown in Figure 2.12, a linear mapping strategy relates the displacement x to the corresponding ascending or descending reference function $f_r(v)$, where index r stands for a, for the ascending and d, for the descending reference curves defined above. Consequently, for any trajectory starting from point (v_1, x_1) and approaching point (v_2, x_2), the following linear mapping formulation is obtained:

$$x_{12}(v) = x(v, v_1, x_1, v_2, x_2) = af_r(v) + b \tag{2.11}$$

where $x_{12}(v)$ represents the hysteresis trajectory between points (v_1, x_1) and (v_2, x_2) when input voltage v is varied between v_1 to v_2; a and b are the parameters calculated by substituting points (v_1, x_1) and (v_2, x_2) into (2.11) (e.g. $x_1 = af_r(v_1) + b$), and are given by:

$$a = \frac{x_2 - x_1}{f_r(v_2) - f_r(v_1)}, \ b = \frac{x_1 f_r(v_2) - x_2 f_r(v_1)}{f_r(v_2) - f_r(v_1)} \tag{2.12}$$

Substituting a and b from Eq. (2.12) into Eq. (2.11) yields:

$$x_{12}(v) = x_1 + \frac{x_2 - x_1}{f_r(v_2) - f_r(v_1)}\left(f_r(v) - f_r(v_1)\right) \quad (2.13)$$

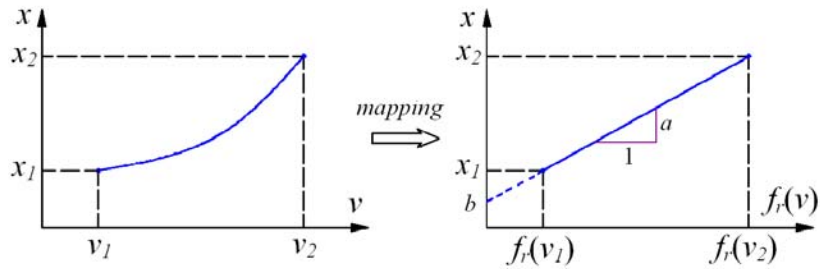

Figure 2.12. Linear mapping of a hysteresis curve between two initial and target points.

The fact that the hysteresis trajectory starting from a turning point targets all the previously recorded internal turning points enables the prediction of the response utilizing the proposed mapping strategy. Figure 2.13 depicts the hysteresis path originating from point (v_0, x_0). If the input keeps moving up to the maximum threshold point, the trajectory passes through all the internal target points (v_1, x_1), (v_2, x_2), … , (v_{n-1}, x_{n-1}), and approaches the upper threshold point (v_n, x_n). The describing equation for this path is given by:

$$x_{0n}(v) = \sum_{i=0}^{n-1} x_{i(i+1)} H(v, v_i, v_{i+1}) = \sum_{i=0}^{n-1} x_i + \frac{x_{i+1} - x_i}{f_r(v_{i+1}) - f_r(v_i)}\left(f_r(v) - f_r(v_i)\right) H(v, v_i, v_{i+1}) \quad (2.14)$$

where $x_{0n}(v)$ denotes the predicted multiple-segment hysteresis path, and H represents the bilateral unit Heaviside function given in Eq. (2.9).

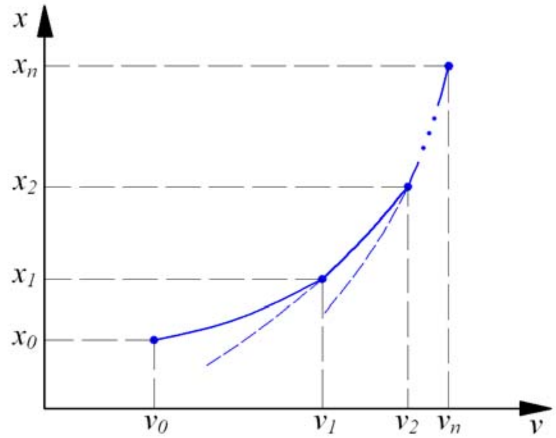

Figure 2.13. A typical multi-segment hysteresis path.

Equation (2.14) states that hysteresis path is composed of a sequential set of different curves that are separated by intervals distinguished by turning points. Except for the first segment of the path, the other segments are the continuation of the previously broken hysteresis curves. Yet, it is necessary to make certain that the proposed method satisfies the curve alignment property. To study this property, a theorem is presented and utilized to prove the satisfaction of curve alignment property by the proposed model.

Consider points (v_1, x_1), (v_0, x_0), and (v_2, x_2), as shown in Figure 2.14, on the hysteresis plane that satisfy:

$$v_1 < v_0 < v_2 \text{ and } x_0 = x_{12}(v_0) \tag{2.15}$$

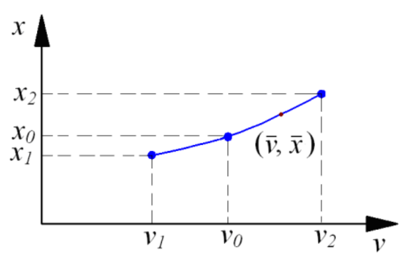

Figure 2.14. Figure assisting the proof of the curve alignment satisfaction.

Theorem: For any arbitrary point $(\bar{v}, \bar{x})$ that satisfies $v_0 < \bar{v} < v_2$ and $\bar{x} = x_{02}(\bar{v})$, we can write:

$$\bar{x} = x_{12}(\bar{v}) \tag{2.16}$$

Proof: From the conditions of the theorem, for x_0 and $\bar{x}$ we can write:

$$x_0 = x_{12}(v_0) = x_1 + \frac{x_2 - x_1}{f_r(v_2) - f_r(v_1)}\left(f_r(v_0) - f_r(v_1)\right) \tag{2.17}$$

$$\bar{x} = x_{02}(\bar{v}) = x_0 + \frac{x_2 - x_0}{f_r(v_2) - f_r(v_0)}\left(f_r(\bar{v}) - f_r(v_0)\right) \tag{2.18}$$

Utilizing Eq. (2.17) we have:

$$\begin{aligned}
\frac{x_2 - x_0}{f_r(v_2) - f_r(v_0)} &= \frac{x_2 - \left\{x_1 + \frac{x_2 - x_1}{f_r(v_2) - f_r(v_1)}\left(f_r(v_0) - f_r(v_1)\right)\right\}}{f_r(v_2) - f_r(v_0)} \\
&= \frac{(x_2 - x_1)\left\{1 - \frac{f_r(v_0) - f_r(v_1)}{f_r(v_2) - f_r(v_1)}\right\}}{f_r(v_2) - f_r(v_0)} = \frac{(x_2 - x_1)\left\{\frac{f_r(v_2) - f_r(v_0)}{f_r(v_2) - f_r(v_1)}\right\}}{f_r(v_2) - f_r(v_0)} \\
&= \frac{x_2 - x_1}{f_r(v_2) - f_r(v_1)}
\end{aligned} \tag{2.19}$$

Substituting Eqs. (2.17) and (2.19) into Eq. (2.18) yields:

$$\bar{x} = x_1 + \frac{x_2 - x_1}{f_r(v_2) - f_r(v_1)}\left(f_r(v_0) - f_r(v_1)\right) + \frac{x_2 - x_1}{f_r(v_2) - f_r(v_1)}\left(f_r(\bar{v}) - f_r(v_0)\right) \tag{2.20}$$

Simplifying Eq. (2.20) leads to the proof of the theorem as:

$$\bar{x} = x_1 + \frac{x_2 - x_1}{f_r(v_2) - f_r(v_1)}\left(f_r(\bar{v}) - f_r(v_1)\right) = x_{12}(\bar{v}) \tag{2.21}$$

As a result of this theorem, the satisfaction of curve alignment property by the proposed linear mapping strategy can be proved. For this, Figure 2.15 which demonstrates a typical hysteresis trajectory has been generated through a numerical simulation. It is seen from the figure that the trajectory initiated from Point #3 must align to Curve 1-2 at Point #2 and continue its path towards the next target point. It can be shown that to guarantee the satisfaction of curve alignment property, the following condition must hold:

$$x_{24}(v)H(v, v_2, v_4) = x_{14}(v)H(v, v_2, v_4) \tag{2.22}$$

Since point (v_2, x_2) satisfies the conditions $v_1 < v_2 < v_4$ and $x_2 = x_{14}(v_2)$, for any arbitrary point (v, x) that satisfies $v_2 < v < v_4$ and $x = x_{24}(v)$, it follows that $x = x_{14}(v)$. Therefore, the fulfillment of curve alignment property is guaranteed.

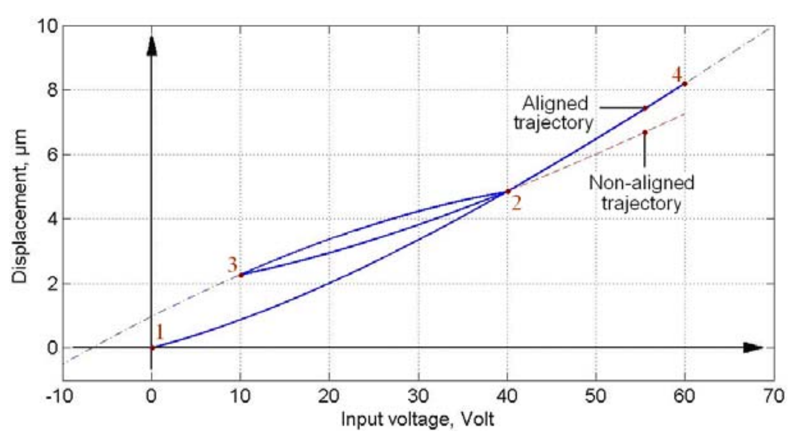

Figure 2.15. Targeting turning point and curve alignment property.

The implementation of the proposed model requires two explicitly known ascending and descending reference functions. Here, two third order polynomials are utilized for the approximation of ascending and descending reference curves due to their sufficient accuracy in capturing the unsaturated region of piezoelectric actuator operation. The polynomials representing the ascending and descending hysteresis reference curves are expressed as:

$$f_a(v) = \sum_{i=0}^{3} a_i v^i = a_0 + a_1 v + a_2 v^2 + a_3 v^3 \tag{2.23}$$

$$f_d(v) = \sum_{i=0}^{3} d_i v^i = d_0 + d_1 v + d_2 v^2 + d_3 v^3 \tag{2.24}$$

where a_i and d_i are the shaping coefficients that can be identified through a least square error minimization or similar algorithms.

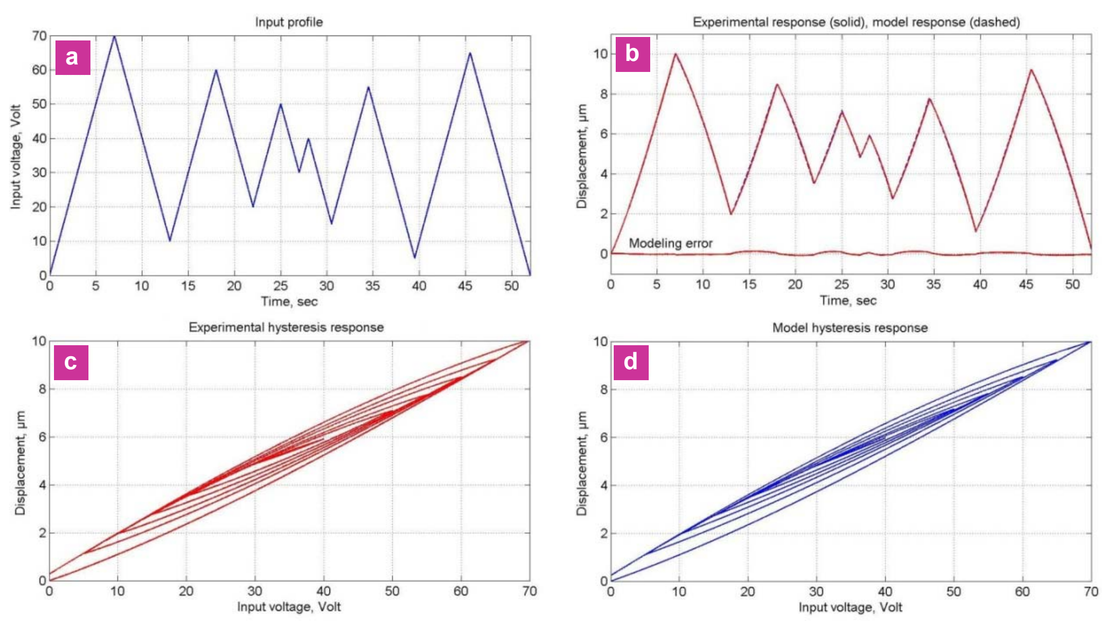

Figure 2.16. Experimental verification of the proposed hysteresis model; (a) input profile, (b) experimental time response (solid line) and model time response (dashed line), (c) stage hysteresis response, and (d) model hysteresis response.

A ± 10 Volt/sec input profile is designed such that the model requires at least five memory units for the accurate prediction of hysteresis trajectory. The experimental and memory-based model responses are demonstrated in Figure 2.16. It is seen that the proposed model is able to accurately predict the multiple-path hysteretic response of the stage. The maximum and RMS (root-mean-square) error percentages are obtained as 1.27% and 0.61%, respectively.

2.3.4. Memory Allocation Strategies

It was demonstrated that precise prediction of hysteresis trajectory requires a number of memory units to store the target points in the hysteresis path. In this section, the concept of memory-allocation strategy is introduced, and the behavior of the model with saturated memory is presented and discussed.

Two events are important for the memory-allocation process: (i) the time that the direction of input changes and a turning point is recorded; and (ii) the time that the trajectory hits and passes a target point, which coincides with the curve alignment and wiping-out events. Figure 2.17 graphically demonstrates the memory-allocation strategy. In this figure, five memory units are included in the model. The circles contain the location of different untouched turning points which have been recorded. When the direction of the input changes, all memory occupants shift rightward by one step and the new turning point is recorded in the memory (see Figure 2.17(a)). When a target point is passed by the hysteresis trajectory, that point is eliminated from the memory unit, and all other target points move leftward by one step, to be utilized for the prediction of the future path (see Figure 2.17(b)). It is remarked that the symbols inside the circles (e.g., triangle, rectangle, etc.) are used to show the location of different turning points (e.g., v_i and x_i) in the hysteresis history.

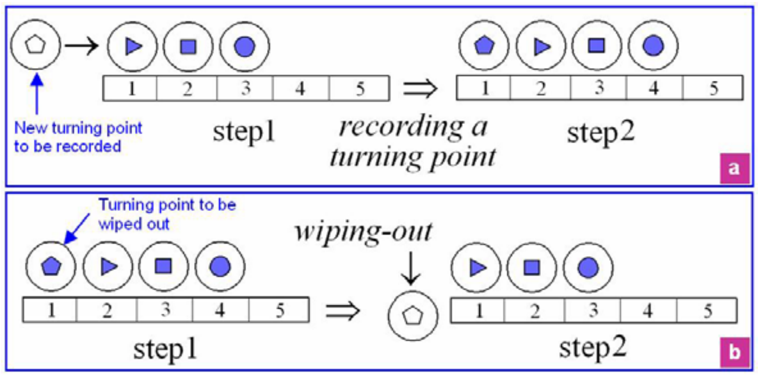

Figure 2.17. Memory-allocation strategy; (a) recording and (b) wiping-out turning points.

It is important to note that the first and the *always-available* memory occupants (in case of sufficient memory units) are the points corresponding to the maximum and the minimum input thresholds (in Figure 2.17, this point corresponds to the unit with the circle sign inside). Since these points are never passed by the trajectory, they are not wiped out. However, if the memory units are not sufficiently included, by recording the turning points memory gets saturated, and therefore, further recording leads to loosing the untouched targets including these threshold points. To investigate the influence of memory saturation on the model response, two cases of interest are discussed next.

Open memory-allocation strategy

In this strategy, by recording a new turning point (unit corresponding the hexagon sign in Figure 2.18(a)), the most distant target (unit corresponding the circle sign) is eliminated, other occupants shift rightward, and the new point is recorded in the memory. Since the most distant targets are eliminated, model loses some information of the hysteresis history. Yet, trajectory is predictable until model needs the lost targets. Hysteresis trajectory diverges from the real path when it hits the last and the only target point. Since there are no other targets, hysteresis trajectory loses its correct path and diverges from it. Furthermore, the trajectory may break the reference curves and escape from the hysteresis borders that could lead to large modeling errors.

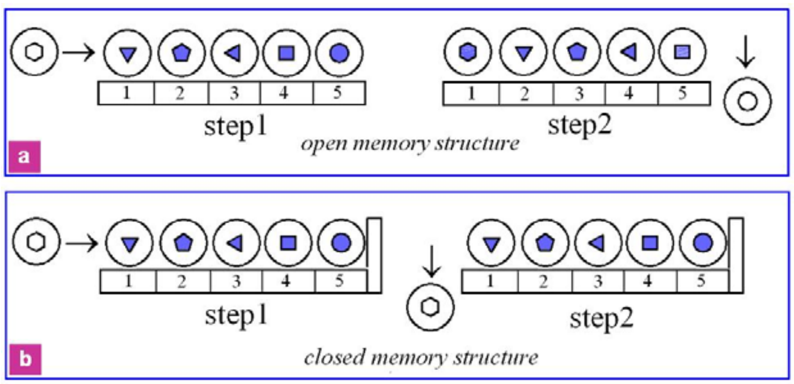

Figure 2.18. Saturated memory function; (a) open and (b) closed memory-allocation strategies.

To demonstrate the performance of the open memory-allocation strategy in the event of memory saturation, a simulation study is carried out here. Input profile shown in Figure 2.19(a) is applied to the hysteresis model with one, two and three memory units. For the given input profile, *three memory units* are required for the prediction of the hysteresis path. Therefore, the model with three memory units is considered as the ideal model to which the other two are compared. As seen from Figure 2.19, as the number of memory units gets closer to the minimum required number, model performance improves.

Hysteresis trajectory diverges from the correct trajectory when it passes the first and the second dominant extrema for the models with one and two memory units, respectively. Although the response is precise for the initial time interval, it diverges from the original path after passing the related dominant extremum and does not converge again. The straight dashed lines in Figures 2.19(c) and 2.19(d) demonstrate the time when the trajectory diverges.

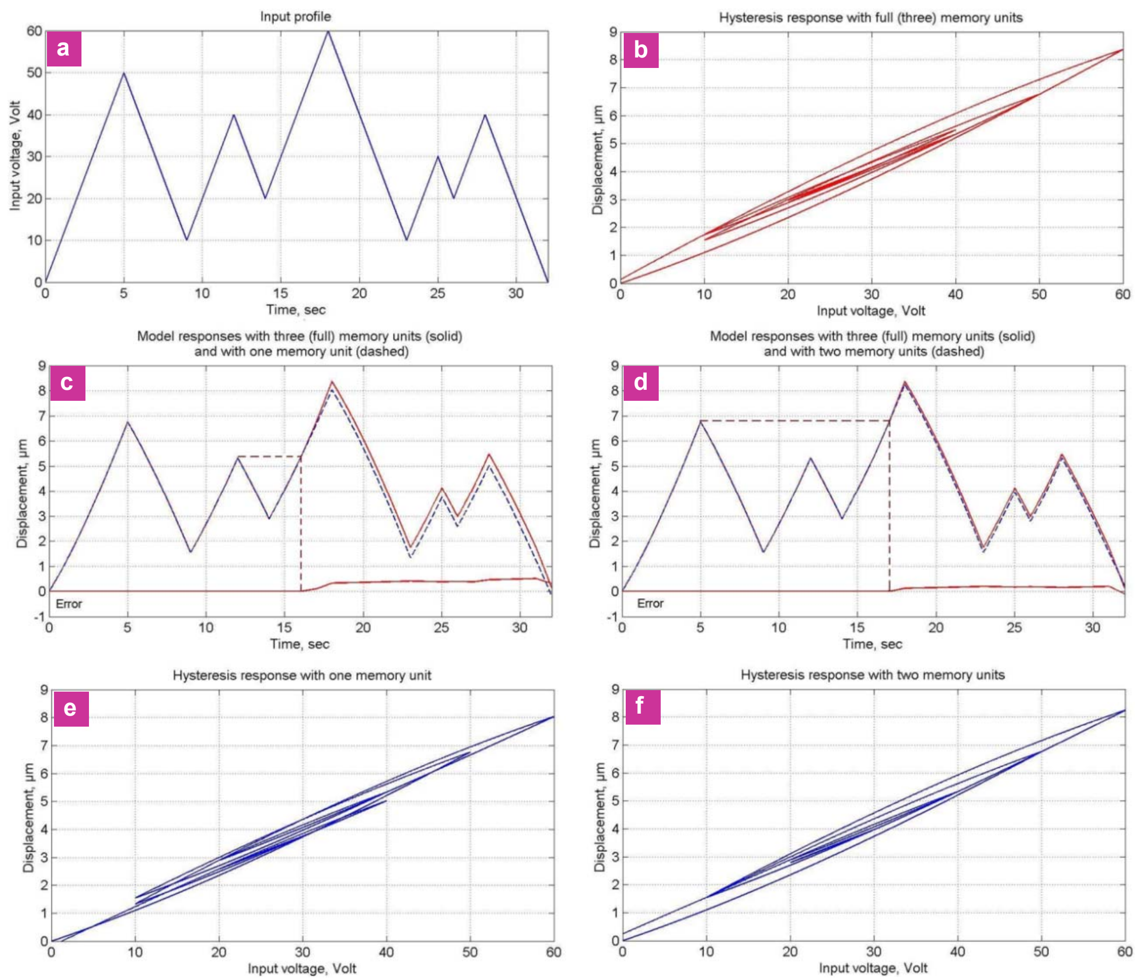

Figure 2.19. Open memory-allocation performance; (a) input profile, (b) hysteresis with full memory units; model responses with (c) one memory unit and (d) two memory units; hysteresis responses with (e) one memory unit, and (f) two memory units.

Closed memory-allocation strategy

The objective of developing a closed memory-allocation strategy is to reduce the modeling error by bounding the response with the reference curves. In this strategy, if a new turning point is made, the memory-allocation strategy does not permit the turning point to be recorded. Therefore, the most distant targets are safely kept in the memory, and closer targets are lost (see Figure 2.18(b)). In contrary to open memory-allocation strategy, the diverged trajectory may converge back, as the important targets including the upper and the lower threshold points are maintained.

Figure 2.20 demonstrates performance enhancement of the model through the closed memory-allocation strategy. As seen from this figure, models with one and two memory units with closed strategy have significantly less error than those with open strategy shown in Figure 2.19. Furthermore, the hysteresis trajectory is always bounded by the reference curves, and the modeling error jumps up and down around zero. Compared to the open strategy, the trajectory diverges earlier, but may converge back; this happens for the case of two memory units as shown in Figure 2.20(b). The dashed lines show the location of the trajectory divergence, and the dash-dotted lines show the points where the trajectory converges back. For the case with one memory unit, the convergence would have been occurred if the trajectory had arrived at the upper or lower threshold points. In conclusion, closed memory-allocation strategy presents more stable and effective prediction of hysteresis loops compared to the open strategy in the event of memory saturation. This can be better realized from Table 2.3, where the RMS error percentages for both open and closed strategies are listed.

Table 2.3. RMS error percentages for models with one and two memory units and with closed and open memory-allocation strategies.

RMS error percentages	Model error with one memory unit	Model error with two memory units
Open memory-allocation	3.28 %	1.33 %
Closed memory-allocation	1.04 %	0.23 %

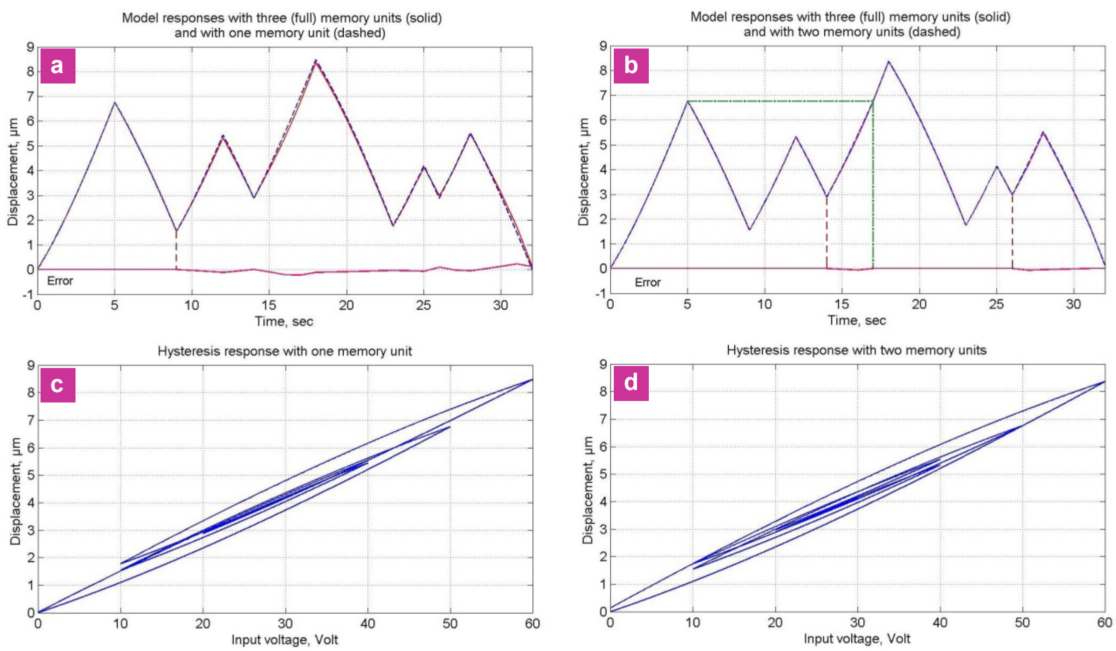

Figure 2.20. Closed memory-allocation performance; model responses with full and (a) one memory unit, and (b) two memory units; hysteresis responses with (c) one memory unit, and (d) two memory units.

2.3.5. Feedforward Hysteresis Compensation with Exponential Memory-based Mapping

Feedforward controllers operate based on the inverse plant model to remove the nonlinear effect and generate a relatively linear response. Generally, two methods are utilized to find the inverse model of hysteresis: (1) analytical approaches that systematically present the inverse model using the identified direct model [44], and (2) numerical methods that find the inverse of the hysteresis utilizing numerical techniques [27].

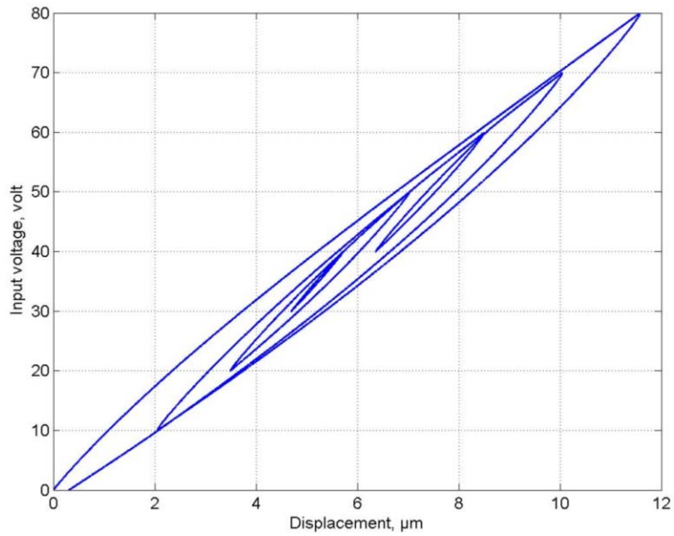

Figure 2.21. Inverse hysteresis response.

A direct method for obtaining the inverse hysteresis model for the feedforward control strategy is proposed here. As seen from Figure 2.21, the inverse hysteresis response can be obtained by plotting the input voltage versus the resultant displacement. The inverse response is also of hysteretic type with the same intellectual properties. The differences are, however, in the characteristics of reference curves and the inversion of input/output axes. The inverse hysteresis formulation can be then expressed as:

$$v_A(x) = F^{-1}(x, x_{L1}, v_{L1}, x_{U1}, v_{U1}) H(x, x_{L1}, x_{U1}) + \sum_{i=1}^{n} F_{Ai}^{-1}(x) H(x, x_{Ui}, x_{U(i+1)}) \tag{2.25}$$

$$v_D(x) = F^{-1}(x, x_{U1}, v_{U1}, x_{L1}, v_{L1}) H(x, x_{L1}, x_{U1}) + \sum_{i=1}^{n} F_{Di}^{-1}(x) H(x, x_{L(i+1)}, x_{Li}) \tag{2.26}$$

$$F^{-1}(x, x_1, v_1, x_2, v_2) = k'(1 + a' e^{-\tau'(x - x_1)})(x - x_1) + v_1 \tag{2.27}$$

$$k' = \frac{v_2 - v_1}{x_2 - x_1}(1 + a'e^{-\tau'(x_2 - x_1)})^{-1} \tag{2.28}$$

Equations (2.25) and (2.26) represent inverse ascending and descending curves, respectively. Equations (2.27) and (2.28) describe the proposed exponential form of the hysteresis curves, with a' and τ' being the shaping parameters of the inverse model.

To demonstrate the effectiveness of the feedforward memory-dominant inverse controller, a $\pm 1\mu\text{m/sec}$ desired trajectory signal is generated and fed into the controller (see Figure 2.22 for the control strategy). This trajectory requires at least four memory units. The inverse model parameters a' and τ' are identified as -0.46 and -0.20 for the ascending and -0.68 and 0.18 for the descending reference curves, respectively. The system responses to the inverse controller with different memory units and the best linear controller are depicted in Figure 2.23. The best linear controller is designed by fitting a line into the inverse hysteresis response of the nanopositioning stage obtained with the best feedforward controller for a specific trajectory. As seen from the figure, the controller response is improved as the number of memory units increases to the minimum required number. Maximum and mean square tracking errors are listed in Table 2.4 for comparison. It is remarkable to note that the inverse controller with one memory unit demonstrates even worse performance than the linear controller for this specific trajectory. This is due to the fact that system response diverges from the desired trajectory after passing the first dominant extremum, which is located in the initial interval of the desired trajectory span. However, the hysteresis nonlinearity is reduced from 14.1% to 1.0% for the controller with four memory units.

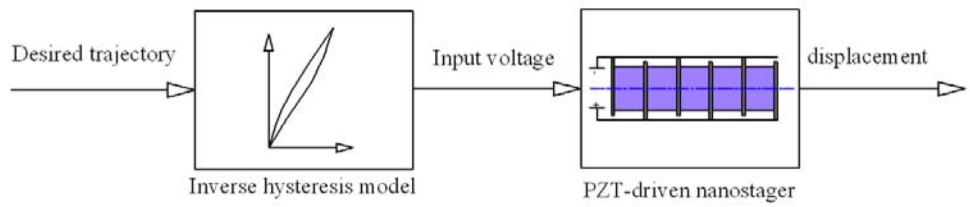

Figure 2.22. Feedforward control strategy based on the inverse hysteresis model.

Table 2.4. Maximum and mean-square tracking error values for linear controller and feedforward inverse controller with different memory units.

Controller type	Maximum error (%)	Mean square error ($\mu m^2 sec$)
Proportional controller	7.43	12.32
Inverse controller with one memory unit	8.66	17.06
Inverse controller with two memory units	1.90	0.28
Inverse controller with three memory units	1.27	0.11
Inverse controller with four or more memory units	1.04	0.07

The proposed controller could also be successfully utilized for rate-varying input signals. Although the hysteresis rules derived here are for a constant rate input, as long as the rate operating is close to the rate at which the model has been identified, the controller exhibits improved performance. Figure 2.24 depicts the trajectory tracking results of the system for a multi-frequency sinusoidal desired trajectory ($x_d(t) = 6 - 0.45\cos(1.4\pi t) - 1.50\cos(0.6\pi t) - 1.80\cos(\pi t) - 2.25\cos(2\pi t)$, μm). A feedforward memory-dominant inverse controller with sufficient memory units (three units here) is compared with the best linear controller. As clearly seen, the hysteresis nonlinearity is reduced from 15.5% to 1.6% by the utilization of the proposed inverse controller for this trajectory.

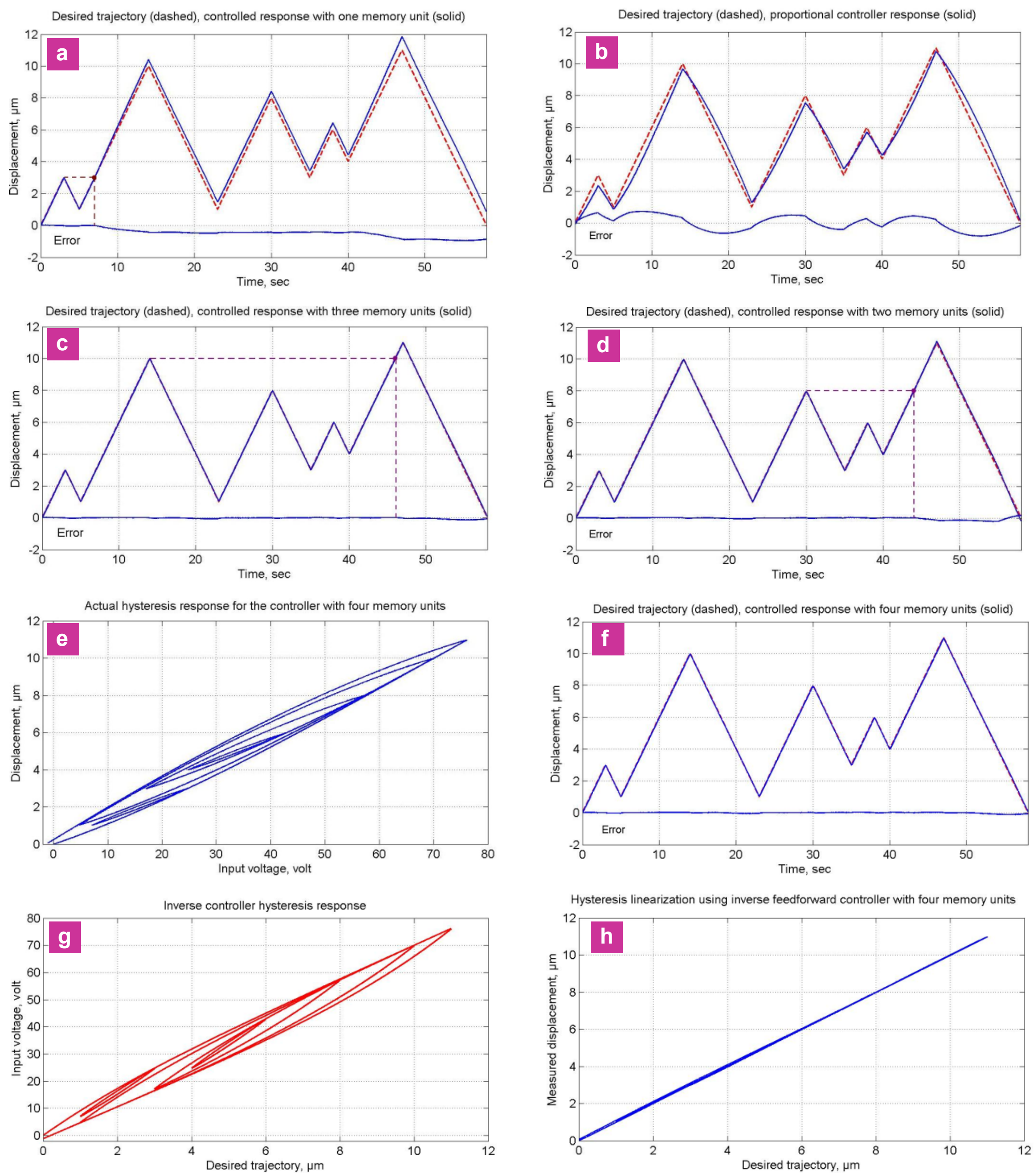

Figure 2.23. Inverse feedforward controller results; (a) linear controller response, inverse controller response with (b) one memory unit, (c) two memory units, (d) three memory units, and (e) four or more memory units, (f) actual hysteresis response for the controller with four memory units, (g) inverse hysteresis response of the controller with four memory units, and (h) linearized response using the controller with four memory units.

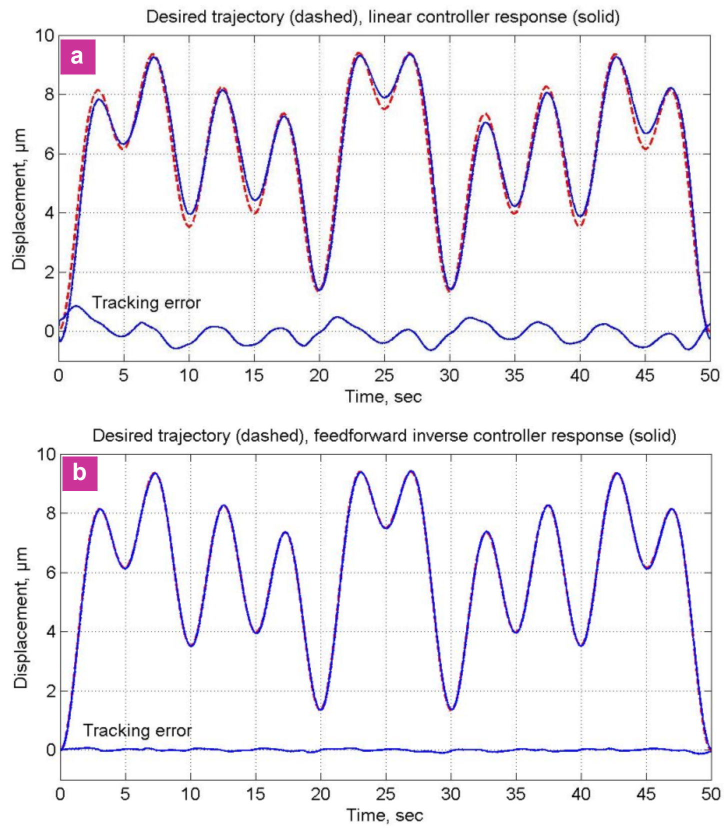

Figure 2.24. Tracking control of a multi-frequency sinusoidal trajectory; (a) linear proportional controller response, (b) memory-base inverse controller response.

Chapter Summary

Low frequency open-loop tracking control of piezoactive micro and nanopositioning systems is limited by the multi-loop history-dependent hysteresis phenomenon associated with their applied input voltage and resultant output displacement. Both conventional phenomenological and constitutive models lack accuracy either due to the rigidity of the frameworks or lack of knowledge on the memory-based properties of hysteresis. In this chapter, both phenomenological and constitutive frameworks were targeted for possible improvements or development of new modeling frameworks. More specifically, a modification has been applied to the conventional PI hysteresis operator, one of the widely-used phenomenological frameworks, to improve its accuracy. Experimental comparisons on a PZT-driven nanopositioning stage demonstrated significant enhancement in the accuracy of the proposed modified PI model.

A novel memory-based constitutive modeling framework was then proposed to precisely predict the hysteresis phenomenon. The model utilized a set of intelligent properties of hysteresis that were experimentally observed and identified. These properties were incorporated into a mathematical mapping technique with two different linear and exponential configurations. Superior results were obtained using the proposed framework in modeling and feedforward control of a piezoactive nanopositioning system. The necessary condition for the accuracy of the positioning is for the model to include a sufficient number of memory units for recording important data from the history of hysteresis trajectory.

CHAPTER THREE

LUMPED-PARAMETERS MODELING AND CONTROL OF PIEZOACTIVE MICRO- AND NANO-POSITIONING SYSTEMS

3.1. Introduction

High frequency control of piezoactive micro- and nano-positioning systems requires a comprehensive and detailed model of the system frequency-dependent dynamics. Due to distributed-parameters nature, these systems are well described by partial differential equations [29]. In practice, however, the working frequencies of piezoactive positioning systems barely exceed their first natural frequency. Therefore, their distributed-parameters dynamics could be safely reduced to a lumped-parameters representation, especially when integrated with flexural mechanical compartments. In many references, a second order linear time-invariant model has been integrated with a hysteresis operator appeared in the input excitation for describing the system hysteretic and frequency-dependent behavior [26, 38].

Typically, hysteresis models have complicated structures due to the multiple-loop and memory-dependent behavior of the phenomenon. One way to avoid hysteresis is to use charge-driven circuits such that the input charge can be applied in a controlled way. It has been shown that the relation between applied charge and displacement is linear in piezoelectric materials [45, 46]; however, the need for expensive instrumentation, amplification of the measurement noise, and reduction in the system responsiveness are the main drawbacks of charge-driven strategy. Hence, many applications prefer to use voltage-driven strategy and compensate hysteresis effect with inverse models.

Control of piezoactive systems can be divided into feedforward and feedback strategies. Feedforward schemes essentially employ an inverse hysteresis model to compensate for this phenomenon which is the dominant source of inaccuracy in low-frequencies [21, 22, 27 and 28]. However, to compensate for the effects of frequency-dependent dynamics, rate-dependent hysteresis model are proposed [44]. The overall uncertainties of the feedforward methods and the presence of external disturbances, however, necessitate the use of feedback control, particularly at higher frequencies. Many feedback schemes utilize a PID (Proportional-Integral-Derivative) controller to overcome the drawbacks of feedforward compensators [23, 28]. Although significant improvements are achieved in low frequencies, a continuous increase in tracking error is observed as the frequency increases.

On the other hand, various systematic methods such as robust and adaptive control schemes have been developed, most of which require a representative hysteresis model [26, 32]. Some robust control schemes, however, do not require a hysteresis model [47, 48]; although performance is improved compared to classical methods, parametric uncertainties have not been taken into account. The fact that a robust controller loses its performance to compensate for disturbances originated from parametric uncertainties elucidates the need for robust adaptive methods when high performance operations are demanded. It is well known that asymptotic robust schemes such as sliding mode control are not practical due to the chatter phenomenon [49], but adaptive methods are able to completely eliminate or significantly reduce the effects of uncertainties in the system parameters [50]. Few works have addressed robust adaptive scheme together in their control design but mainly have focused on the theoretical aspects [51, 52]. The control problem becomes even more challenging when the system is subjected to other sources of uncertainties such as cross-coupling effect in multiple axes operation.

In this chapter, a combined hysteretic and dynamic model is proposed for accurate modeling of piezoactive positioning systems in a broad frequency range. Through a set of experiments it is shown that the model sustains a good level of accuracy compared to the pure hysteretic and pure dynamic models. A feedforward control law is then proposed for tracking time-varying trajectories at various rates. To improve the precision of operation with the advantage of real-time position feedback, a Lyapunov-based robust adaptive controller is developed and implemented on a XY parallel piezo-flexural nanopositioning stage with cross-coupling effect. It has been demonstrated that the controller forces the stage to precisely track low and high-frequency trajectories despite the absence of hysteresis model and the presence of parametric uncertainties.

3.2. Lumped-Parameters Modeling of Piezoactive Nanopositioning Systems

Piezoelectric actuators typically consist of stack of thin layers of electro-active solid-state materials, alternatively connected to the positive and negative terminals of a voltage source (Figure 3.1-left). The total displacement of the actuator is determined as the sum of the expansions of the individual layers. As stated before, due to the high natural frequency of system, a reduced lumped-parameters representation could effectively cover the actual system response in a reasonably broad frequency range.

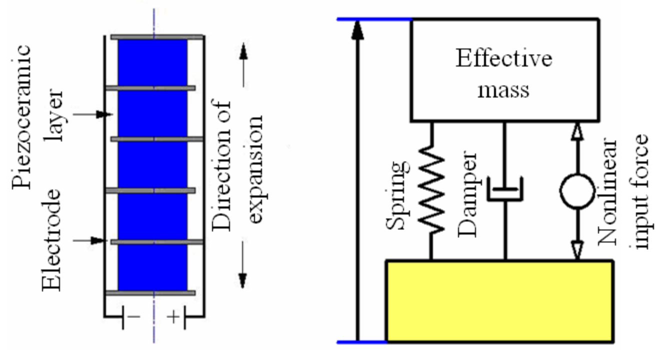

Figure 3.1. (left) Schematic of a typical piezoelectric stack actuator, and (right) its equivalent dynamic model.

3.2.1. Mathematical Model Description

The proposed model combines a mass-spring-damper trio with a nonlinear hysteresis operator appearing in the input excitation to the system (see Figure 3.1-right). The governing equation of motion for such system is then written as:

$$\ddot{x}(t) + 2\xi\omega_n\dot{x}(t) + \omega_n^2 x(t) = \omega_n^2 H\left\{v(t)\right\} \tag{3.1}$$

where $x(t)$ and $v(t)$ represent the actuator displacement and input voltage, respectively; ζ and ω_n are the damping coefficient and natural frequency of the linear dynamic, respectively, and $H\{v(t)\}$ is a scaled hysteretic relation between the input voltage and the excitation force.

To evaluate the contribution of the hysteretic and the dynamic models independently, three other possible models are considered to be compared with the proposed integrated model. The models are given by:

$$x_1(t) = av(t) \tag{3.2}$$

$$x_2(t) = H\left\{v(t)\right\} \tag{3.3}$$

$$\ddot{x}_3(t) + 2\xi\omega_n\dot{x}_3(t) + \omega_n^2 x_3(t) = a\omega_n^2 v(t) \tag{3.4}$$

where $x_1,(t)$, $x_2(t)$ and $x_3(t)$ denote the piezoactive system models responses to the given input voltage $v(t)$, respectively. The model given in Eq. (3.2) presents a linear relation between the input voltage and the stage displacement, Eq. (3.3) proposes a pure static hysteretic relation between the input voltage and the stage displacement, and Eq. (3.4) presents a pure dynamic model for the stage without considering its hysteretic behavior.

Because of high stiffness and thus high natural frequency of piezoactive systems, in low-rate and low frequency operations where the velocity and acceleration terms $\dot{x}(t)$ and $\ddot{x}(t)$ are small, the effects of first two terms in Eq. (3.1), i.e. inertia and damping terms become negligible. Therefore, Eq. (3.1) can be safely reduced to Eq. (3.3), and Eq. (3.4) can be accordingly reduced to Eq. (3.2). It is expected that for low-frequency operation, Eq. (3.3) can precisely predict the system response if a valid hysteresis model is utilized, however, Eqs. (3.2) and (3.4) fail to accurately predict the response. In high-frequency operation, Eq. (3.3) should fail to precisely predict the system response, as the effects of system dynamics have been neglected. Similar to low-frequency operation, Eq.

(3.4) lacks the needed precision because the hysteresis effect is ignored, but the response accuracy remains insensitive to the variation of input rate and frequency as the dynamics is incorporated. The simplest model is the proportional model described by Eq. (3.2), which is expected to demonstrate the least levels of accuracy and performance for both low and high-rate inputs.

3.2.2. Experimental Verification

To demonstrate the effectiveness of the proposed modeling framework and observe the effects of dynamic and hysteresis models on the accuracy of the response, two low- and high-rate (± 10 and ± 1000 Volt/sec) triangular inputs with the same profiles are generated and implemented on a piezo-flexural nanopositioning system depicted in Figure 3.6. The memory-based hysteresis model proposed in Chapter 2 is developed and implemented in the system. Figure 3.2 depicts the low-rate experimental comparison of the system response with the responses of the models described by Eqs. (3.1) to (3.4). From the similarity of the responses of Figures 3.2(a) with 3.2(c), and 3.2(b) with 3.2(d), it can be concluded that the effects of system dynamics are negligible for the low-rate operation. Figure 3.3 demonstrates the high-rate response of the models compared to that of the actual system. It can be clearly understood that only the proposed combined hysteretic dynamics model can precisely estimate the actual system response. Other models lack accuracy because of ignoring either hysteresis, or dynamics or both of them.

It is obvious that for higher rate input excitation, the effect of system dynamics become more visible, while the effect of hysteresis nonlinearity remains the same. Figure

3.4 demonstrates the input/output hysteresis responses of the actual system and proposed model for the given low- and high-rate inputs. As seen from the figure, the hysteresis loops are expanded as the input rate increases, due to the further induced hysteresis from the system damping. It is also seen from the figure that not only the proposed model precisely predicts the hysteresis response for the low-rate operations, but also effectively incorporates the effects of rate variation. To achieve a more visible assessment of the accuracy of the models, the mean-square and maximum error values of each model are calculated which are listed in Table 3.1.

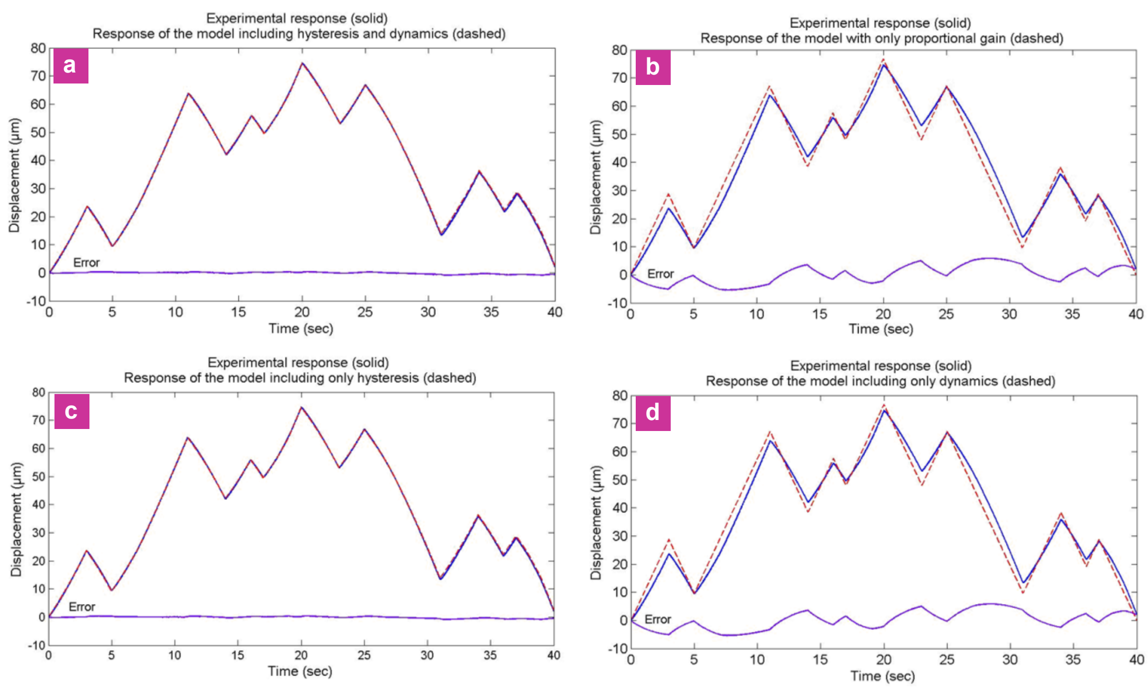

Figure 3.2: Low-rate response of the piezo-flexural system compared to responses of; (a) combined hysteretic and dynamics model, (b) proportional model, (c) pure hysteretic model, and (d) pure dynamic model.

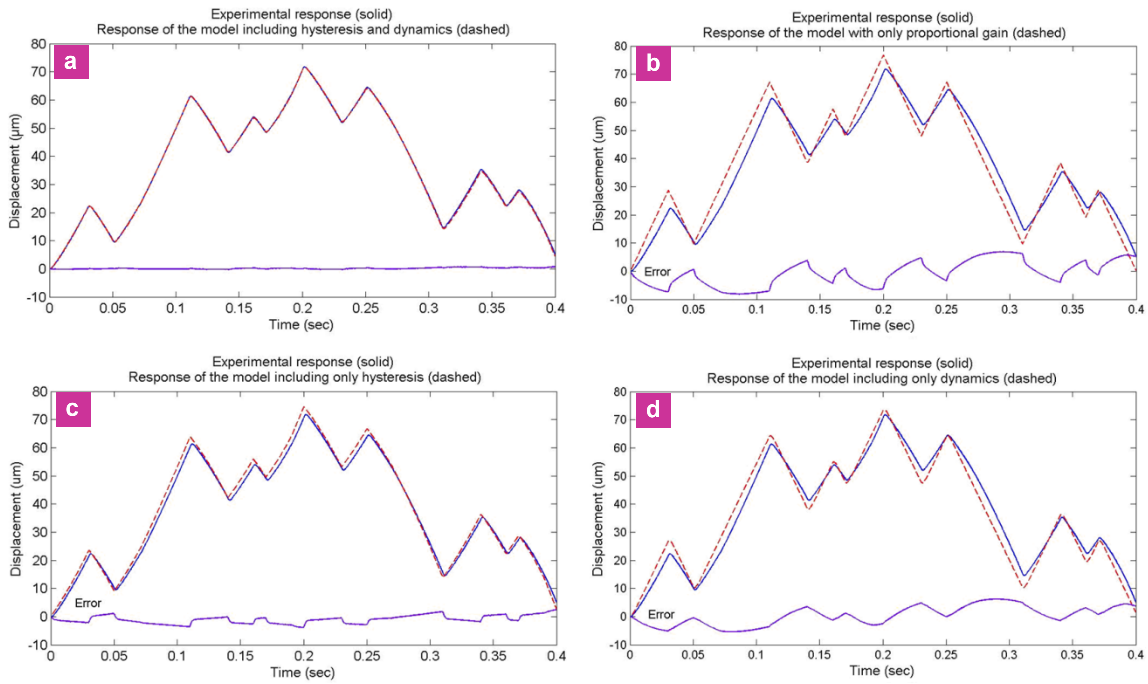

Figure 3.3: High-rate response of system versus responses of; (a) combined hysteretic and dynamic, (b) proportional, (c) pure hysteretic and (d) pure dynamic models.

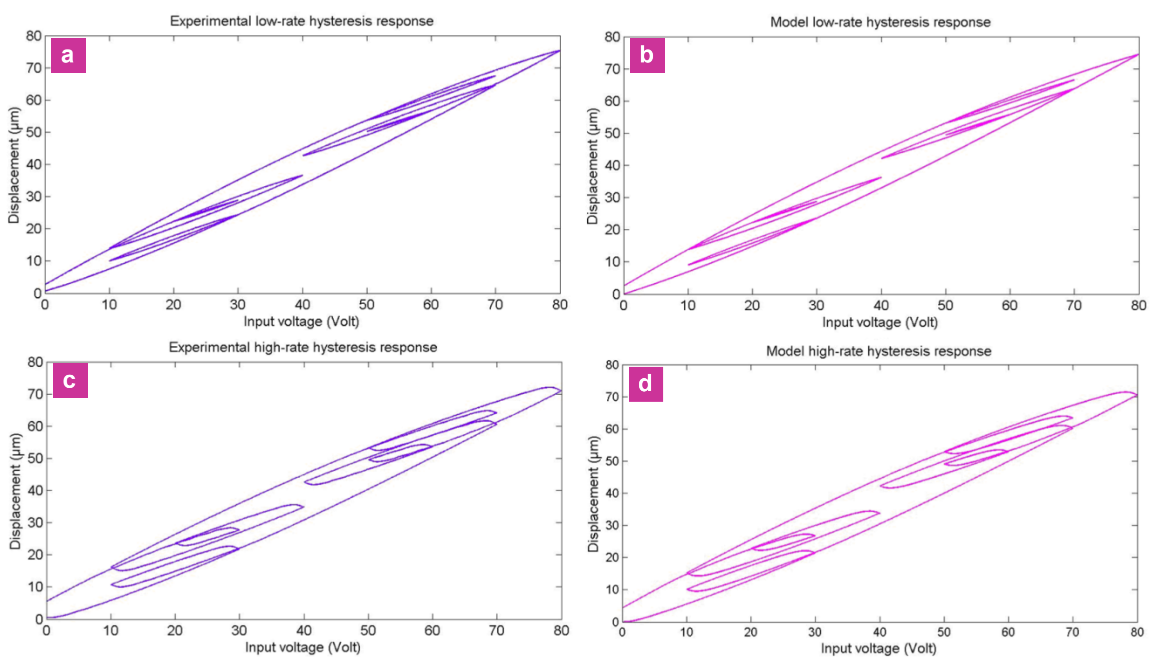

Figure 3.4: (a) Low-rate experimental, (b) low-rate model, (c) high-rate experimental and (d) high-rate model hysteresis responses of the actual and simulated system.

Table 3.1. Maximum and mean-square modeling error values for different models in low- and high-rate operations.

Model type	Low-rate input		High-rate input	
	Maximum error (%)	Mean-square error (μm)	Maximum error (%)	Mean-square error(μm)
Model including hysteresis and dynamics Eq. (3.1)	1.24	0.26	1.04	0.21
Model with only a proportional gain Eq. (3.2)	7.75	2.69	11.24	3.76
Model including only hysteresis nonlinearity Eq. (3.3)	1.22	0.26	5.40	1.48
Model including only dynamics Eq. (3.4)	7.73	2.68	8.60	2.84

3.3. Feedforward Control of Piezoactive Nanopositioning Systems

In this subsection, an inverse model-based feedforward controller is introduced and experimentally implemented for tracking control of multiple frequency trajectories. For this, a perturbation term is added to the system equation of motion to present a more actual description of the system dynamics as:

$$\ddot{x}(t) + 2\xi\omega_n\dot{x}(t) + \omega_n^2 x(t) = \omega_n^2 H\left\{v(t)\right\} + p(t) \tag{3.5}$$

where $p(t)$ is the influence of the parametric uncertainties, unknown terms and the ever-present unmodeled dynamics. A feedforward control law is proposed next for the system described by Eq. (3.5).

3.3.1. Feedforward Controller Derivation

Consider a feedforward control law given by:

$$v(t) = H^{-1}\left\{\frac{1}{\omega_n^2}\ddot{x}_d(t) + \frac{2\xi}{\omega_n}\dot{x}_d(t) + x_d(t)\right\} \tag{3.6}$$

with $x_d(t)$ being the two-times continuously differentiable desired trajectory. Substituting Eq. (3.5) into the system equation of motion, (3.5) results in the following error dynamics:

$$\ddot{e}(t) + 2\xi\omega_n\dot{e}(t) + \omega_n^2 e(t) = -p(t) \tag{3.7}$$

where $e(t) = x_d(t) - x(t)$ represents the tracking error. It can be interpreted from Eq. (3.7) that if the magnitude of the model perturbation $p(t)$ is bounded, the error signal remains bounded, and the feedforward controller leads to a uniformly stable tracking. This is due to the fact that the coefficients of system error and its first and second time derivatives are positive, leading to a stable differential equation for the error dynamics. However, the magnitude of the error depends on the model perturbations which appear as a forcing disturbance to the second order error dynamics. In low-frequency operation, such perturbation essentially originates from the hysteresis model inaccuracy, while in high-frequencies the dynamic model inaccuracy adds to the perturbations. An experimental test is carried out next to demonstrate the effectiveness of the proposed controller.

3.3.2. Experimental Verification of the Feedforward Controller

Tracking performance of the controller is examined on the piezoactive nanopositioning stage depicted in Figure 2.4 for three different multiple frequency trajectories as shown in Figure 3.5. The modified PI hysteresis operator proposed and identified in Chapter 2 is utilized in the controller. In order to evaluate the effectiveness of the proposed strategy, a proportional controller, which operates based on a single input/output conversion gain is tested and compared with the inverse feedforward controller for the given trajectories. The detailed profile of the desired trajectories and the maximum and mean-square values of the tracking error are all given in Table 3.2. The practical application of such trajectories could include trajectories used in Scanning Probe Microscopes (SPMs) which are utilized for topography tracking of uniform and non-uniform surface profiles.

Experimental results depicted in Figure 3.5 and Table 3.2 clearly indicate that the inverse feedforward controller is able to significantly suppress the tracking error originated from hysteresis nonlinearity and system dynamics in both low- and high-frequency operations. The results for the proportional controller demonstrate, however, that if the frequency of operation increases, the tracking error increases as well. This is simply due to the fact that the dynamics of the system are ignored in this controller.

Table 3.2. Trajectory profiles and tracking error values for feedforward control strategy.

Desired trajectory profile (μm)	(Exp. run), Controller	Maximum error (%)	Mean-square error (μm)
$4 - [\cos(2\pi t) + \cos(6\pi t) + \cos(10\pi t) + \cos(20\pi t)]$	(a) Inverse FF	2.34	0.04
	(b) *Proportional FF*	*8.03*	*0.23*
$4 - [\cos(20\pi t) + \cos(30\pi t) + \cos(80\pi t) + \cos(100\pi t)]$	(c) Inverse FF	2.70	0.06
	(d) *Proportional FF*	*10.92*	*0.27*
$4 - [\cos(60\pi t) + \cos(100\pi t) + \cos(140\pi t) + \cos(200\pi t)]$	(e) Inverse FF	2.12	0.05
	(f) *Proportional FF*	*16.66*	*0.32*

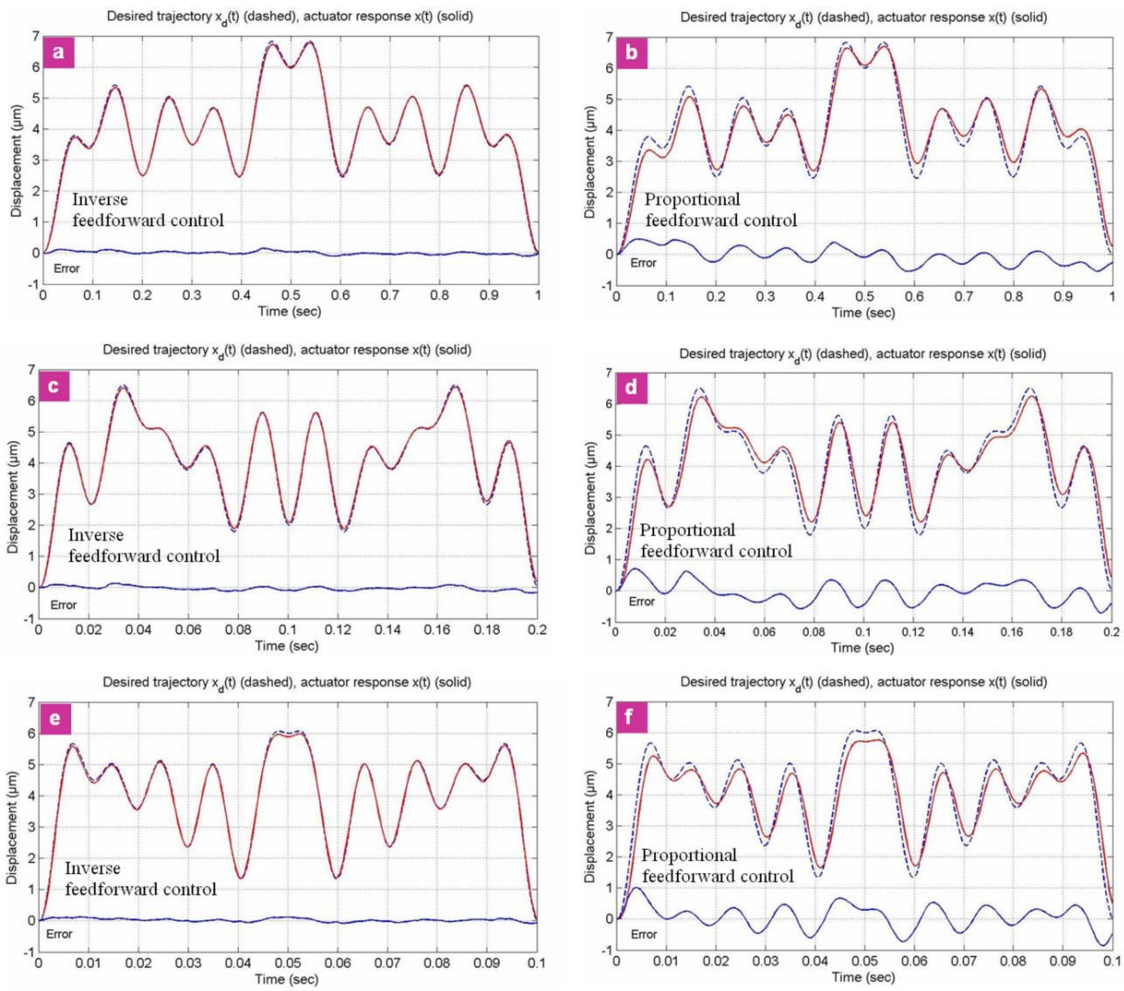

Figure 3.5. Multiple frequency feedforward trajectory tracking results for; (a) low-frequency inverse feedforward, (b) low-frequency proportional, (c) moderate-frequency inverse feedforward, (d) moderate-frequency proportional, (e) high-frequency inverse feedforward, and (f) high-frequency proportional control results.

3.4. Feedback Control of Piezoactive Nanopositioning Systems

The feedback availability of the real-time position can serve to significantly improve the control performance compared to the feedforward control schemes. Particularly, when the parametric uncertainties effectively disturb the system at high-frequencies and incorporation of complex hysteresis models is not preferred, the use of position feedback becomes inevitable for the precision control purpose. However, the development of an effective feedback controller makes the main challenge in this respect.

In this subsection, a Lyapunov-based robust adaptive control strategy is developed and utilized for precision tracking control of a double axes parallel piezo-flexural nanopositioning stage. This system not only suffers from the hysteresis nonlinearity and parametric uncertainties associated with its piezoelectric and dynamic structure, it also experiences a disturbance-like cross-coupling effect between its two axes when they are simultaneously excited.

3.4.1. System Description and Experimental Setup

Piezo-flexural systems have been developed to respond to the demand for multiple-axis micro- and nano-scale motions for a wide range of displacements. They comprise of several piezoelectric stack actuators, usually made of PZT connected to a flexural mechanism to handle the multiple-axis motion for a single moving stage. A flexure is a frictionless mechanism which operates based on the elastic deformation of a solid part made of a stiff metal providing maintenance-free and perfectly guided motion without any stick-slip effect.

A Physik Instrumente P-733.2CL double-axis parallel piezo-flexure stage with high resolution capacitive position sensors is considered here for the experiments (see Figure 3.6). Experimental data interfacing is carried out through the Physik Instrumente E-500 chassis for PZT amplifier along with DS1103 dSPACE® data acquisition and controller board. The sampling frequency of all experiments is set to be 20 kHz, and the stage motion is reflected by two built-in capacitive sensors with sub-nanometer resolution.

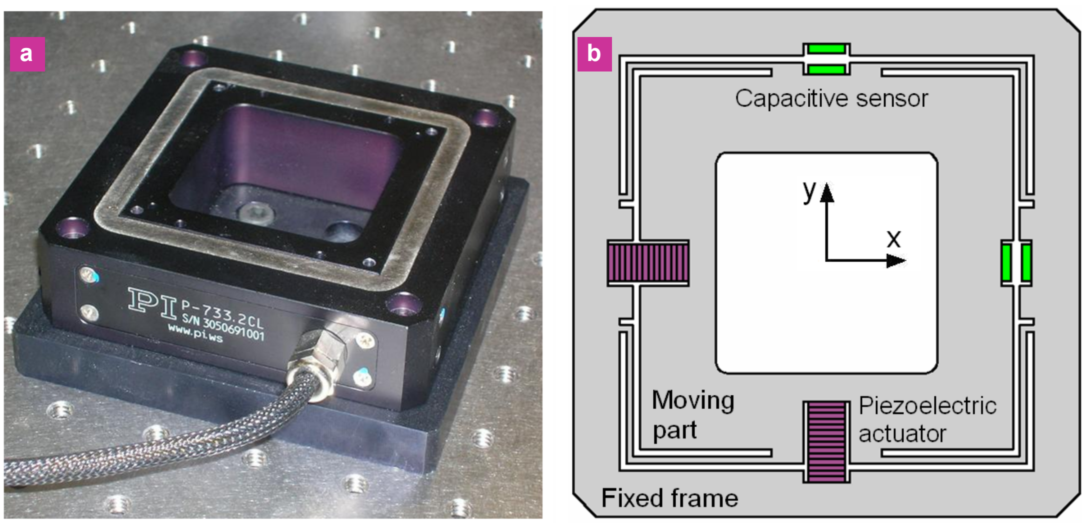

Figure 3.6. Parallel piezo-flexural system configuration; (a) Physik Instrumente P-733.2CL double-axis parallel piezo-flexure stage for the experiments, and (b) its schematic representation.

Figure 3.6(b) depicts the schematic configuration of the system. Two piezoelectric stacks are preloaded by a wire-cut flexural stage with the ability to push in two perpendicular directions and generate a simultaneous double-axis motion. Since both actuators move a single stage, the system configuration is called *parallel-kinematics*. In addition to accurate positioning, this system has the advantage of identical resonant frequencies and dynamic behavior in both directions.

3.4.2. The Cross-coupling Effect in Double-axis Motion

Parallel piezo-flexural systems suffer from a nonlinear cross-coupling phenomenon which originates from the asymmetrical arrangement of the actuators. That is, when the stage moves in one direction, the actuator in the other direction, which is tightly compressed between the moving surface and the stationary part, may rotate and deform due to the strong preload and the frictional forces. The piezoelectric stacks, on the other hand, may slip on each other due to the generated shear force. The combined rotation, compression and slip effects influence the stage motion in other direction. This cross-coupling becomes even more disruptive at high-frequencies, particularly when it is close to the system natural frequency.

Figure 3.7(a) demonstrates the experimental coupling responses when one axis is neutral and the other one is excited with 1 Hz and 50 Hz harmonic inputs. It is observed that the couplings in two directions are similar but demonstrate different behavior in different frequencies. Comparing the coupling phenomenon with hysteresis, one can view their similar nature; however, the main difference can be in their input excitation sources; the input of hysteresis is the applied voltage, while coupling originates from the motion of other axis. Hence, we propose the following equation representing the coupling phenomenon for neutral axis when the other axis is under excitation:

$$\ddot{x}(t) + 2\xi\omega_n\dot{x}(t) + \omega_n^2 x(t) = \omega_n^2 C\{y(t)\} \qquad (3.8)$$

where $x(t)$ is the neutral axis displacement , $y(t)$ is the moving axis displacement, and $C\{y(t)\}$ is a nonlinear operator representing the coupling phenomenon. It is noticeable that about 0.3% of one axis motion is transferred into the other axis through this coupling. This may reduce the precision of open-loop and the stability of the closed-loop system if not effectively compensated.

When both axes are under simultaneous excitations, not only the hysteresis influences the response, but also the coupling phenomenon disturbs the performance. Figure 3.7(b) depicts hysteresis response of axis x for 1 Hz excitation when axis y is excited by 40 Hz input excitation. This shows that the motion of high-frequency axis induces a small-amplitude wave on the hysteresis response of the low-frequency axis.

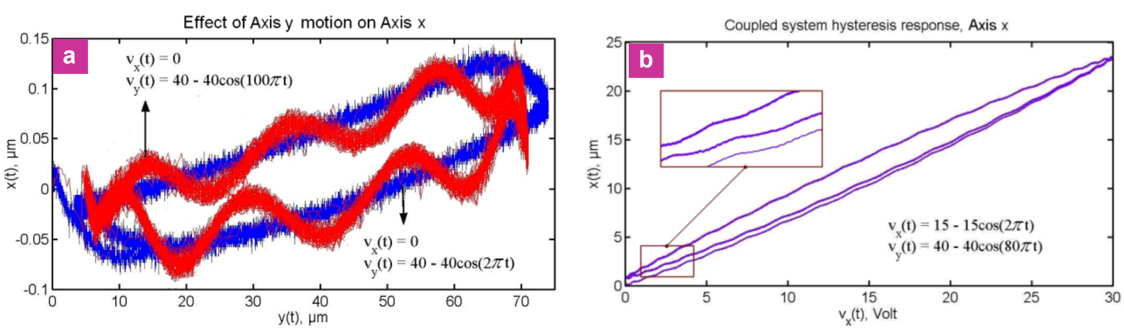

Figure 3.7. Cross-coupling effect of axis y motion on axis x: (a) when axis x is inactive while axis y is excited by 1 Hz and 50 Hz inputs, and (b) coupled hysteresis response of axis x in 1 Hz when axis y is excited by 40 Hz input; (similar responses are obtained for axis y as a result of axis x motion).

The governing equations of motion can now be obtained through the superposition of the hysteretic excitation and the coupling effect. Hence, the following pair of equations are proposed here for the double-axis motion of stage:

$$\begin{aligned} \ddot{x}(t) + 2\xi_x \omega_{nx} \dot{x}(t) + \omega_{nx}^2 x(t) &= \omega_{nx}^2 \left(H_x \left\{ v_x(t) \right\} + C_{yx} \left\{ y(t) \right\} + D_x(t) \right) \\ \ddot{y}(t) + 2\xi_y \omega_{ny} \dot{y}(t) + \omega_{ny}^2 y(t) &= \omega_{ny}^2 \left(H_y \left\{ v_y(t) \right\} + C_{xy} \left\{ x(t) \right\} + D_y(t) \right) \end{aligned} \tag{3.9}$$

where $D_{x/y}(t)$ represents the influence of the external disturbances on the system, with subscripts x and y specifying the parameters, operators, and inputs for the corresponding axis. Next, the widely used Proportional-Integral-Derivative (PID) controller is implemented for simultaneous tracking control of stage at different frequencies.

3.4.3. PID Controller Implementation

PID controller is a well-known strategy for precision control of mechanical systems. Choosing the proportional and integral control gains with trial and error, Figure 3.8 depicts tracking results when both axes are forced to simultaneously track desired trajectories with different frequencies and nonzero initial values. The desired trajectories include 60 μm peak-to-peak sinusoids in 5 Hz and 50 Hz for axis x and axis y, respectively. The achieved maximum steady-state tracking error is 1% for axis x and 20% for axis y. With further increasing gains for a better performance, system tends to instability. Although results indicate excellent steady-state tracking for the low-frequency trajectory, its transient response includes large overshoot and undesired oscillations. On the other hand, improving overshoot by tuning the gains decreases the steady-state tracking performance. Hence, PID controller lacks a desirable transient response in tracking of time-varying trajectories and has low performance in high frequency trajectory tracking.

It is remarked that for the same desired trajectories with *zero* initial values, about 0.7% (for axis x) and 8.3% (for axis y) maximum tracking errors can be achieved. Again, PID control is unable to track high-frequency trajectories, although, it is excellent for low-frequency trajectories with zero initial values.

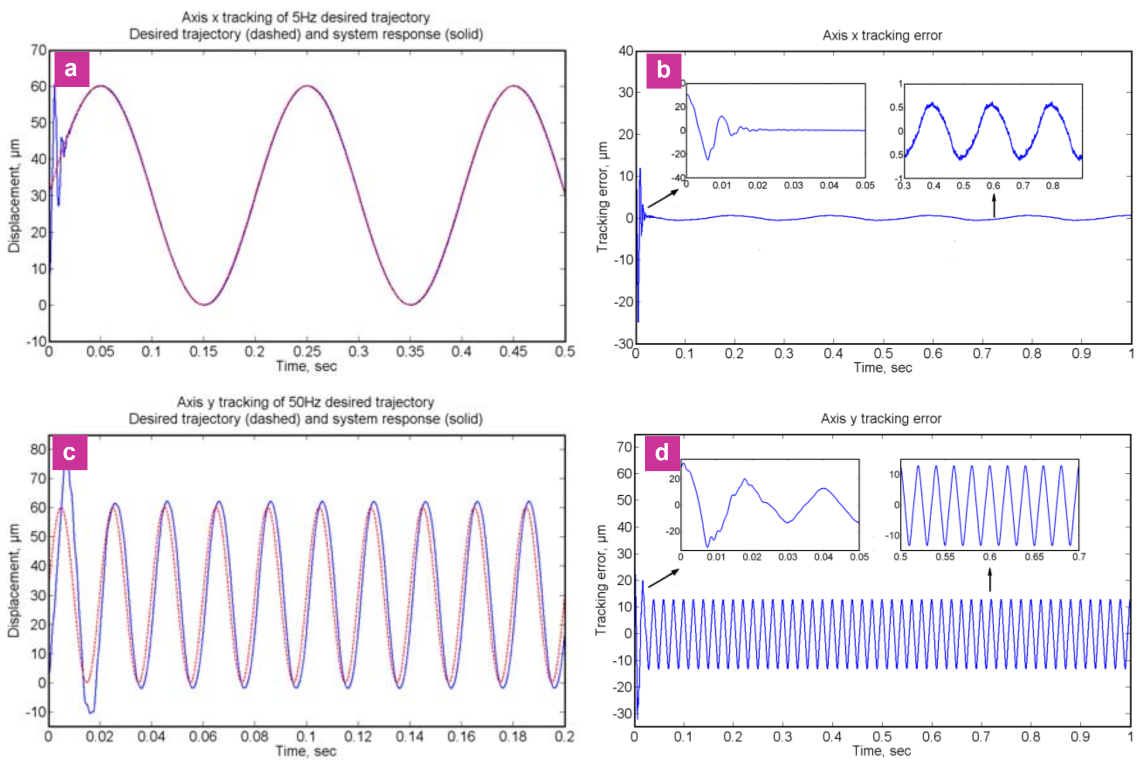

Figure 3.8. PID controller results for simultaneous double-axis motion control; (a) axis x 5 Hz tracking control, (b) axis x tracking error, (c) axis y 50 Hz tracking control, and (d) axis y tracking error.

3.4.4. Robust Adaptive Control Development

Precision tracking control of the double-axis piezo-flexural system presented by Eq. (3.9) encounters problems such as parametric uncertainties, external disturbances, and ever-present unmodeled dynamics including coupling and hysteresis modeling uncertainties. However, a properly designed closed-loop controller can offer a remedy for all these problems. This subsection proposes a Lyapunov-based robust adaptive control strategy for the precision tracking control of piezo-flexural nanopositioning systems.

Since both system axes motions are governed by identical equations of motion, for the sake of simplicity, the controller is designed for only one axis, and without loss of generality, is applied to the second axis as well. For this, let's select axis *x* and remove all the indices in Eq. (3.9). The following definitions are considered first:

$$
\begin{aligned}
&H\{v(t)\} \triangleq a\left(v(t)+\hat{v}_h(t)+\tilde{v}_h(t)\right) \\
&C\{y(t)\} \triangleq b\left(y(t)+\hat{y}_c(t)+\tilde{y}_c(t)\right) \\
&D(t) \triangleq \hat{D}(t)+\tilde{D}(t)
\end{aligned}
\tag{3.10}
$$

where operators $H\{v(t)\}$ and $C\{y(t)\}$ are assumed to be divided into linear segments with the respective slopes of *a* and *b*, known time-varying parts $\hat{v}_h(t)$ and $\hat{y}_c(t)$ (obtained from approximate models), and bounded uncertain parts $\tilde{v}_h(t)$ and $\tilde{y}_c(t)$, respectively. Similarly, the disturbance is divided into a known part $\hat{D}(t)$ and a bounded uncertain part $\tilde{D}(t)$. The validity of this assumption (dividing hysteresis into a linear part and a bounded time-varying part) has been shown in [52] for systems with backlash-like hysteresis including piezoelectric systems. Moreover, it has been shown that hysteresis trajectories in piezo-flexural stages are bounded by reference curves, due to the hysteresis curve-alignment property [20].

The equation of motion can then be written as:

$$\begin{aligned}
&m\ddot{x}(t) + c\dot{x}(t) + kx(t) = v(t) + \hat{v}_h(t) + r\left(y(t) + \hat{y}_c(t)\right) + \hat{D}(t) + p(t),\\
&p(t) = p_0 + \tilde{p}(t) = \tilde{v}_h(t) + r\tilde{y}_c(t) + \tilde{D}(t),\\
&m = \frac{1}{a\omega_n^2},\ \ c = \frac{2\xi}{a\omega_n},\ \ k = \frac{1}{a},\ \ r = \frac{b}{a}
\end{aligned} \tag{3.11}$$

with $p(t)$ being the overall system perturbations consisting of an average (static) term p_0 to be relaxed through an adaption law, and a time-varying term $\tilde{p}(t)$ to be compensated through a robust control design. Parameters m, c, k and r are the system unknown parameters to be included in the adaptive strategy. It is remarked that one is free to take only the linear part of the operators and leave $\hat{v}_h(t)$ and $\hat{y}_c(t)$ completely in the uncertainty terms $\tilde{v}_h(t)$ and $\tilde{y}_c(t)$, respectively. However, the less the amplitude of system perturbation, the better the tracking performance will be in practice.

<u>*Control Derivation*</u>

To simultaneously satisfy tracking control and robustness requirements, the sliding hyperplane is selected as:

$$s(t) = \dot{e}(t) + \sigma e(t) \tag{3.12}$$

where $\sigma > 0$ is a control gain, and $e(t) = x_d(t) - x(t)$ with $x_d(t)$ being the two times continuously differentiable desired trajectory. Taking the time derivative of (3.12) and using (3.11) yields:

$$\begin{aligned}\dot{s}(t) &= \ddot{e}(t) + \sigma\,\dot{e}(t) \\ &= \ddot{x}_d(t) - \ddot{x}(t) + \sigma\,\dot{e}(t) \\ &= \ddot{x}_d(t) + \sigma\,\dot{e}(t) + \frac{1}{m}\Big(c\dot{x}(t) + kx(t) - v(t) - \hat{v}_h(t) - r\big(y(t) + \hat{y}_c(t)\big) - \hat{D}_h(t) - p_0 - \tilde{p}(t)\Big)\end{aligned} \tag{3.13}$$

Theorem 3.1: For the system described by (3.11)*, if the variable structure control is given by:*

$$\begin{aligned}v(t) = {} & \hat{m}(t)\big(\ddot{x}_d(t) + \sigma\dot{e}(t)\big) + \hat{c}(t)\dot{x}(t) + \hat{k}(t)x(t) - \hat{r}(t)\big(y(t) + \hat{y}_c(t)\big) \\ & - \hat{p}_0(t) - \hat{v}_h(t) - \hat{D}_h(t) + \eta_1 s(t) + \eta_2 \operatorname{sgn}\big(s(t)\big)\end{aligned} \tag{3.14}$$

where η_1 *and* η_2 *are positive control gains,* $|\tilde{p}(t)| \le \eta_2$ *for* $\forall t \in [0,\infty)$*, the parameter adaptation laws given by:*

$$\begin{aligned}\hat{m}(t) &= \hat{m}(0) + \frac{1}{k_1}\int_0^t s(\tau)(\ddot{x}_d(\tau) + \sigma\dot{e}(\tau))d\tau \\ \hat{c}(t) &= \hat{c}(0) + \frac{1}{k_2}\int_0^t s(\tau)\dot{x}(\tau)d\tau \\ \hat{k}(t) &= \hat{k}(0) + \frac{1}{k_3}\int_0^t s(\tau)x(\tau)d\tau \\ \hat{r}(t) &= \hat{r}(0) - \frac{1}{k_4}\int_0^t s(\tau)\big(y(\tau) + \hat{y}_c(\tau)\big)d\tau \\ \hat{p}_0(t) &= \hat{p}_0(0) - \frac{1}{k_5}\int_0^t s(\tau)d\tau\end{aligned} \tag{3.15}$$

with k_1 to k_5 *being adaptation gains, and* $\hat{m}(0)$ *to* $\hat{p}(0)$ *being approximate parameter values, then asymptotic stability of the closed-loop system and tracking control of desired trajectory are guaranteed in the sense that* $e(t)$ *is bounded.*

Proof: Let's define the following parametric error signals and take their time derivatives to obtain:

$$
\begin{aligned}
&\tilde{m}(t) = m - \hat{m}(t);\ \dot{\tilde{m}}(t) = -\dot{\hat{m}}(t) \\
&\tilde{c}(t) = c - \hat{c}(t);\ \dot{\tilde{c}}(t) = -\dot{\hat{c}}(t) \\
&\tilde{k}(t) = k - \hat{k}(t);\ \dot{\tilde{k}}(t) = -\dot{\hat{k}}(t) \\
&\tilde{r}(t) = r - \hat{r}(t);\ \dot{\tilde{r}}(t) = -\dot{\hat{r}}(t) \\
&\tilde{p}_0(t) = p_0 - \hat{p}_0(t);\ \dot{\tilde{p}}_0(t) = -\dot{\hat{p}}_0(t)
\end{aligned}
\tag{3.16}
$$

Now, select the positive definite Lyapunov function as:

$$
V_L(t) = \frac{1}{2}\left(ms^2(t) + k_1\tilde{m}^2(t) + k_2\tilde{c}^2(t) + k_3\tilde{k}^2(t) + k_4\tilde{r}^2(t) + k_5\tilde{p}_0^2(t) \right) \tag{3.17}
$$

Taking its time derivative yields:

$$
\dot{V}_L(t) = ms(t)\dot{s}(t) + k_1\tilde{m}(t)\dot{\tilde{m}}(t) + k_2\tilde{c}(t)\dot{\tilde{c}}(t) + k_3\tilde{k}(t)\dot{\tilde{k}}(t) + k_4\tilde{r}(t)\dot{\tilde{r}}(t) + k_5\tilde{p}_0(t)\dot{\tilde{p}}_0(t) \tag{3.18}
$$

Substituting (3.13), (3.14) and (3.16) into (3.18) results in:

$$
\begin{aligned}
\dot{V}_L(t) = {} & \tilde{m}(t)\left[s(t)\left(\ddot{x}_d(t) + \sigma\dot{e}(t) \right) - k_1\dot{\hat{m}}(t) \right] + \tilde{c}(t)\left[s(t)\dot{x}(t) - k_2\dot{\hat{c}}(t) \right] \\
& + \tilde{k}(t)\left[s(t)x(t) - k_3\dot{\hat{k}}(t) \right] - \tilde{r}(t)\left[s(t)\left(y(t) + \hat{y}_c(t) \right) + k_4\dot{\hat{r}}(t) \right] \\
& - \tilde{p}_0(t)\left[s(t) + k_5\dot{\hat{p}}(t) \right] - \eta_1 s(t)^2 - \eta_2 s(t)\operatorname{sgn}\left(s(t) \right) + \tilde{p}(t)s(t)
\end{aligned}
\tag{3.19}
$$

Taking time derivatives of adaptation laws given by (3.15) and substituting into (3.19) makes the coefficients of the parametric error signals (terms inside the squared brackets) zero. Hence:

$$\dot{V}_L(t) = -\eta_1 s^2(t) - \eta_2 s(t)\mathrm{sgn}\left(s(t)\right) + \tilde{p}(t)s(t) = -\eta_1 s^2(t) - \eta_2 \left|s(t)\right| + \tilde{p}(t)s(t) \qquad (3.20)$$

If the condition $\left|\tilde{p}(t)\right| \le \eta_2$ is applied for all $t > 0$ then:

$$-\eta_2 \left|s(t)\right| \le \tilde{p}(t)s(t) \ \text{ or } \ \dot{V}_L(t) \le -\eta_1 s^2(t) \le 0 \qquad (3.21)$$

Since the time derivative of proposed Lyapunov function is negative, asymptotic convergence of the sliding variable $s(t)$ is achieved, i.e. $s(t) \to 0$ as $t \to \infty$ according to [53]. Moreover, all the adaptation signals are bounded; hence $e(t)$ and $\dot{e}(t)$ converge to zero, as a conclusion from (3.12).

Derivation and Analysis of Soft Switching Mode Control

Although the proposed adaptive sliding mode controller is robust and asymptotically stable, it cannot be effectively implemented in practice due to the chatter phenomenon [49]. That is, due to the hard switching of signum function in the control law, resonant modes of the system can be excited which may lead to large vibrations or even instability. A widely-used remedy for this problem is to replace the hard switching term $sgn(s)$ with a softer switching method using the following saturation function:

$$\mathrm{sat}(s/\varepsilon) = \begin{cases} s/\varepsilon & \left|s\right| \le \varepsilon \\ \mathrm{sgn}(s) & \left|s\right| > \varepsilon \end{cases} \qquad (3.22)$$

with ε being a small positive parameter select to adjust the rate of switching operation. The control law (3.14) is then modified to:

$$\begin{aligned} v(t) &= \hat{m}(t)\left(\ddot{x}_d(t)+\sigma\dot{e}(t)\right)+\hat{c}(t)\dot{x}(t)+\hat{k}(t)x(t)-\hat{r}(t)\left(y(t)+\hat{y}_c(t)\right) \\ &\quad -\hat{p}_0(t)-\hat{v}_h(t)-\hat{D}_h(t)+\eta_1 s(t)+\eta_2 \mathrm{sat}\left(s(t)/\varepsilon\right) \end{aligned} \tag{3.23}$$

It is remarked that the adaptation laws given by (3.15) are no longer applicable with the modified control law. The reason is that control law (3.23) can only guarantee the boundedness of the sliding trajectory, not its asymptotic convergence, i.e. $s(t)\rightarrow\Omega$ as $t\rightarrow\infty$, where Ω is a bounded set. Hence, adaptation integrals in (3.15) can lead to unbounded values over time. To eliminate this problem, a projection operator is utilized as proposed in [50]. This operator requires the lower and the upper bounds of parameters and is introduced as:

$$\mathrm{Proj}_\theta\left[\bullet\right]=\begin{cases} 0 & \text{if } \hat{\theta}(t)=\theta_{\max} \text{ and } \bullet>0 \\ 0 & \text{if } \hat{\theta}(t)=\theta_{\min} \text{ and } \bullet<0 \\ \bullet & \text{otherwise} \end{cases} \tag{3.24}$$

where $\hat{\theta}(t)$ represents the adaptation parameter (e.g., $\hat{m}(t)$, $\hat{c}(t)$, etc.) with $\theta_{\min}$ and $\theta_{\max}$ being its lower and upper bounds, respectively. Accordingly, the adaptation laws are modified to:

$$\hat{m}(t)=\hat{m}(0)+\frac{1}{k_1}\int_0^t \mathrm{Proj}_m\left[s(\tau)\left(\ddot{x}_d(\tau)+\sigma\dot{e}(\tau)\right)\right]d\tau$$
$$\hat{c}(t)=\hat{c}(0)+\frac{1}{k_2}\int_0^t \mathrm{Proj}_c\left[s(\tau)\dot{x}(\tau)\right]d\tau$$
$$\hat{k}(t)=\hat{k}(0)+\frac{1}{k_3}\int_0^t \mathrm{Proj}_k\left[s(\tau)x(\tau)\right]d\tau \tag{3.25}$$
$$\hat{r}(t)=\hat{r}(0)+\frac{1}{k_4}\int_0^t \mathrm{Proj}_r\left[-s(\tau)\left(y(\tau)+\hat{y}_c(\tau)\right)\right]d\tau$$
$$\hat{p}_0(t)=\hat{p}_0(0)+\frac{1}{k_5}\int_0^t \mathrm{Proj}_{p_0}\left[-s(\tau)\right]d\tau$$

Hence, it is guaranteed that the adaptation parameters remain bounded by the lower and upper bounds, provided that they are initially selected within the bounds, i.e. if $\theta_{\min}<\hat{\theta}(0)<\theta_{\max}$, then $\theta_{\min}<\hat{\theta}(t)<\theta_{\max}$, $\forall t\in[0,\infty)$. Furthermore, it can be shown that the following property holds for the projection operator:

$$\tilde{\theta}(t)\chi(t)\leq\tilde{\theta}(t)\mathrm{Proj}_{\theta}\left[\chi(t)\right] \tag{3.26}$$

Theorem 3.2: For the system described by (3.11)*, if the soft variable structure control given by* (3.23) *and the adaptation laws given by* (3.25) *are applied, the closed-loop system becomes globally uniformly ultimately bounded, in the sense that the error* $e(t)$ *is bounded. Moreover, the bound of the steady-state error can be explicitly derived as:*

$$\left|e_{ss}(t)\right|\leq\frac{\eta_2\varepsilon}{\sigma(\eta_1\varepsilon+\eta_2)} \tag{3.27}$$

Proof: The time derivative of the Lyapunov function given in (3.17), after applying modified control law (3.23), adaptation laws (3.25), and property (3.26) becomes:

$$\dot{V}_L(t) \le -\eta_1 s(t)^2 - \eta_2 s(t)\mathrm{sat}\left(s(t)/\varepsilon\right) + \tilde{p}(t)s(t) \tag{3.28}$$

Assume that the sliding variable starts from outside the boundary layer specified by ε, such that its initial value satisfies $|s(0)| > \varepsilon$. From (3.22), the Lyapunov derivative of the modified controller, Eq. (3.28) becomes identical to that of the primary controller, Eq. (3.20). Hence, $s(t)$ will be stirred towards zero as a conclusion from Theorem 3.1. However, before arriving at the origin, it enters the boundary layer, $|s(t)| \le \varepsilon$, where the structure of controller changes due to the switching of saturation function. For $s(t)$ being inside the boundary layer, the derivative of the Lyapunov function is given by:

$$\begin{aligned} \dot{V}_L(t) &\le -\eta_1 s^2(t) - \eta_2 s(t)\mathrm{sat}\left(s(t)/\varepsilon\right) + \tilde{p}(t)s(t) = \\ &-\eta_1 s^2(t) - \eta_2 s^2(t)/\varepsilon + \tilde{p}(t)s(t) = \\ &s(t)\left(\tilde{p}(t) - \left[\eta_1 + \eta_2/\varepsilon\right]s(t)\right), \;\; |s(t)| \le \varepsilon \end{aligned} \tag{3.29}$$

If $s(t)$ stays inside a particular range in the boundary layer such that it satisfies $\left(|\tilde{p}(t)|\varepsilon\right)/\left(\eta_1\varepsilon + \eta_2\right) \le |s(t)| \le \varepsilon$, then it follows that $\dot{V}_L(t) \le 0$. Hence, $s(t)$ is further forced towards the origin. Once it enters the region where the inequality $|s(t)| < \left(|\tilde{p}(t)|\varepsilon\right)/\left(\eta_1\varepsilon + \eta_2\right) < \varepsilon$ holds, the derivative of the Lyapunov function becomes positive, i.e., $\dot{V}_L(t) > 0$. This may force $s(t)$ to move outside the region, where it will be forced back inside again. Eventually, $s(t)$ will be entrapped inside the region where $|s(t)| < \left(|\tilde{p}(t)|\varepsilon\right)/\left(\eta_1\varepsilon + \eta_2\right) \le \lambda < \varepsilon$, and $\lambda = \eta_2\varepsilon/\left(\eta_1\varepsilon + \eta_2\right)$ after a finite time $\tau_\lambda \; \forall t \in [\tau_\lambda, \infty)$. Hence, the region $|s(t)| < \lambda < \varepsilon$ is the zone of convergence or the region of attraction for trajectories starting outside the zone.

Now, assume that $s(t)$ enters the zone of convergence at $t=\tau_\lambda$ and the inequality $|s(t)|<\lambda$ holds for $\forall t\in[\tau_\lambda,\infty)$. Consequently, a time-varying positive function $l_1(t)>0$ can be found such that:

$$s(t)=\dot{e}(t)+\sigma e(t)=\lambda-l_1(t) \tag{3.30}$$

Solving the differential equation (3.30) yields:

$$\begin{aligned} e(t) &= \frac{\lambda}{\sigma}+\left\{e(\tau_\lambda)-\frac{\lambda}{\sigma}\right\}\exp\left(-\sigma(t-\tau_\lambda)\right)-\exp\left(-\sigma t\right)\int_{\tau_\lambda}^{t} l_1(\tau)\exp\left(\sigma\tau\right)d\tau \\ &< \frac{\lambda}{\sigma}+\left\{e(\tau_\lambda)-\frac{\lambda}{\sigma}\right\}\exp\left(-\sigma(t-\tau_\lambda)\right) \quad \forall t\in[\tau_\lambda,\infty) \end{aligned} \tag{3.31}$$

Therefore,

$$e_{ss}(t)<\frac{\lambda}{\sigma} \tag{3.32}$$

Likewise, there exists a function $l_2(t)>0$, $\forall t\in[\tau_\lambda,\infty)$, for $|s(t)|<\lambda$ such that:

$$s(t)=\dot{e}(t)+\sigma e(t)=-\lambda+l_2(t) \tag{3.33}$$

which similarly follows that:

$$e(t)>-\frac{\lambda}{\sigma}+\left\{e(\tau_\lambda)+\frac{\lambda}{\sigma}\right\}\exp\left(-\sigma(t-\tau_\lambda)\right); \quad \forall t\in[\tau_\lambda,\infty) \tag{3.34}$$

And consequently,

$$e_{ss}(t)>-\frac{\lambda}{\sigma} \tag{3.35}$$

Form inequalities (3.32) and (3.35), one can simply conclude:

$$\left|e_{ss}(t)\right| \leq \beta \quad \text{where} \quad \beta = \frac{\lambda}{\sigma} = \frac{\eta_2 \varepsilon}{\sigma(\eta_1 \varepsilon + \eta_2)} \tag{3.36}$$

The intersection of regions $\left|s(t)\right| < \lambda$ and $\left|e(t)\right| < \beta$ forms a parallelogram in $e - \dot{e}$ plane to which the error phase trajectory converges. Figure 3.9 graphically demonstrates the function of the proposed soft variable structure controller. The $e - \dot{e}$ plane is divided into four regions: region 1, where $\left|s(t)\right| > \varepsilon$; region 2, the boundary layer where $\left|s(t)\right| < \varepsilon$; region 3, the convergence zone of $s(t)$ where $\left|s(t)\right| < \lambda$; and region 4, the convergence zone of $e(t)$ where $\left|e(t)\right| < \beta$. Starting from an initial point in region 1, the phase trajectory moves towards region 2, enters the region and proceeds further inside into region 3. It is, however, possible that the trajectory inside region 3 escapes outside due to its initial momentum. In this case, the trajectory will be attracted back to region 3, since the Lyapunov function derivative is always negative outside this region. The trajectory will eventually enter region 4 and get entrapped inside the parallelogram of attraction, as depicted in the figure, representing a globally uniformly ultimately bounded response for the closed-loop system.

The appropriate selection of control parameters requires a number of trial and error experiments. With the help of explicit derivation of the system ultimate error bound given by (3.36), the selected sets of control parameters can be initially checked for performance acceptability. This leads to saving a large number of experimental runs. The initially verified sets can then be implemented in the actual experiment for selecting the final set.

It is remarked that if the constraints on the error bounds are too tight, the probability of chattering increases. Final set of control parameters is selected based on a trade-off and step-by-step squeezing of the ultimate error bound, while staying away from chatter. Eq. (3.36) can also be helpful on performing such a trade-off, since it can present the sensitivity of the ultimate error with respect to the control parameters.

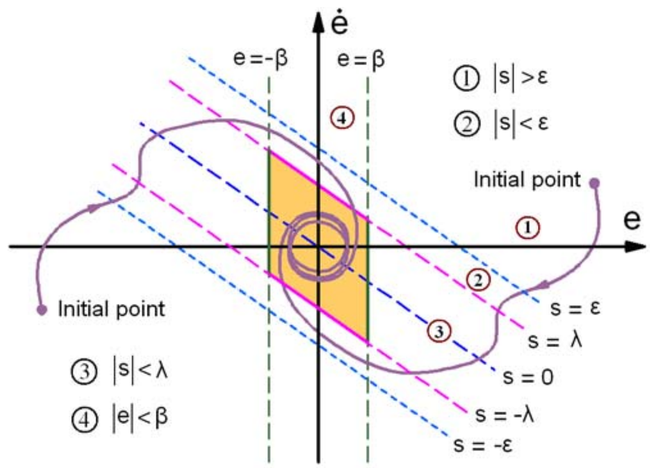

Figure 3.9. Soft variable structure control with parallelogram zone of attraction.

Experimental Verification of the Robust Adaptive Controller

In this subsection, the proposed controller is experimentally implemented for tracking of the same sinusoidal trajectories used in the PID controller earlier. Only the linear parts of the hysteresis and the coupling nonlinearities are taken into account, and no external disturbances affect the system, i.e. $\hat{v}_h(t) = \hat{y}_c(t) = 0$ and $D(t) = 0$. The approximate values of the system parameters used for initialization of the adaptation integrals are given in Table 3.3. The selected control gains obtained from an experimental trial and error procedure are listed in Table 3.4.

Table 3.3. Approximate system parameter values.

System parameters	ω_n	ζ	a	b	m	c	k	r
Approximate values	2700	3	10^{-6}	0.0025	0.14	2200	10^{6}	2500
Units	rad/sec	-	m/Volt	-	kg.V/N	V.s/m	V/m	V/m

Table 3.4. Control parameter values for the experiments.

Control parameters	σ	ε	η_1	η_2	-
Values	500	0.01	300	20	-
Adaptation gains	k_1	k_2	k_3	k_4	k_5
Values	20	2×10^{-9}	5×10^{-14}	10^{-10}	2×10^{-6}

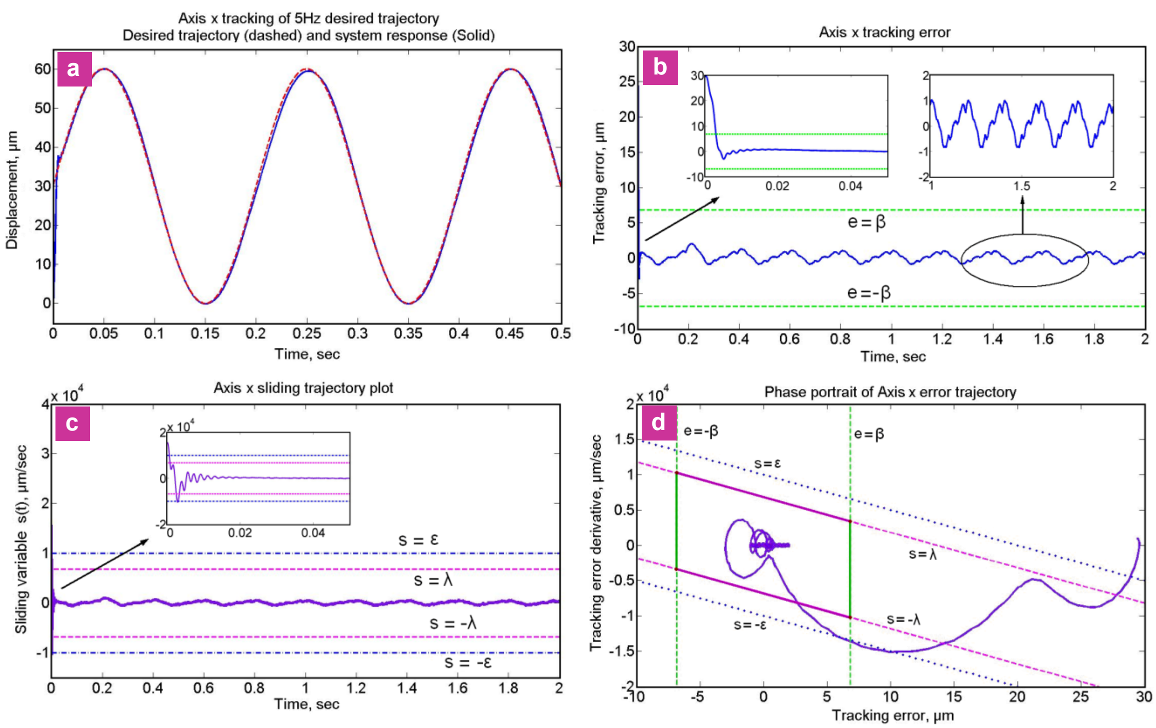

Figure 3.10. Axis x tracking control results: (a) trajectory tracking, (b) tracking error, (c) sliding variable plot, and (d) phase portrait of error trajectory.

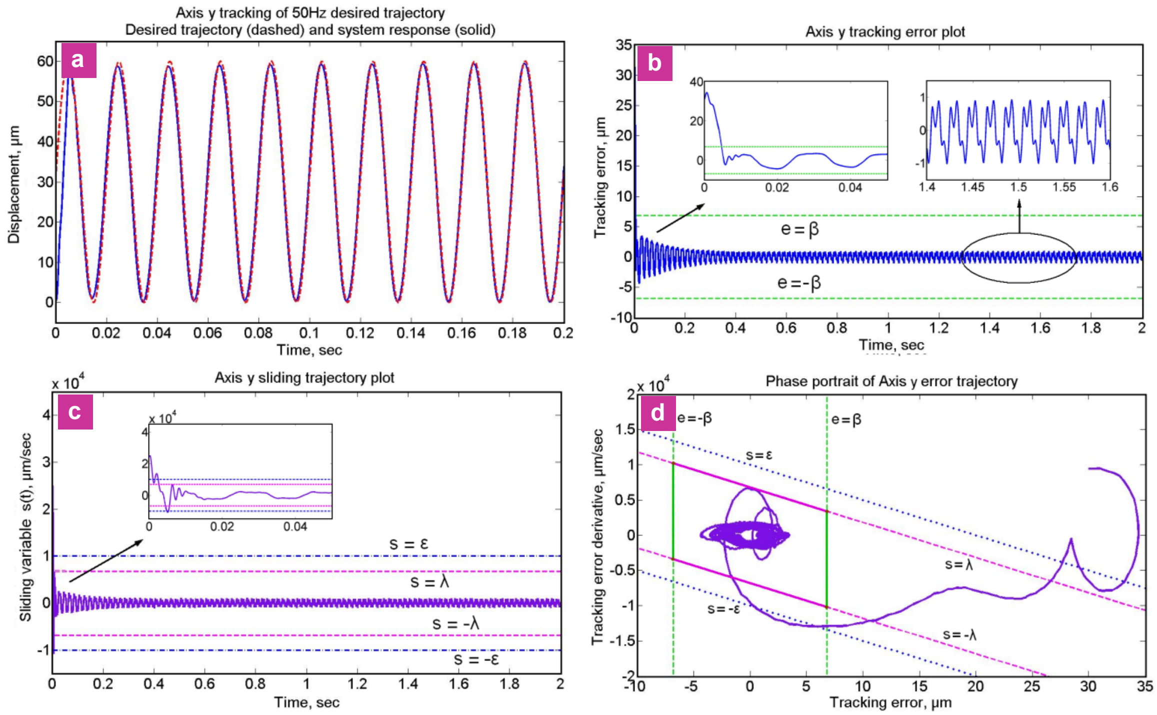

Figure 3.11. Axis *y* tracking control results: (a) trajectory tracking, (b) tracking error, (c) sliding variable plot, and (d) phase portrait of error trajectory.

Figures 3.10 and 3.11 depict the double-axis tracking control results for axis *x*, and axis *y*, respectively. Tracking of the desired trajectory, system error response, convergence of the sliding variable, $s(t)$, and the error phase portrait are given through sub-plots 3.10(a)-(d) for axis *x* , and sub-plots 3.11(a)-(d) for axis *y*. It is seen that the convergence of the error and the sliding trajectories to the prescribed zones are attained. Furthermore, the error phase trajectories converge to the predicted parallelogram formed by the control gains. The adaptations of parameters $\hat{k}(t)$ and $\hat{p}_0(t)$ are depicted in Figure 3.12. For the other parameters, adaptation signals stay within their lower and upper bounds, similarly. However, the plots are omitted in the interest of space saving. It is remarked that the coefficients of the parameter adaptations are obtained experimentally to yield a sufficiently high adaptation rate while stay away from instability.

Maximum and average steady-state tracking error percentages are obtained as 1.67 % and 0.83 % for axis x, and 1.71 % and 0.82 % for axis y, respectively. It is seen that the controller yields similar tracking performance for both axis in different frequencies. However, it is remarked that some portion of performance drop is due to the simultaneous double-axis operation; experiments demonstrate that single axis tracking yields considerable improvement in performance (around 180 % compared to the double-axis tracking) with the proposed control method.

Comparing to the PID controller, transient response in low-frequency tracking and the steady-state performance in high frequency tracking have been significantly improved. Therefore, the proposed controller is preferred over the PID controller, especially at high frequencies. However, if low-frequency tracking with zero initial value is desired or the transient properties are not the concern, PID controller is preferred due to its simple structure and straightforward implementation.

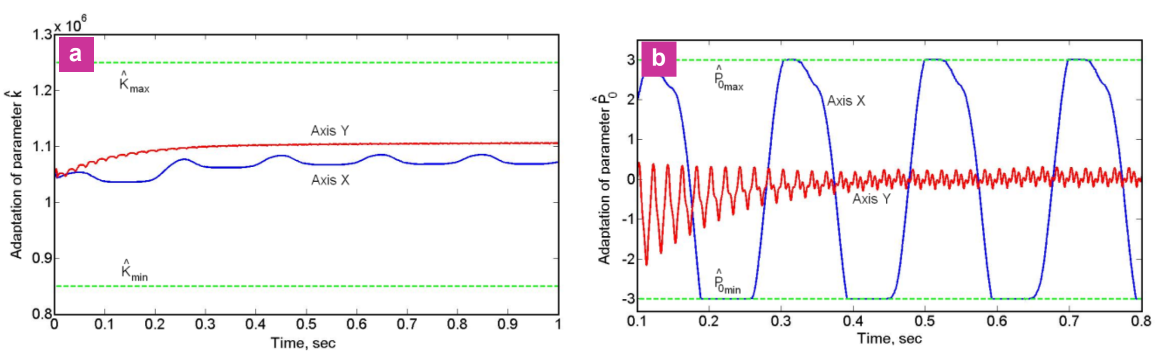

Figure 3.12. Parameters adaptation results: adaptation of (a) $\hat{k}(t)$, and (b) $\hat{p}_0(t)$.

3.4.5. Application in High-Speed Laser-Free AFM

The proposed robust adaptive controller implemented in *xy* scanning system is utilized here for micro- and nano-scale imaging using a laser-free AFM setup shown in Figure 3.13. As seen from the figure, the sample to be imaged is mounted on the *xy* scanning stage, while a piezoresistive microcantilever is mounted on the *z* nanopositioning stage for acquiring sample topography. The *z*-stage is used only for the initial adjustment and to bring the cantilever into a desired contact with the sample. During the scanning process, the *z*-stage does not move; hence, the cantilever deflection corresponds to the surface topography (see Figure 3.14 for the schematic view of laser-free AFM setup).

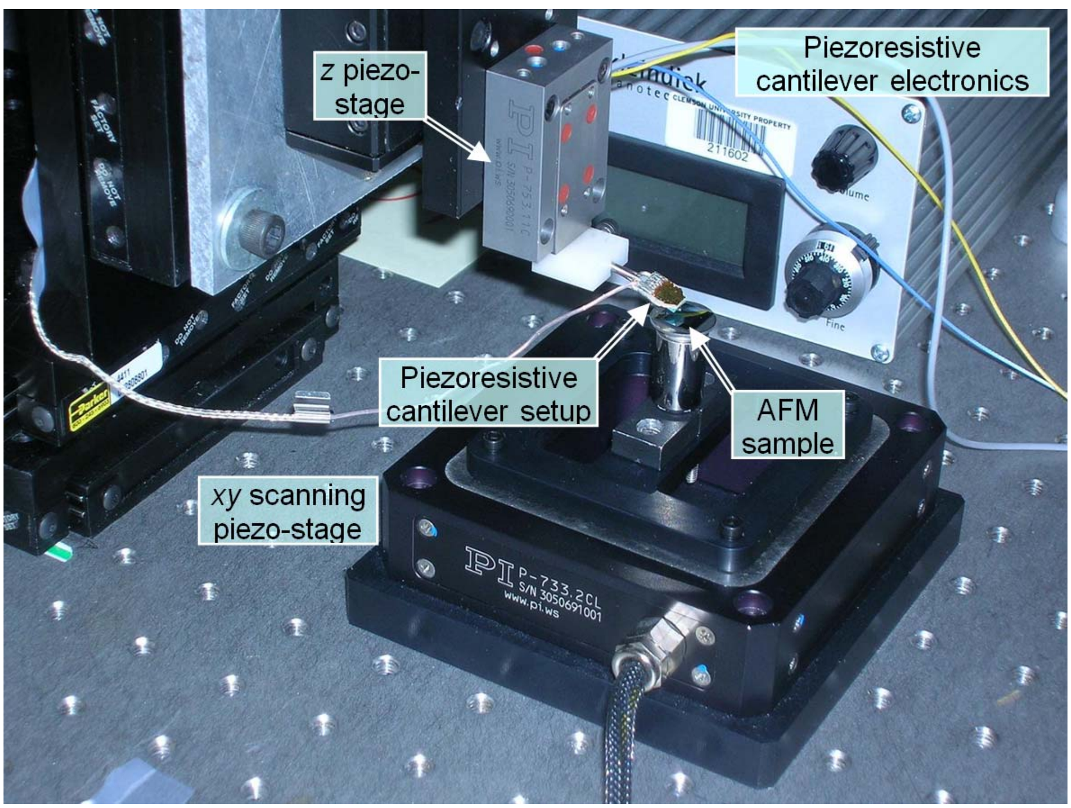

Figure 3.13. Piezoresistive cantilever-based laser-free AFM setup.

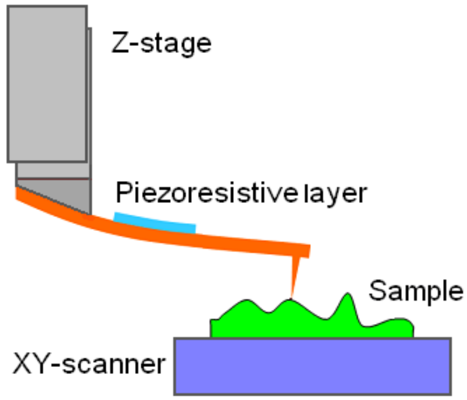

Figure 3.14. Schematic representation of laser-free AFM setup.

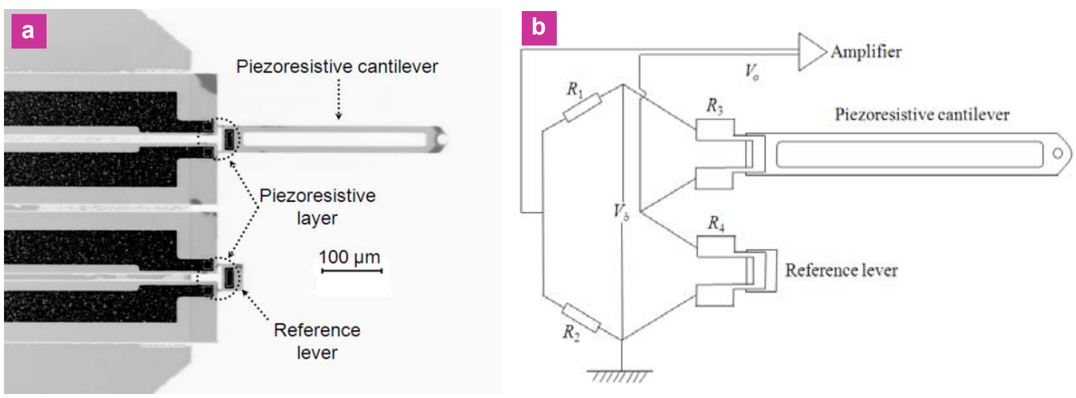

Figure 3.15. Piezoresistive microcantilever with Weston bridge circuit.

A self-sensing microcantilever, PRC-400, is utilized here for imaging purpose. Figure 3.15(a) depicts the piezoresistive cantilever image under a 100X magnification light microscopy consisting of a piezoresistive layer on the base, tip mass and the piezoresistive reference lever. The piezoresistive layers on cantilever and reference lever are utilized as the resistances in a Wheatstone bridge. Due to the external force on the piezoresistive cantilever's tip, it bends and results in a change of resistance in the piezoresistive layer. This change of resistance can be monitored utilizing the output voltage of the Wheatstone bridge. Figure 3.15(b) depicts a schematic of the PRC-400 self-sensing cantilever, with external Wheatstone bridge and amplifier [54]. Since the first resonant frequency of cantilever is around several kHz, in low-frequency operations (e.g. below 100 Hz), the cantilever behaves similar to a lumped-parameters system. Hence, the relation between the cantilever deflection and output voltage of the Wheatstone bridge is realized to be linear (proportional) [54]. Thus, the cantilever deflection can be measured by knowing the deflection-to-voltage gain of the piezoresistive cantilever.

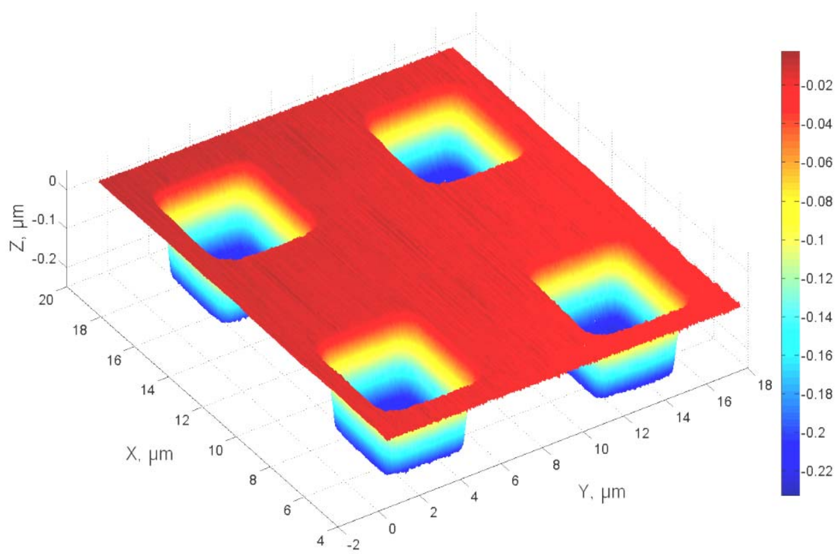

Figure 3.16. 3D image of an AFM calibration sample with 200 *nm* steps captured by the developed laser-free AFM setup at 10 Hz raster scanning rate.

Figure 3.16 demonstrates the 3D image of an AFM calibration sample using the developed laser-free AFM setup. Trajectories for axes x and y are assigned based on a raster scanning procedure; that is, one of the axes tracks a low-rate ramp trajectory, while the other is in charge of tracking a high-rate sinusoidal trajectory. For tracking the low-rate ramp trajectory, PID controller is used, while the proposed robust adaptive controller has been utilized for tracking the harmonic trajectory. It is particularly desired to relate the quality of the acquired image to the speed of scanning which is proportional to the frequency of harmonic trajectory. Figure 3.17 demonstrates the top view of images at frequencies varying from 10 Hz to 60 Hz with 10 Hz increments. It is seen that as the frequency increases, more blurred images are obtained. This quality drop could have been originated from the increased vibrations of microcantilever due to facing with the steeper steps in the surface at higher speeds, and/or the sensitivity reduction of piezoresistive layer due to the frequency increase. Nevertheless, acquiring high-quality images at frequencies up to 30 Hz could imply to the effectiveness of the proposed control framework in increasing the speeds of current AFMs which typically suffer from the low speed of their PID controllers.

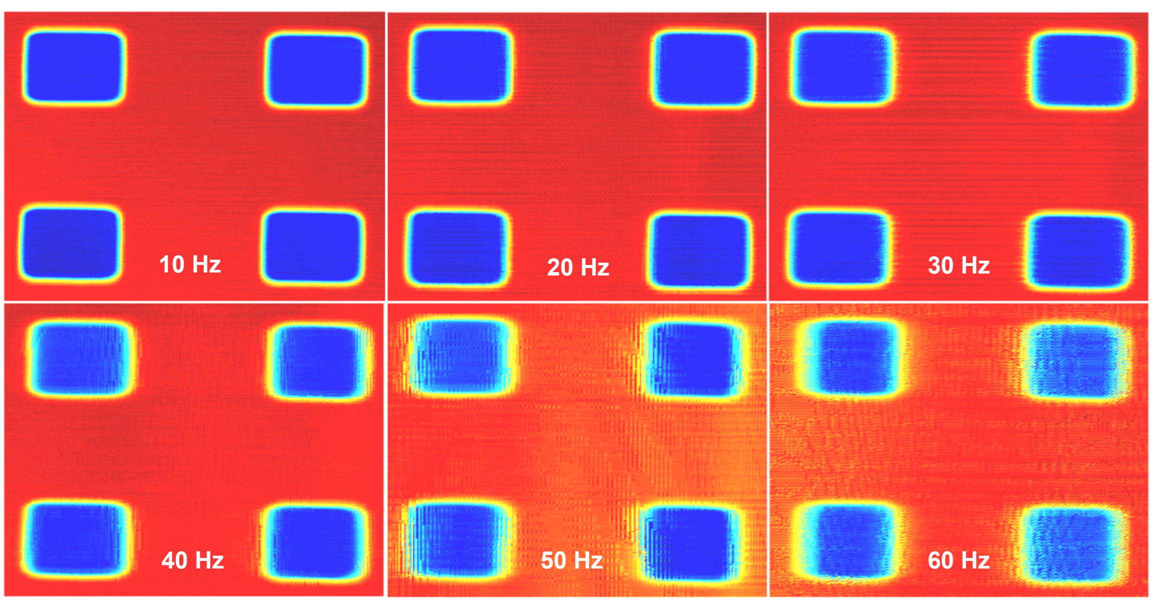

Figure 3.17. Effects of raster scanning frequency on the image quality of laser-free AFM.

Chapter Summary

High frequency tracking control of piezoactive micro and nanopositioning systems is not only influenced by hysteresis nonlinearity, but also by the excitation of system dynamics. Integration of a second order dynamic model, equivalent of a mass-spring-damper trio, with a hysteresis operator appearing in the input excitation was shown to accurately model the behavior of such systems in a reasonably broad frequency range. A feedforward control law, simultaneously accounting for the system dynamics and hysteretic effect, was proposed and validated on a piezoactive nanopositioning stage in tracking of multiple-frequency harmonic trajectories including both low and high frequency components. However, to increase the positioning accuracy despite the parametric uncertainties, and eliminate the complexities associated with hysteresis modeling, a Lyapunov-based robust adaptive control strategy was proposed. The controller demonstrated excellent tracking of low and high-frequency trajectories despite the parametric uncertainties and unmodeled hysteresis nonlinearity. Comparisons with widely-used PID controller demonstrate further effectiveness of the proposed robust adaptive controller, particularly at high-frequency operations. Moreover, implementation of the controller in a laser-free AFM setup yields high quality image of surfaces with stepped topographies at frequencies up to 30 Hz in raster scanning. This shall indicate the direct application of the proposed control algorithm in improving the speed of current AFM systems which mostly suffer from the tardiness of their PID controllers.

CHAPTER FOUR

TRACKING CONTROL OF DISCONTINUOUS TRAJECTORIES WITH APPLICATION TO PROBE-BASED IMAGING AND NANOPOSITIONING*

4.1. Introduction

In a typical Scanning Probe Microscopy (SPM) system, the task of the probe attached to a positioning stage is to scan and track the surface of samples with random topography variations, preferably at high speeds. Therefore, precision and robustness are key factors for achieving high-performance control through piezoelectric systems. In general, controllers designed for tracking of time-varying trajectories are tuned for continuously differentiable trajectories. Hence, discontinuities and particularly step-like jumps in the desired trajectory may lead to significant oscillations of the closed-loop system and even instability because of the input saturation. In many applications including SPMs, the desired trajectory is not stipulated, and may change suddenly in real-time. Hence, the controller must be prepared for such events. One of the most commonly used remedies is to pass the desired trajectory through a low-pass filter before applying to the controller. This will transform the jumps of desired trajectory into gradual transitions leading to a smoother signal. However, a delay is inherently induced in the filtered signal which can significantly decrease the control performance in real-time, particularly, at high frequencies.

* The contents of this chapter may have come directly or indirectly from our joint publication [55].

In this chapter, a switching controller is proposed for effective tracking control of high-frequency trajectories with discontinuities. The controller structure is based on switching between two separate control modes: a Lyapunov-based robust adaptive tracking controller (proposed in Chapter 3) and a PID step controller. It has been demonstrated that the proposed robust adaptive controller presents excellent robustness and performance in tracking of continuous trajectories in frequencies up to 300 Hz. However, its transient performance for stepped inputs is limited by large oscillations. On the other hand, a PID controller can be tuned in such a way that it presents excellent step tracking performance with small settling time and overshoot. Nevertheless, the PID controller is unable to precisely track medium-range and high-frequency trajectories because of its limited bandwidth. The proposed switching controller has been shown to offer excellent performance in tracking of high-frequency trajectories with discontinuities without the degrading delay effect associated with filtering proposition. It is expected that this strategy will significantly improve the speed of nanopositioning systems as well as SPMs in imaging applications.

4.2. Problem Statement

SPM is a powerful tool for atomic level surface imaging and manipulation. The main idea in SPM is to bring an atomically sharpened probe close to surface of a sample material and scan it to characterize its topography, or manipulate objects in atomic level. The first SPM was a Scanning Tunneling Microscope (STM) introduced by Binnig and Rohrer in 1981 [56]. Figure 4.1 depicts the schematic view of STM and its working principle.

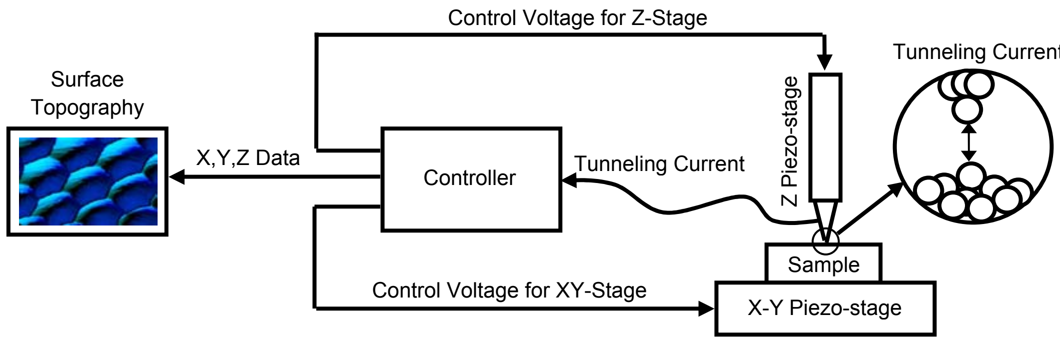

Figure 4.1. Schematic of STM and its working principle.

As illustrated in Figure 4.1, STM utilizes a sharp tip mounted on a piezoelectric stage to approach sample's surface and stop near it in an equilibrium position between the attractive and repulsive areas [57]. In this position, electrons tunnel between the STM tip and the sample resulting in a current with amplitude being a function of the tip/sample distance. Utilizing a piezoelectric scanner, sample is moved in the X-Y directions, and due to the variation of sample topography, the distance between STM tip and sample surface changes. By acquiring the amplified feedback of the tunneling current and employing an appropriate controller, the piezoelectric stage moves up and down in Z direction to control the tunneling current at a constant level [58]. Hence, the recorded positions of X-Y-Z piezoelectric stages can reveal the surface topography with molecular and atomic variations. Other SPMs such as AFM follow similar principles but with different interaction mechanisms between sample and surface.

A typical SPM controller should be able to track different sample topographies, some of which are depicted in Figure 4.2. To this end, SPM tip must scan the surface with the Z stage following the surface's point-by-point topography. As seen from Figure 4.2, the surface topographies may change suddenly (a), smoothly (b), or both (c). For the piezoelectric actuator, tracking the trajectory of a line of scan in Figure 4.2(a), 4.2(b) and 4.2(c) is similar to the tracking the trajectories depicted in Figure 4.3(a), 4.3(b) and 4.3(c), respectively.

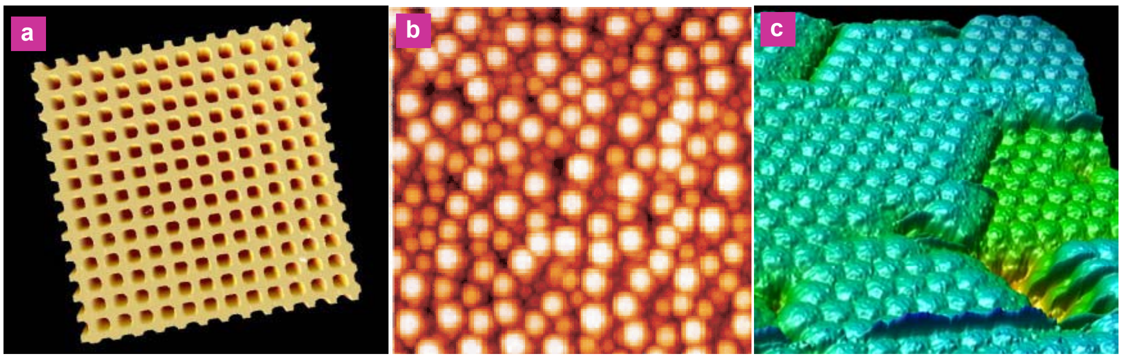

Figure 4.2. Common SPM sample topographies: (a) SPM calibration sample [59], (b) Positively-charged polymer latex particles adsorbed to mica in water [60], and (c) Crystal of satellite tobacco mosaic virus particles [61].

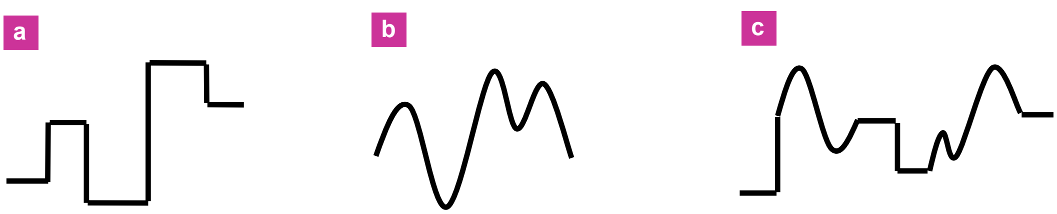

Figure 4.3. (a) Stepped trajectory, (b) continuous harmonic trajectory, and (c) combination of step and harmonic trajectories resembling topographical surfaces of samples shown in Figure 4.2.

As shown in Figures 4.2 and 4.3, SPM samples could contain both rough and smooth topography variations which can be represented with stepped and harmonic trajectories for the control structure. Hence, the control problem for SPM with fast imaging rate can be reduced to robust controller design for piezoelectric actuators that can track combined stepped and sinusoidal trajectories in broad frequency ranges.

As illustrated next, the controller design for tracking of step trajectories in piezoelectric actuators is dissimilar to the design for tracking of sinusoidal trajectories. In this work, two different control structures are utilized along with an optimal switching function that efficiently switches between them to provide concurrent performance in tracking stepped and harmonic trajectories.

4.3. PID Controller Versus Robust Adaptive Controller

The developed Lyapunov-based robust adaptive controller in Chapter 3 is utilized for the piezoactive nanopositioning system depicted in Figure 2.4 for tracking a desired chirp trajectory. The trajectory is a 1 μm amplitude chirp signal with a linear frequency increase from 0 to 300 Hz within 30 seconds. The advantage of chirp trajectory is that it demonstrates a continuous variation of closed-loop system performance in a wide frequency range. To comparatively assess the effectiveness of the proposed control law, a PID controller is implemented as well. With several trial and errors, the gains of both controllers are tuned in such a way that they operate near their best performance for the applied desired trajectory.

Figure 4.4 depicts the chirp tracking results, as well as a sample tracking around 250 Hz. It is seen that the proposed robust adaptive controller maintains a good level of performance for the entire frequency range, especially for higher frequencies. There is a

2.5% peak for maximum tracking error at about 25 Hz, while for most of the frequencies this value stays below 2%. The PID controller produces a linear increase in error amplitude with respect to frequency. Although it presents better performance compared to the robust adaptive controller initially, its performance starts to degrade after about 30 Hz. Tracking with PID controller can lead to 20% maximum error percentage at 300 Hz, indicating it is less effective than robust adaptive controller in tracking of high-frequency trajectories.

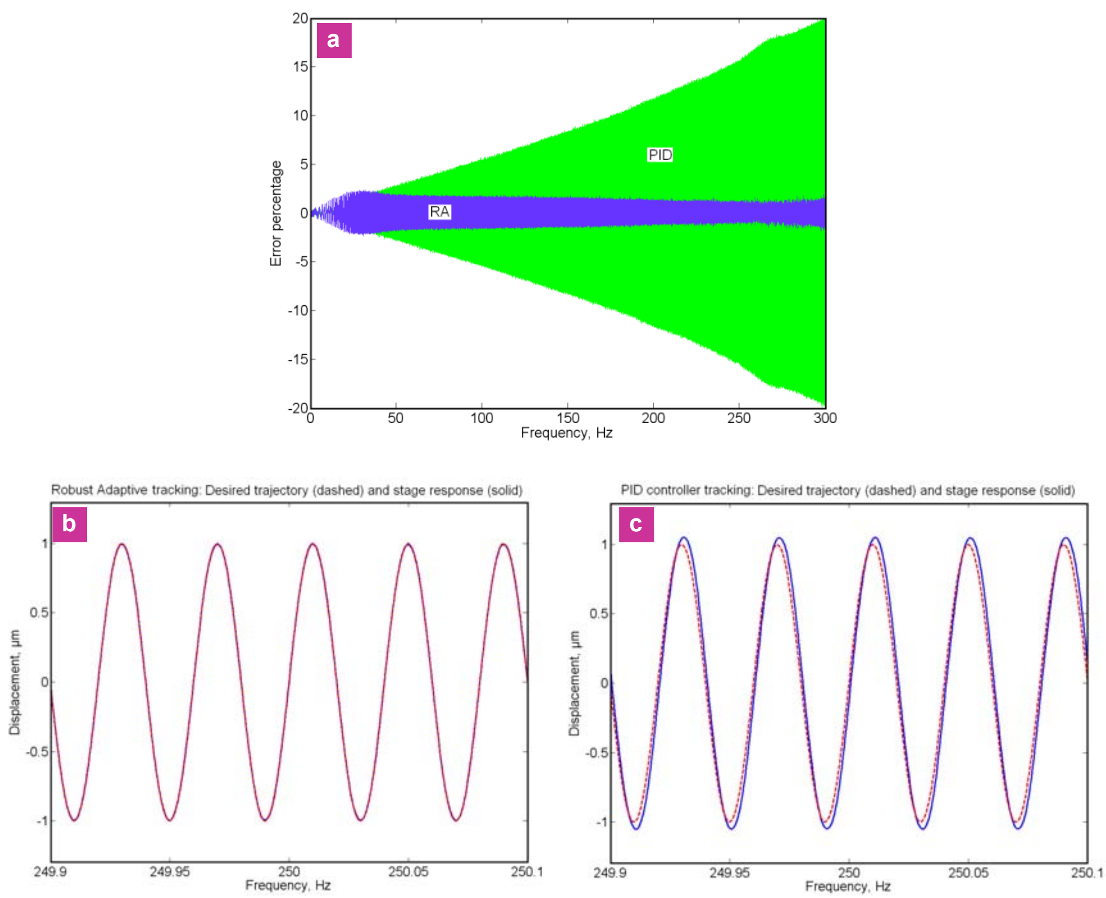

Figure 4.4. Tracking results of 1 μm amplitude chirp trajectory from 0 to 300 Hz: (a) error comparison between well-tuned robust adaptive and PID controllers, (b) robust adaptive tracking around 250 Hz, and (c) PID tracking around 250 Hz.

Since many applications may require tracking of step-like trajectories, a 50 Hz rectangular reference signal is applied to assess the performance of these controllers. Figure 4.5 depicts the system response using PID and robust adaptive controllers. Although both controllers offer stable convergence to the desired trajectory, their transient response includes undesirable large oscillations. Hence, the control gains are re-tuned to present better and faster transient response for stepped trajectory as shown in Figure 4.6. However, when these gains are utilized for tracking of the previous chirp trajectory, they yield lower tracking performance. This is shown in Figure 4.7, where the robust adaptive controller presents about 7% maximum error around 40 Hz while the PID controller yields about 75% error at 300 Hz. Tables 4.1 and 4.2 list the control gains tuned for stepped and chirp trajectories for robust adaptive and PID controllers, respectively.

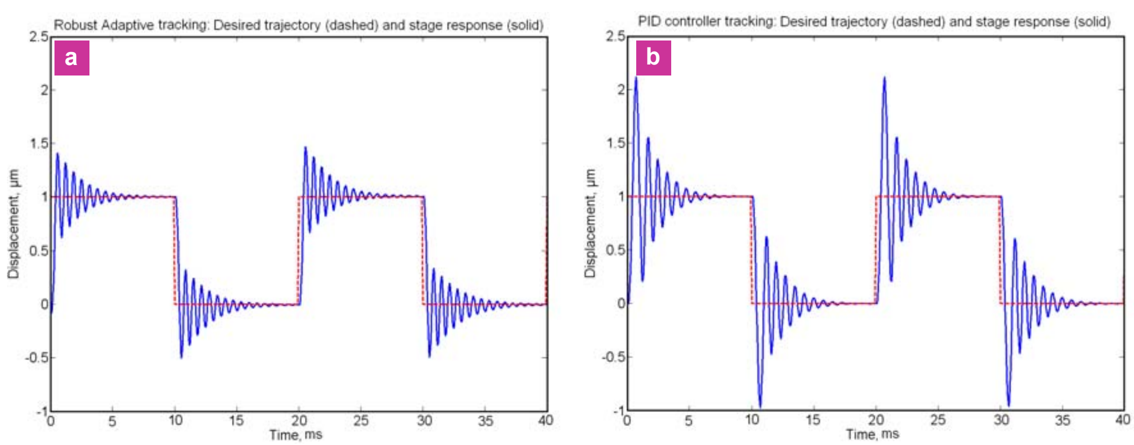

Figure 4.5. Stepped trajectory tracking using (a) robust adaptive and (b) PID controllers tuned for *chirp* tracking.

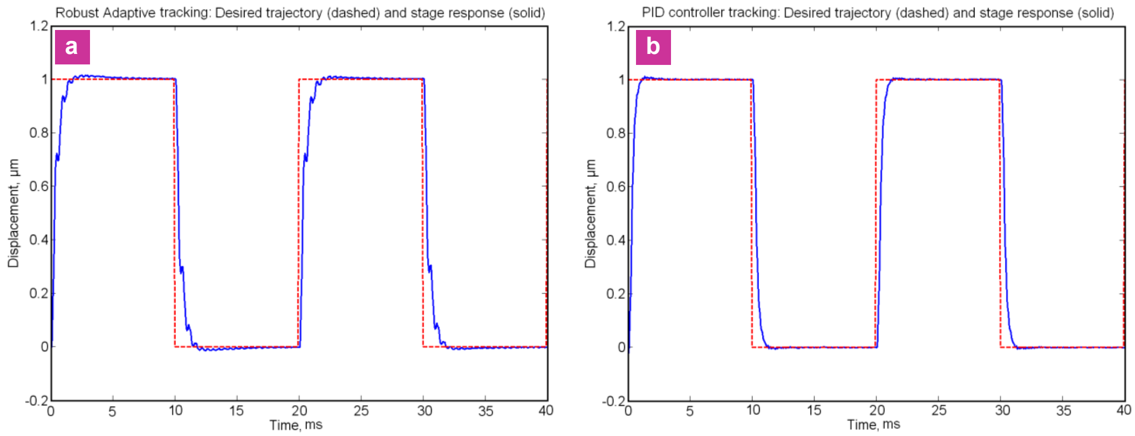

Figure 4.6. Stepped trajectory tracking using (a) robust adaptive and (b) PID controllers tuned for *step* tracking.

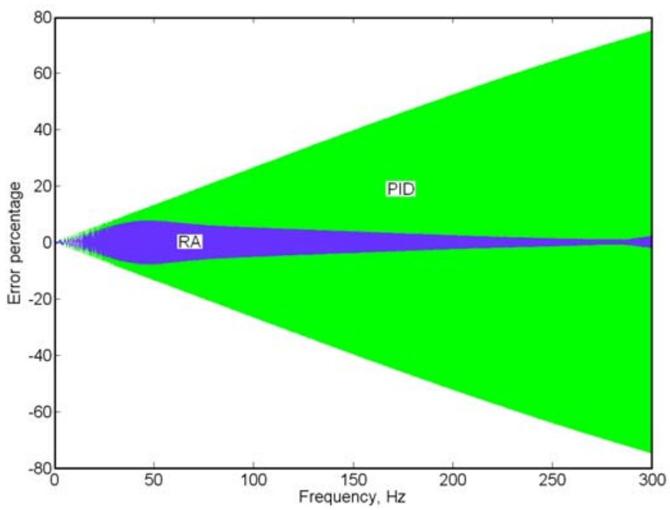

Figure 4.7. Tracking results of 1 μm amplitude chirp trajectory from 0 to 300 Hz for robust adaptive and PID controllers tuned for *step* tracking.

Table 4.1. Robust adaptive control gains used for tracking of chirp and step trajectories.

	η_1	η_2	σ	ε	k_1	k_2	k_3	k_4
Chirp tracking	800	35	5800	0.007	0.5	10^6	5×10^{16}	2×10^6
Step tracking	4800	30	1450	0.01	0.5	10^6	10^{17}	5×10^6

Table 4.2. PID control gains used for tracking of chirp and step trajectories.

	k_P	k_I	k_D
Chirp tracking	28×10^6	11.5×10^{10}	1500
Step tracking	9×10^6	2.25×10^{10}	500

In SPM applications, the piezoelectric stage is responsible of tracking surface topographies with multiple-frequency components and frequent stepped-like discontinuities. Choosing robust adaptive controller for tracking continuously-varying trajectories and PID controller for tracking stepped trajectories, two experiments are carried out here for tracking a representative harmonic trajectory with stepped discontinuities. Figure 4.8 presents the results for both robust adaptive and PID controllers, where each one alone, cannot yield excellent results for such trajectories (the robust adaptive controller lacks desirable transient response at stepped points, while the PID controller yields a poor steady-state tracking performance).

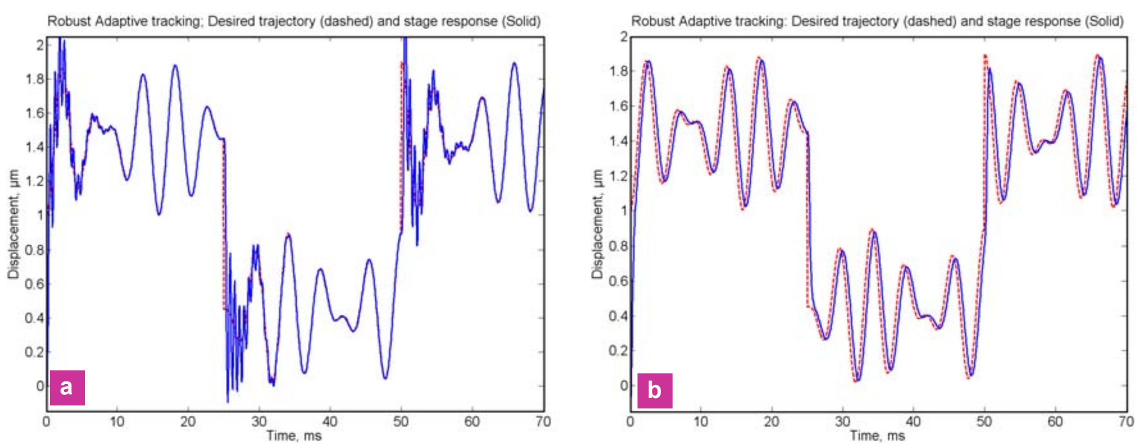

Figure 4.8. Tracking multiple-frequency harmonic trajectory with discontinuities: (a) Robust adaptive controller tuned for *chirp* tracking, and (b) PID controller tuned for *step* tracking.

To achieve a high-performance tracking control while having a desirable transient response at stepped points, a switching controller is proposed here. The robust adaptive controller tuned for chirp tracking will be activated for the continuous trajectories, while the PID controller tuned for step trajectories will be in charge of the discontinuities. Switching conditions need to be carefully assigned as they play significant roles in the stability and performance of tracking in the event of switching from one controller to another. It is remarked that one may choose only the robust adaptive controller and tune the gains in a trade-off between two control objectives. This way, both step and tracking performances are penalized yielding poorer results. The next section presents the switching controller design for achieving high-performance trajectory tracking despite discontinuities.

4.4. Supervisory Switching Controller Design

The objective of switching control is to systematically assign different controllers to the system in order to achieve desired objectives with conflicting requirements. More specifically, we intend to use the robust adaptive controller for tracking of continuous trajectories and switch to PID controller in the event of trajectory jumps. Hence, two switching conditions need to be specified: (i) the condition for switching to PID controller, and (ii) condition for switching back to the robust adaptive controller.

When a jump occurs in the desired trajectory, the position error $e(t)$ changes suddenly, depending on the jump amplitude; however, the time derivative of the position error $\dot{e}(t)$ which is approximated by $\left(e(t)-e(t-\Delta t)\right)/\Delta t$ grows significantly at the jump instance because of sudden error change in a small time step Δt. Hence, it can be a good indicator of discontinuity in the desired trajectory for switching to PID controller. That is, when $\dot{e}(t)$ becomes greater than a preset threshold, i.e., $|\dot{e}(t)| > e_{dtr}$, and the robust adaptive controller is in charge of tracking, the supervisory control law must switch to PID controller and wait until system response converges to the desired trajectory. Once the position error $e(t)$ reaches near zero, i.e., $|e(t)| < e_{tr}$, while the PID controller is operating, the supervisory control law must switch to the robust adaptive controller again to achieve the ideal performance in tracking of the desired trajectory. Since an overshoot-free PID controller design in utilized, the time derivative of error $\dot{e}(t)$ becomes very small when $e(t)$ reaches near zero. Hence, the initial conditions of robust adaptive controller at the switching time are trivial, and may only induce small initial oscillations.

Consequently, the proposed switching control law can be formulated as:

$$v(t) = \begin{cases} v_{PID}(t): \ (\text{if } v(t-\Delta t) \in \text{PID} \,\&\, |e(t)| > e_{tr}) \text{ or } (\text{if } v(t-\Delta t) \in \text{RA} \,\&\, |\dot{e}(t)| > e_{dtr}) \\ v_{RA}(t): \ (\text{if } v(t-\Delta t) \in \text{PID} \,\&\, |e(t)| \le e_{tr}) \text{ or } (\text{if } v(t-\Delta t) \in \text{RA} \,\&\, |\dot{e}(t)| \le e_{dtr}) \end{cases} \tag{4.1}$$

where term $v(t-\Delta t) \in X$ means the control input at the previous time step is generated by controller *X*. Eq. (4.1) states that the control strategy must stay the same or switch to another strategy if one of the switching conditions holds.

Switching stability and performance depends on a number of matching conditions at the switching instances. Particularly, when a switching occurs, the activated controller starts a new task. Hence, a transformation is needed for the time and position coordinates. Figure 4.9 demonstrates switching between two PID and robust adaptive controllers. At every switching instance, the time and position are set to zero for the new control task, meaning the coordinates are transformed to the switching position.

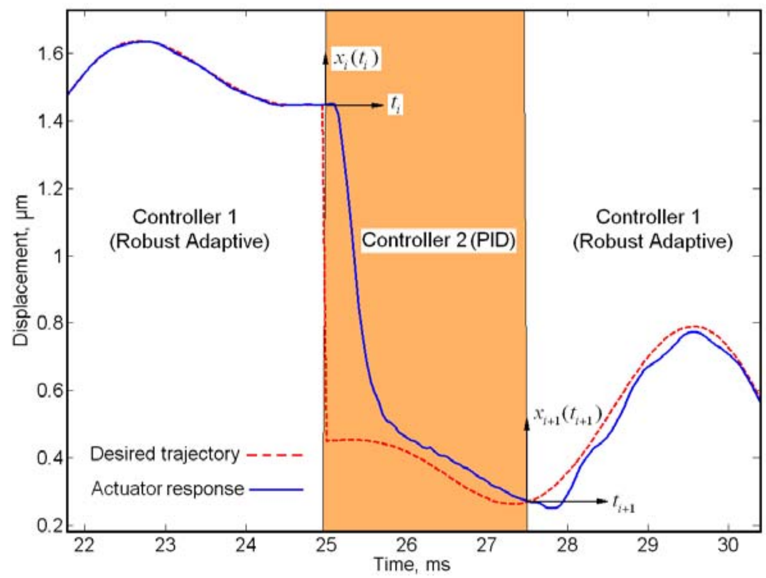

Figure 4.9. A typical step tracking within tracking of a continuous trajectory (controller switches from robust adaptive to PID at the step instance and then switches back to the robust adaptive strategy when actuator response reaches the desired trajectory).

Denoting the i^{th} switching time as t_{si}, and constructing the i^{th} coordinate system based on t_i and $x_i(t_i)$, the following transformations can be given:

$$\begin{aligned} &t_i = t - t_{si},\ t_{si} < t \\ &x_i(t_i) = x(t) - x(t_{si}) \\ &x_{di}(t_i) = x_d(t) - x(t_{si}) \end{aligned} \tag{4.2}$$

which result in:

$$\begin{aligned}
&\dot{x}_i(t_i) = \dot{x}(t) - \dot{x}(t_{si}) = \dot{x}(t) \\
&\dot{x}_{di}(t_i) = \dot{x}_d(t) - \dot{x}(t_{si}) = \dot{x}_d(t) \Rightarrow \ddot{x}_{di}(t_i) = \ddot{x}_d(t) \\
&e_i(t_i) = x_{di}(t_i) - x_i(t_i) = e(t) \Rightarrow \dot{e}_i(t_i) = \dot{e}(t) \\
&s_i(t_i) = \dot{e}_i(t_i) + \sigma e_i(t_i) = \dot{e}(t) + \sigma e(t) = s(t)
\end{aligned} \tag{4.3}$$

Moreover, integrators including adaptation and PID integrals after the switching instance are reset due to the time transformation. For a general function $f_i(t_i)$, this can be written as:

$$\int_0^{t_i} f_i(\tau)d\tau = \int_{t_{si}}^{t} f(\tau)d\tau \tag{4.4}$$

Since the coordinates are transformed, the control input must be transformed as well. That is:

$$v_i(t_i) = v(t) - v(t_{si}),\ t_{si} < t \tag{4.5}$$

Considering the transformation proposed by Eq. (4.2) and the results given by Eqs. (4.3) and (4.4), if the i^{th} switching is from robust adaptive controller to PID controller, one can write:

$$v_{PID}(t) = v(t_{si}) + v_i(t_i) = v(t_{si}) + k_P e(t) + k_I \int_{t_{si}}^{t} e(\tau)d\tau + k_D \dot{e}(t),\ \ t_{si} < t \tag{4.6}$$

And, if the i^{th} switching is from PID controller to robust adaptive controller, we have:

$$\begin{aligned}
v_{RA}(t) = v(t_{si}) + v_i(t_i) = &\\
&v(t_{si}) + \hat{m}_i(t_i)\left(\ddot{x}_d(t) + \sigma\dot{e}(t)\right) + \hat{c}_i(t_i)\dot{x}(t) + \\
&\hat{k}_i(t_i)\left(x(t) - x(t_{si})\right) - \hat{d}_{ci}(t_i) + \eta_1 s(t) + \eta_2 \mathrm{sat}\left(s(t)/\varepsilon\right),\ t_{si} < t
\end{aligned} \tag{4.7}$$

where

$$
\begin{aligned}
\hat{m}_i(t_i) &= \hat{m}(0) + \frac{1}{k_1}\int_{t_{si}}^{t} \mathrm{Proj}_{m_i}\left[s(\tau)\left(\ddot{x}_d(\tau) + \sigma\dot{e}(\tau)\right)\right]d\tau \\
\hat{c}_i(t_i) &= \hat{c}(0) + \frac{1}{k_2}\int_{t_{si}}^{t} \mathrm{Proj}_{c_i}\left[s(\tau)\dot{x}(\tau)\right]d\tau \\
\hat{k}_i(t_i) &= \hat{k}(0) + \frac{1}{k_3}\int_{t_{si}}^{t} \mathrm{Proj}_{k_i}\left[s(\tau)\left(x(\tau) - x(t_{si})\right)\right]d\tau \\
\hat{d}_{ci}(t_i) &= \hat{d}_c(0) + \frac{1}{k_4}\int_{t_{si}}^{t} \mathrm{Proj}_{d_{ci}}\left[-s(\tau)\right]d\tau
\end{aligned}
\qquad (4.8)
$$

Eqs. (4.6)-(4.8) represent the finial forms of control laws for the proposed switching strategy. It is remarked that only three changes are made in the control inputs and their corresponding signals: (i) resetting the integrals, (ii) recording the control input at the switching instance $v(t_{si})$ and adding it to the original control input after switching, and finally (iii) transforming the position feedback $x(t)$ to $x(t) - x(t_{si})$. All other signals remain unchanged.

Figure 4.10 demonstrates a flowchart of the proposed switching control strategy. Setting the initial controller to robust adaptive, the condition for stepped trajectory is checked; if the answer is positive, the controller switches to PID, and if it is negative, it stays on the robust adaptive strategy until a step occurs. If the strategy is on PID control, the controller checks whether the actuator response has reached the desired trajectory or not; if the answer is positive, it switches back to robust adaptive, otherwise it stays on PID control strategy. The controller keeps tracking until a termination command is applied by the computer or the operator. In practice, the switching law can be applied through Rely and Switch operators in computer-based control environments such as Simulink or LabVIEW.

It is remarked that the proposed controller is not limited to switching between PID and robust adaptive controllers; instead any other control pairs, one tuned for step tracking which the other one tuned for continuous trajectory tracking, can be implemented using the proposed switching strategy. However, the modifications imposed by transformation of coordinates must be carefully applied to the control laws.

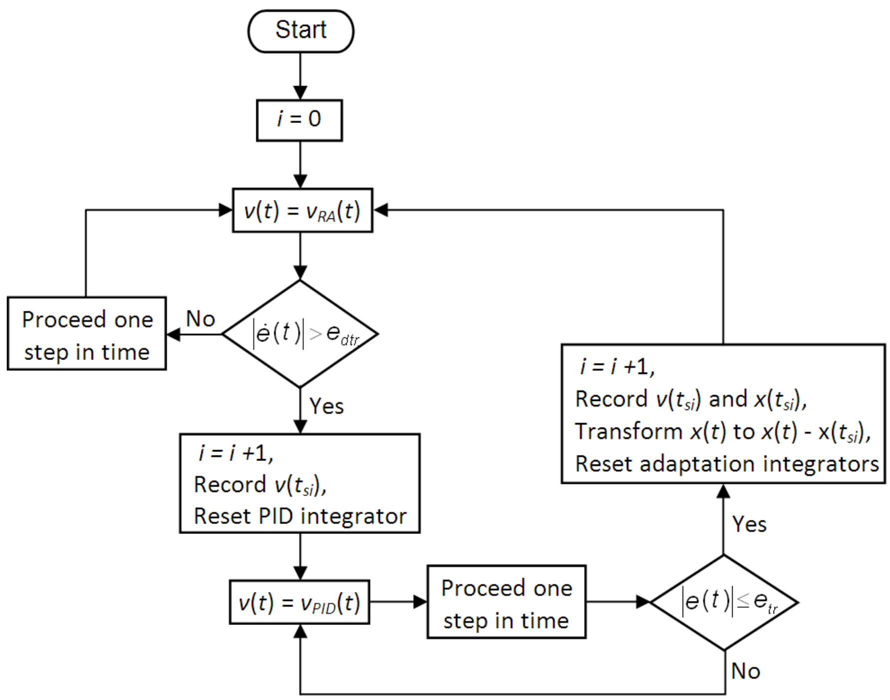

Figure 4.10. Flowchart of the proposed switching strategy between robust adaptive and PID controllers.

The multiple-frequency sinusoidal trajectory depicted in Figure 4.8 is given to the switching controller to assess its tracking performance. The switching thresholds are set to $e_{dtr} = 5\times10^{-4}\, m/\sec$ (corresponding to 25 nm step in $5\times10^{-5}\sec$ time interval) and $e_{tr} = 5\, nm$. Figure 4.11 depicts the tracking results. As seen, the designed switching controller is able to smoothly track a trajectory of combined jumps and high-frequency sinusoids with excellent performance, when compared to the PID and robust adaptive controller responses depicted in Figure 4.8.

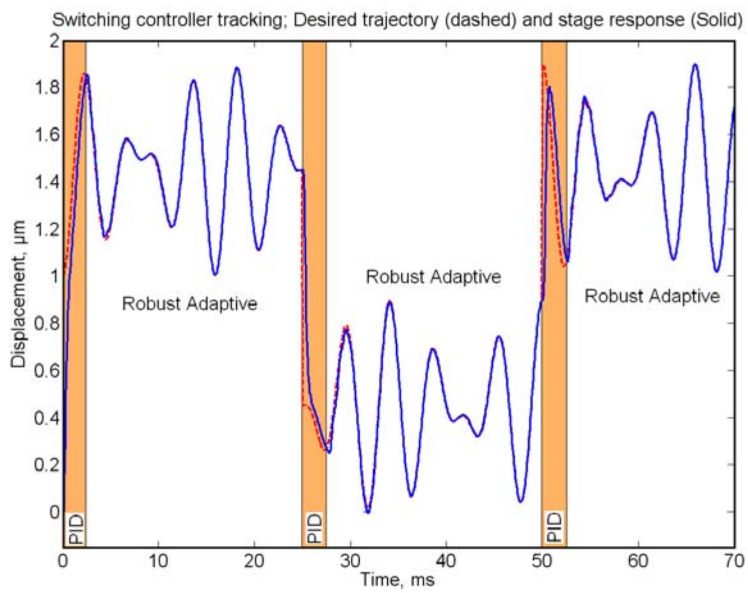

Figure 4.11. Tracking multiple-frequency harmonic trajectory with discontinuities using the proposed switching control strategy.

Chapter Summary

A switching control strategy was proposed for piezoelectric nanopositioning systems for effective tracking control of time-varying continuous trajectories including step discontinuities. A Lyapunov-based robust adaptive controller and a PID controller were employed to study the performance of controllers for tracking of chirp and stepped trajectories. It was shown that when controllers were tuned for chirp tracking, they induced large oscillations for step trajectories. Conversely, when they were tuned for step tracking, they demonstrated low-performance chirp tracking. Moreover, the robust adaptive controller offered more effective performance than PID in chirp tracking, but less for tracking stepped trajectories. Hence, a switching strategy was proposed to decide between the robust adaptive and PID controllers tuned for chirp and step tracking, respectively. Switching conditions were derived and the need for coordinate transformation at switching instances was discussed in detail. The proposed strategy was implemented experimentally and significant improvements were achieved using the proposed controller compared to the individual controllers. This strategy is expected to effectively improve the speed of scanning probe microscopy systems in nano-scale imaging applications.

CHAPTER FIVE

DISTRIBUTED-PARAMETERS MODELING AND CONTROL OF ROD-TYPE SOLID-STATE ACTUATORS*

5.1. Introduction

Rod-type actuators such as piezoelectric, magnetostrictive, electrostrictive and shape memory alloy actuators are distributed-parameters in nature; that is, their equations of motion are described by partial differential equations with appropriate boundary conditions. However, many works have considered lumped-parameters representation for these systems to simplify its analysis and control [26, 31 and 38]. Although such lumped-parameters model can be valid below the first natural frequency of system, it starts to deviate if the operational frequency exceeds the first resonance. Therefore, a distributed-parameters representation is preferred in higher operational frequencies. Nevertheless, only a few references have utilized this representation for their system modeling (see, for example [29, 30]), while they have used approximate methods such as finite element or finite difference schemes to solve the equations of motion.

Tracking control of flexible mechanical systems suffers from lack of a unified approach that can be utilized independent of the structure configuration. Although various controllers have been proposed for control of flexible systems, they mostly concentrate on set-point or quasi-static tracking problems where the effects of high

* The contents of this chapter may have come directly or indirectly from our joint publication [62].

frequency modes are typically ignored [63, 64]. Moreover, the control of multiple-mode flexible systems has been widely studied in vibration suppression applications [65-67]. Despite these developments, the research is open for flexible structures on tracking time-varying and high-frequency trajectories.

In this chapter, the standard vibration analysis methods are utilized to derive the state-space representation of rod-type solid-state actuators. The forced vibration analysis is carried out by including the actuation force, structural damping, and damping of the flexure at the boundary. The truncated k-mode state-space representation of system is explicitly derived using system parameters and modal properties. To achieve high bandwidth tracking control, a new state-space controller is proposed and implemented for tracking continuously-varying desired trajectories within a broad frequency range. Numerical simulations indicate that for precise control of system with a high bandwidth tracking specification, sufficient number of system modes must be included in the controller. This necessitates the need for developing distributed-parameters modeling and control approaches. Integration of state observers and robustness features to the controller are proposed and discussed for enabling practical implementation.

5.2. System Configuration and Modeling

Figure 5.1 depicts the schematic configuration as well as representative model of a typical rod-type solid-state actuator. Having mass per unit length ρ, stiffness E, damping coefficient B, length L, and cross-sectional area A, the actuator is modeled as a distributed-parameters rod subjected to a compound boundary condition of a mass m, damper c and spring k as shown in Figure 1. Moreover, the actuation force $f(t)$, which is the equivalent of a distributed internal stress, can be applied at the boundary as a concentrated load. The present work is aimed at: (i) deriving the modal characteristics of actuator including its natural frequencies and mode shapes, (ii) obtaining the state-space representation by carrying out the forced vibration analysis, and finally (iii) designing control laws for the actuator tip to precisely track desired time-varying trajectories. The advantage of the state-space representation is in the unique control framework proposed for multiple-mode tracking of distributed-parameters system.

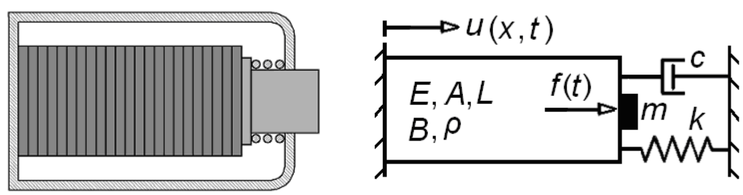

Figure 5.1. Schematic of a solid-state actuator (left) and its representative rod model (right).

The governing equation for the longitudinal (axial) vibrations of the actuator subjected to axial force $f(t)$ at the tip is derived using the extended Hamiltonian principal given by:

$$\int_{t_1}^{t_2} \left(\delta \left(T - V \right) + \delta W_{ext} \right) dt = 0 \tag{5.1}$$

where T, V and W_{ext} are, respectively, the kinetic energy, potential energy and the external work of rod in the presence of time-varying force $f(t)$. The longitudinal displacement $u(x,t)$ is assumed to be varying over the entire length of the actuator.

By using the extended Hamilton's principal and taking several integrations by parts, (refer to Appendix A) the governing equation of motion (5.2) and the boundary conditions (5.3) for the system are obtained as:

$$\rho\left(\frac{\partial^2 u(x,t)}{\partial t^2}\right) - EA\left(\frac{\partial^2 u(x,t)}{\partial x^2}\right) + B\left(\frac{\partial u(x,t)}{\partial t}\right) = 0 \tag{5.2}$$

$$u(0,t) = 0, \quad m\left(\frac{\partial^2 u(L,t)}{\partial t^2}\right) + EA\left(\frac{\partial u(L,t)}{\partial x}\right) + C\left(\frac{\partial u(L,t)}{\partial t}\right) + ku(L,t) = f(t) \tag{5.3}$$

These equations can be approximated with a finite-mode state-space representation as discussed in the next sections.

3.3. Modal Analysis of the System

Modal characterization of system is performed by a standard procedure for free and un-damped vibration analyses. Setting the damping to zero in Eq. (5.2), the equation of motion reduces to:

$$\rho\left(\frac{\partial^2 u(x,t)}{\partial t^2}\right) = EA\left(\frac{\partial^2 u(x,t)}{\partial x^2}\right) \tag{5.4}$$

By assuming that the solution of Eq. (5.4) is separable in time and space domains, the longitudinal displacement of rod can be written as:

$$u(x,t) = \phi_r(x) q_r(t) \tag{5.5}$$

where $\phi_r(x)$ is known as the spatial modal function and $q_r(t)$ is the generalized time-dependant coordinate. Substituting Eq. (5) into Eq. (4) yields:

$$\left(\frac{\ddot{q}_r(t)}{q_r(t)}\right)=\left(\frac{EA}{\rho}\right)\frac{\phi_r''(x)}{\phi_r(x)}=-\omega_r^2 \tag{5.6}$$

where ω_r is a constant parameter representing the natural frequency for the r^{th} mode of actuator. Hence, Eq. (5.6) can be split into time-domain and spatial equations as:

$$\ddot{q}_r(t)+\omega_r^2 q_r(t)=0 \tag{5.7}$$

$$\phi_r''(x)+\beta_r^2\phi_r(x)=0 \tag{5.8}$$

where

$$\beta_r^2=\frac{\rho\omega_r^2}{EA} \tag{5.9}$$

The general solution of the equation of motion in the spatial domain can be written as:

$$\phi_r(x)=C_r\sin\beta_r x+D_r\cos\beta_r x \tag{5.10}$$

At the fixed boundary, we have $\phi_r(0)=0$ which results in $D_r=0$. Hence, modal functions are simplified to:

$$\phi_r(x)=C_r\sin\beta_r x \tag{5.11}$$

To quantify C_r and β_r, we apply the separation of variables to the free and un-damped boundary condition of system at $x = L$ to obtain:

$$m\phi_r(L)\ddot{q}_r(t)+EA\phi_r'(L)q_r(t)+k\phi_r(L)q_r(t)=0 \tag{5.12}$$

By substituting Eq. (5.7) and Eq. (5.11) into Eq. (5.12) and with further simplifications, the characteristics equation of system is obtained as:

$$\left[k-\left(mEA/\rho\right)\beta_r^2\right]\sin\left(\beta_r L\right)+EA\beta_r\cos\left(\beta_r L\right)=0 \tag{5.13}$$

The numerical solution of (5.13) yields infinite solutions for β_r and natural frequencies according to Eq. (5.9). For the r^{th} mode shape of system given by:

$$\phi_r(x)=C_r\sin\left(\sqrt{\rho/EA}\,\omega_r x\right) \tag{5.14}$$

coefficient C_r is calculated using a orthonormality condition with respect to mass (refer to Appendix B for detailed derivations) as:

$$\rho\int_0^L \phi_r(x)\phi_s(x)dx+m\phi_r(L)\phi_s(L)=\delta_{rs} \tag{5.15}$$

where δ_{rs} is the Kronecker delta (i.e. $\delta_{rs}=1$ if $r=s$ and $\delta_{rs}=0$ if $r\neq s$).

Substituting Eq. (5.14) into Eq. (5.15) and simplifying it, the following explicit expression is obtained:

$$C_r=\left[\rho\int_0^L \sin^2\left(\sqrt{\rho/EA}\,\omega_r x\right)dx+m\sin^2\left(\sqrt{\rho/EA}\,\omega_r L\right)\right]^{-\frac{1}{2}} \tag{5.16}$$

Utilizing the derived equations and expressions for system natural frequencies and mode shapes, we present, next, the forced motion analysis of system where the effects of excitation force and damping are taken back into account to form the state-space equations of system.

5.4. Forced Motion Analysis

While the system modal functions and natural frequencies are obtained through the free motion analysis, the actual response is affected by the presence of damping and the actuation force. Hence, further analysis is required to derive a comprehensive model which includes both free and forced responses of system. The widely-used expansion theorem [68] is utilized here to solve the problem. Based on this theorem, the longitudinal displacement function is assumed to be equal to an infinite series of system modal responses as:

$$u(x,t)=\sum_{r=1}^{\infty}\phi_r(x)q_r(t) \tag{5.17}$$

By this assumption, the partial differential equation of motion, Eq. (5.2), can be recast as an infinite series:

$$\sum_{r=1}^{\infty}\left\{\rho\phi_r(x)\ddot{q}_r(t)-EA\phi_r''(x)q_r(t)+B\phi_r(x)\dot{q}_r(t)\right\}=0 \tag{5.18}$$

Multiplying Eq. (5.18) by $\phi_s(x)$, taking an integral over the entire length of rod, and applying integral by parts, yields:

$$\begin{aligned}\sum_{r=1}^{\infty}\Big\{&\rho\ddot{q}_r(t)\int_0^L\phi_r(x)\phi_s(x)dx-EAq_r(t)\phi_r'(L)\phi_s(L)+\\&EAq_r(t)\int_0^L\phi_r'(x)\phi_s'(x)dx+B\dot{q}_r(t)\int_0^L\phi_r(x)\phi_s(x)dx\Big\}=0\end{aligned} \tag{5.19}$$

On the other hand, substituting Eq. (5.17) into Eq. (5.3), the boundary condition at $x = L$ becomes:

$$\sum_{r=1}^{\infty}\{m\phi_r(L)\ddot{q}_r(t)+EA\phi_r'(L)q_r(t)+C\phi_r(L)\dot{q}_r(t)+k\phi_r(L)q_r(t)\}=f(t) \tag{5.20}$$

Substituting $EA\phi_r'(L)q_r(t)$ from Eq. (5.20) into Eq. (5.19) and rearranging the terms, one can obtain:

$$\begin{aligned}\sum_{r=1}^{\infty}\Big\{&\left[\rho\int_0^L\phi_r(x)\phi_s(x)dx+m\phi_r(L)\phi_s(L)\right]\ddot{q}_r(t)+\left[B\int_0^L\phi_r(x)\phi_s(x)dx+C\phi_r(L)\phi_s(L)\right]\dot{q}_r(t)\\&+\left[EA\int_0^L\phi_r'(x)\phi_s'(x)dx+k\phi_r(L)\phi_s(L)\right]q_r(t)\Big\}=\phi_s(L)f(t)\end{aligned} \tag{5.21}$$

Applying the orthonormality conditions with respect to mass (Eq. 5.15) and stiffness (refer to Appendix A for the detailed derivations) given as:

$$EA\int_0^L\phi_r'(x)\phi_s'(x)dx+k\phi_r(L)\phi_s(L)=\omega_r^2\delta_{rs} \tag{5.22}$$

Eq. (5.21) is simplified to:

$$\sum_{r=1}^{\infty}\left\{\delta_{rs}\ddot{q}_r(t)+\left[B\int_0^L\phi_r(x)\phi_s(x)dx+C\phi_r(L)\phi_s(L)\right]\dot{q}_r(t)+\omega_r^2\delta_{rs}q_r(t)\right\}=\phi_s(L)f(t),\quad r=1,2,... \tag{5.23}$$

which can be rewritten as:

$$\ddot{q}_r(t)+\sum_{s=1}^{\infty}\{d_{rs}\dot{q}_s(t)\}+\omega_r^2q_r(t)=f_r(t) \tag{5.24}$$

where

$$d_{rs}=B\int_0^L\phi_r(x)\phi_s(x)dx+C\phi_r(L)\phi_s(L),\ \ f_r(t)=\phi_r(L)f(t) \tag{5.25}$$

The truncated k-mode description of Eq. (5.24) can be presented in the following matrix form:

$$\mathbf{M}\ddot{q}(t)+\mathbf{D}\dot{q}(t)+\mathbf{K}q(t)=\mathbf{F}u \tag{5.26}$$

where

$$\begin{aligned}&\mathbf{M}=\left[\delta_{rs}\right]_{k\times k}\,,\ \mathbf{D}=\left[d_{rs}\right]_{k\times k}\,,\ \mathbf{K}=\left[\omega_r^2\delta_{rs}\right]_{k\times k}\,,\ q=\left[q_1(t),q_2(t),...,q_k(t)\right]_{k\times 1}^T\,,\\&\mathbf{F}=\left[\phi_1(L),\phi_2(L),.....,\phi_k(L)\right]_{k\times 1}^T,\ u=f(t)\end{aligned} \tag{5.27}$$

Eventually, Eq. (5.26) can be converted into the following state-space representation:

$$\begin{aligned}\dot{x}(t)&=\mathbf{A}x(t)+\mathbf{B}u(t)\\y(t)&=\mathbf{C}x(t)\end{aligned} \tag{5.28}$$

where

$$\mathbf{A}=\begin{bmatrix}\mathbf{0} & \mathbf{I}\\ -\mathbf{M}^{-1}\mathbf{K} & -\mathbf{M}^{-1}\mathbf{D}\end{bmatrix}_{2k\times 2k},\ \mathbf{B}=\begin{bmatrix}\mathbf{0}\\ \mathbf{M}^{-1}\mathbf{F}\end{bmatrix}_{2k\times 1},\ x(t)=\begin{Bmatrix}q(t)\\ \dot{q}(t)\end{Bmatrix}_{2k\times 1}, \tag{5.29}$$

and considering rod's displacement at $x = L$ as the system output, i.e. $y(t) = u(L, t)$, the output matrix is given by:

$$\mathbf{C}=[\phi_1(L),\phi_2(L),...,\phi_k(L),0,...,0]_{1\times 2k}\,, \tag{5.30}$$

according to the truncated k-mode approximation of Eq. (5.17).

5.5. Numerical Simulations

A set of numerical simulations are carried out in this section to assess different aspects of the developed modeling framework. The initial simulations investigate the effects of boundary mass and spring on the natural frequencies and modal functions of system. The first four natural frequencies are plotted versus different values of spring k, while setting m to zero, in Figure 2(a), and versus boundary mass m, while taking k as zero, in Figure 2(b). Other parameters used for these simulations are taken as: $\rho = 6000\ kg/m^3$, $d = 0.01\ m$ (rod diameter), $L = 0.1\ m$, and $E = 100\ GPa$. These values may represent those of a real solid-state micro-positioning actuator.

It can be observed from Figure 5.2 that as the stiffness of the boundary spring increases, the natural frequencies of all modes increase exponentially, but eventually converge to particular values. This is because of the fact that rod with a hard spring at the boundary behaves similarly to that of clamped-clamped rods. Hence, further increase in the spring stiffness will not affect the natural frequencies much. A similar phenomenon occurs in a reverse way with increasing the values of boundary mass. That is, the natural frequencies decrease as the value of boundary mass increases until they get saturated at particular values. Interestingly, the natural frequencies of a rod with a hard spring at boundary are close to those of the rod with a heavy mass at the boundary with one mode ahead. For instance, the *first* and the *second* natural frequencies of the rod with a hard boundary spring are respectively near the *second* and the *third* natural frequencies of a rod with a heavy boundary mass.

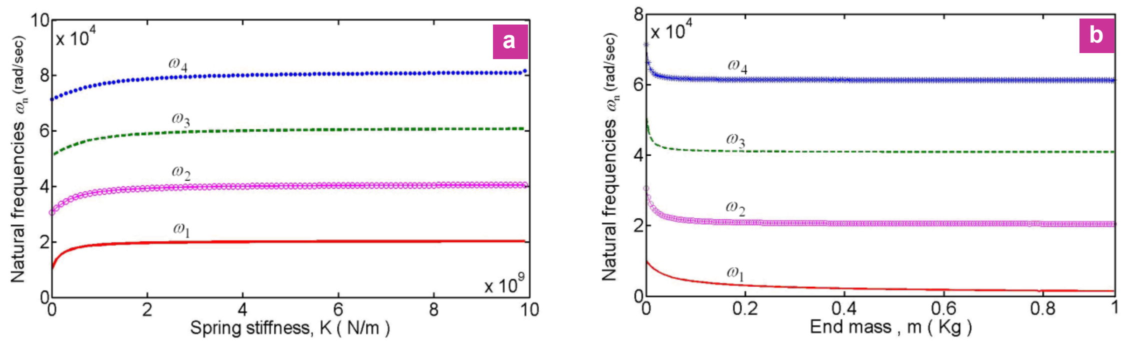

Figure 5.2. First four natural frequencies of rod versus (a) boundary spring stiffness k and (b) boundary mass m.

To study the behavior of mode shapes with the change in the values of boundary spring and mass, the first four modal functions of rod are plotted for four different configurations: (C1) $m = 0$ with high k, (C2) $m = 0$, with $k = 0$, (C3) moderate m with moderate k, and (C4) high m with high k. The selected parameters for the simulations are given in Table 5.1 and the results are depicted in Figure 5.3. The significant changes in all of the four modal functions are observed from one configuration to another. By carefully observing the modal functions, one can see modal functions of rod with boundary configuration C1 ($m = 0$ with high k) are similar to those of the rod with both ends clamped. It can also be seen from the figures that the modal functions of configuration C1 follow those of configuration C4 (high m and k) with one mode forward (e.g. the first mode shape of C1 is similar to the second mode shape of C4).

The Bode diagram of configuration C3 (moderate m with moderate k), which seems to be a more realistic case, for the first four modes is depicted in Figure 5.4. As expected, a uniform multi-modal frequency response is seen from this diagram which could indicate the validity of the proposed modeling framework.

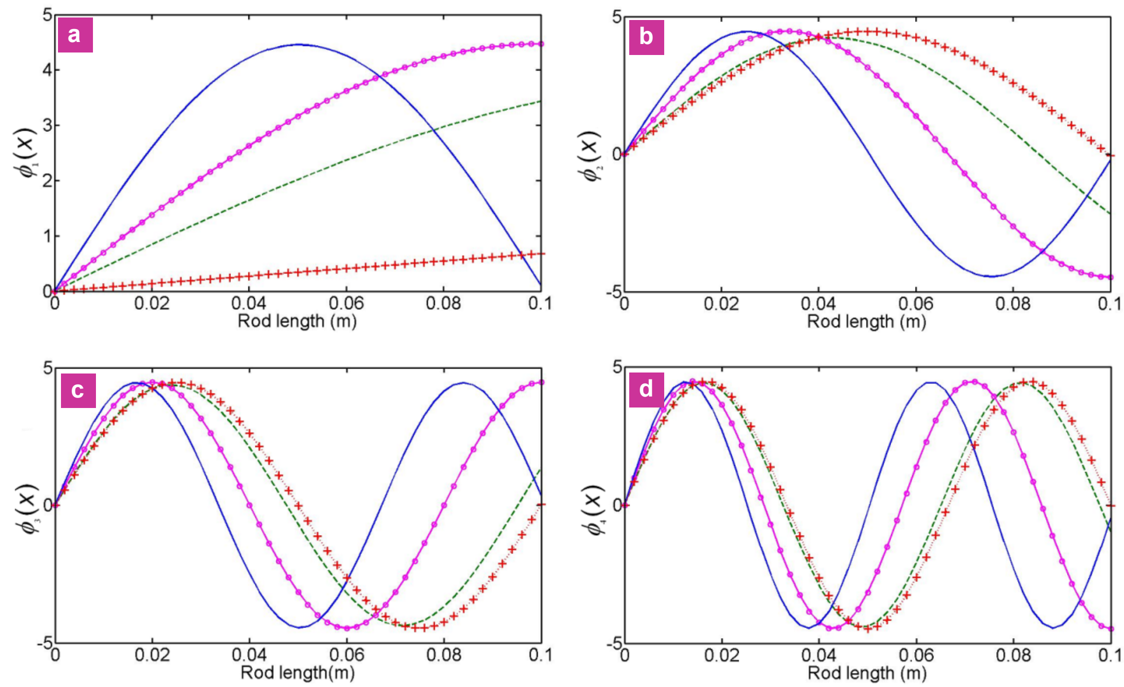

Figure 5.3. (a) First, (b) second, (c) third, and (d) fourth modal function of rod for four different configurations of boundary mass and spring (C1, C2, C3, C4).

Table 5.1. Parameters used for numerical simulations to calculate mode shapes.

Config.	m (kg)	k (N/m)	ω_1 (kHz)	ω_2 (kHz)	ω_3 (kHz)	ω_4 (kHz)
C1	0	10^{10}	20.25	40.5	60.76	81
C2	0	0	10.21	30.62	51.03	71.44
C3	0.02	10^4	7.31	24.09	43.04	62.79
C4	1	0	1.39	20.5	40.87	61.27

Other Actuator parameters:
Rod's damping coefficient: $B = 0.1$ (N.sec/ m^2),
External damping coefficient: C = 0.05 (N.sec/m),

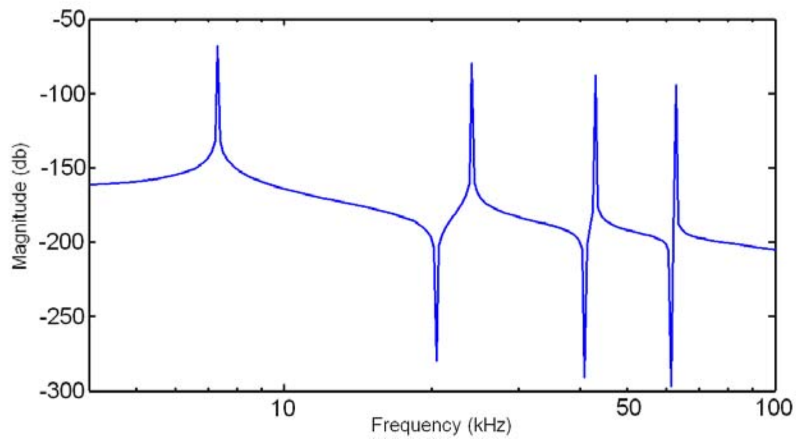

Figure 5.4. Bode plot of system with four modes and boundary condition of configuration C3.

5.6. State-Space Control Development

The development of a straightforward state-space controller for asymptotic output tracking control of linear systems not only can benefit the control of present rod-type actuator, but also can be applied to a variety of dynamical systems. In this section, a new form of state-space control law is proposed for output tracking control of second order single-input single-output (SISO) mechanical systems which is applied for high bandwidth tracking control of rod-type solid-state actuators.

5.6.1. State-Space Control Design

For the actuator tip to follow a two times continuously differentiable desired trajectory, $y_d(t)$, the tracking error is represented as:

$$e(t) = y_d(t) - y(t) \tag{5.31}$$

Taking the time derivative of Eq. (5.31) and using Eq. (5.28) yields:

$$\begin{aligned} \dot{e}(t) = \dot{y}_d(t) - \dot{y}(t) = \\ \dot{y}_d(t) - \mathbf{C}\dot{x}(t) = \\ \dot{y}_d(t) - \mathbf{CA}x(t) - \mathbf{CB}u(t) \end{aligned} \tag{5.32}$$

It can be shown that for the present actuator or other flexible structures (e.g. beams, plates, shells) with inputs being applied forces and outputs being displacements, the term ***CB*** is always zero. This implies that first order state-space controller cannot be used for tracking of desired trajectories in the form of displacement. Letting ***CB*** = 0 and differentiating one more time from the tracking error yields:

$$\begin{aligned} \ddot{e}(t) &= \ddot{y}_d(t) - \mathbf{CA}\dot{x}(t) \\ &= \ddot{y}_d(t) - \mathbf{CA}^2x(t) - \mathbf{CAB}u(t) \end{aligned} \tag{5.33}$$

Similarly, it can be shown that the term ***CAB*** in equation Eq. (5.33) becomes nonzero for the flexible mechanical structures. Hence, a second order state-space control law presented in the next theorem can be utilized to control the actuator displacement.

Theorem 5.1. For the SISO state-space system given in Eq. (5.28) which satisfies ***CB*** = 0 and $\boldsymbol{CAB} \neq 0$, the following control law leads to asymptotic convergence of the tracking error, i.e. $e \to 0$ as $t \to \infty$, provided that all the signals are bounded.

$$u(t) = \left\{\mathbf{CAB}\right\}^{-1}\left(\ddot{y}_d(t) - \mathbf{CA}^2x(t) + k_1\dot{e}(t) + k_2e(t)\right);\;\; k_1, k_2 > 0 \tag{5.34}$$

Proof: Substituting the control law given by Eq. (5.34) into Eq. (5.33), an equation representing the error dynamics of system is obtained, that is:

$$\ddot{e}(t) + k_1\dot{e}(t) + k_2e(t) = 0 \tag{5.35}$$

Since k_1 and k_2 are positive constants, Eq. (5.35) represents a stable second-order differential equation with the roots of its characteristics equation being located in the left side of the complex plane. This indicates that asymptotic convergence of the tracking error $e(t)$ is achieved.

5.6.2. State-Space Controller Simulations

The proposed control law is numerically implemented on the actuator model with configuration C3, assuming that the system output and state vectors are measurable in real-time. Two sinusoidal reference signals with amplitude of 10 μm at 1 kHz and 50 kHz frequencies are considered as the desired trajectories. A phase shift of 60 degrees has been applied to achieve a nonzero initial error value and assess the controller transient response. The values of k_1 and k_2 are respectively selected as 70000 and 1.225×10^9 so that a critically damped error dynamics with the natural frequency of 35000 rad/sec (5573 kHz) is achieved. The sampling rate is set to 100 MHz to maintain the stability of numerical integrations. It is remarked that the critically damped error dynamics offers a suitable stability and performance because of its fast settling time without overshoot. Moreover, higher natural frequency of a critically damped error dynamics results in faster settling time; however, this value cannot be increased above a certain threshold in practice which is determined by the chatter effect.

Figure 5.5 depicts the tracking results which demonstrate that the controller is able to precisely track both low- and high-frequency trajectories with identical exponential convergence rates. There are small amplitude oscillations in the tracking error, particularly at the high-frequency trajectory, due to the ever-present approximation in the numerical integrations. While the system output converges to the desired trajectory within the first cycle of the low-frequency input, it takes a few cycles to converge to the high frequency trajectory. However, this can be modified by increasing the control gains to achieve a desirable response.

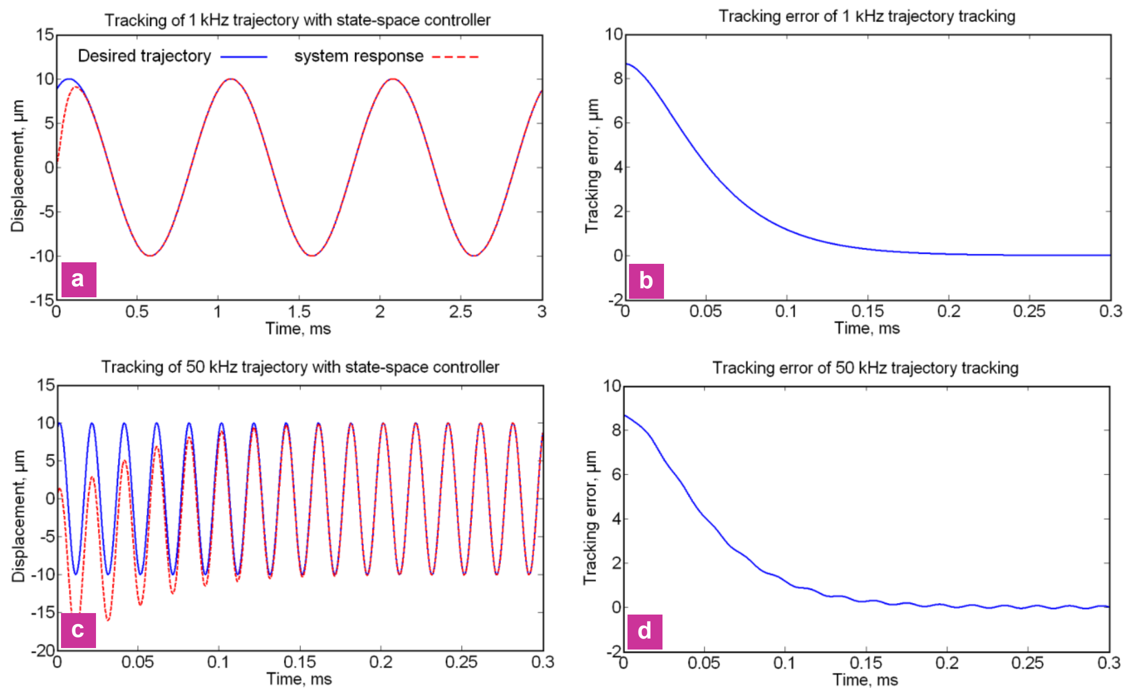

Figure 5.5. Tracking control results using the proposed state-space control law; (a) 1 kHz sinusoidal trajectory tracking and (b) its tracking error, (c) 50 kHz sinusoidal trajectory tracking and (d) its tracking error.

5.7. State Observer Design and Integration

In many real applications, only actuator's tip displacement (system output) is measurable. This limits the implementation of the proposed controller which requires full-state feedback. Hence, the use of state estimators or observers in the feedback loop can be considered to effectively overcome this problem. Closed-loop state observers have been widely used in feedback control techniques when the direct measurements of states are not possible. Yet, the observability of the system must be investigated. Unfortunately, the present state-space model for the rod-type actuator does not agree with the observability condition, because the rank of observability matrix becomes less than the system order, meaning that it is not guaranteed to set the closed-loop observer poles at any desired locations. However, noting that the open-loop system is stable (which implies that the state vector is detectable) one can set the observer poles close to desired locations by optimally tuning the closed-loop observer gains.

The classical closed-loop observer for a linear system is given by [69]:

$$\dot{\hat{x}}(t) = \mathbf{A}\hat{x}(t) + \mathbf{B}u(t) + \mathbf{L}\left(y(t) - \mathbf{C}\hat{x}(t)\right) \tag{5.36}$$

where $\hat{x}(t)$ is the observed state vector, and $\boldsymbol{L}$ is the observer gain matrix. To obtain the observer error dynamics, the state observation error is defined as:

$$\tilde{x}(t) = x(t) - \hat{x}(t) \tag{5.37}$$

Taking the time derivative of Eq. (5.37) and using Eqs. (5.28) and (5.36) yields:

$$\dot{\tilde{x}}(t) = \left(\mathbf{A} - \mathbf{LC}\right)\tilde{x}(t) \tag{5.38}$$

Eq. (5.38) is a first order differential equation representing the observer error dynamics. The only condition for its asymptotic stability of the observer is for the eigenvalues of matrix (***A* - *LC***) to be located in the left side of the complex plane. The simplest choice would be setting $\boldsymbol{L}$ to zero and use an open-loop observer since the eigenvalues of matrix $\boldsymbol{A}$ for the present system have negative real parts. However, the possible presence of uncertainties and disturbances in the system and the poor transient response of open-loop observer because of system low damping necessitate the use of a closed-loop observer. The objective is to choose the gain matrix $\boldsymbol{L}$ such that a stable error dynamics is achieved with its eigenvalues all pushed toward left and concentrated around the real axis to enhance both stability and transient response of observation. It is remarked that the observer eigenvalues cannot be moved more leftward than a certain value in practice because of the need for smaller sampling time to solve the observer differential equation in real-time than that digital signal processing systems could offer.

A random optimization algorithm is utilized to optimally locate the observer poles around the desired locations. The advantage of the random optimization over the gradient-based methods is in its seeking for the global extremum of the given objective function [70]. Figure 5.6 depicts three different sets of optimal locations of observer poles for the desired locations being set to -1000, -20000, and -50000 on the real axis. Although the observer poles can be moved leftward leading to more stable configuration, they cannot be all located on the real axis to yield a desired transient response. However, the poles have been attempted to be squeezed around the real axis through the proposed optimization algorithm within the constraints of the problem, most important of which is the lack of the observability condition. Nevertheless, desirable steady-state responses are expected.

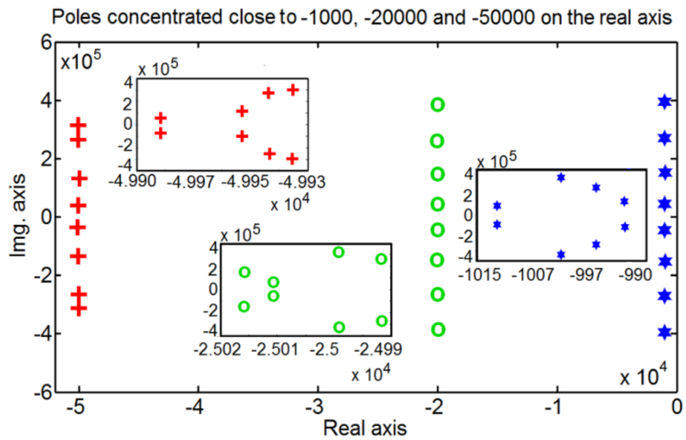

Figure 5.6. Optimal location of the observer poles around -1000, -20000 and -50000 on the real axis.

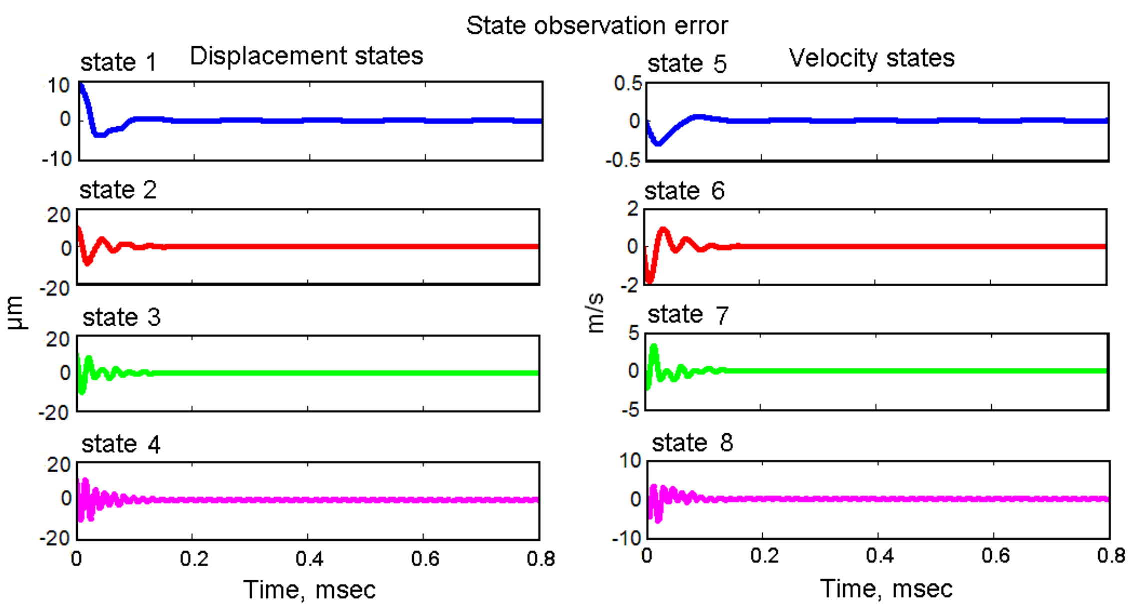

Figure 5.7. Convergence of the state observer errors to zero despite a 20 kHz input excitation, for the observer poles located around -50000 on the real axis.

To assess the performance of the observer in estimating the state-vector, a simulation is carried out by setting the observer poles around -50000 on the real-axis and applying an initial condition and an input force at 20 kHz on the system. The results are depicted in

Figure 5.7, where all the eight state observation errors converge to zero. There are limited oscillations at the beginning, but the steady-state responses are all excellent.

The designed observer can now be integrated with the proposed state-space controller to effectively solve the problem associated with the unavailability of state feedback in practice. By integrating Eq. (5.34) with Eq. (5.36), the state-space control law with the observer integration is given by:

$$\begin{aligned} u(t) &= \{\mathbf{CAB}\}^{-1}\left(\ddot{y}_d(t) - \mathbf{CA}^2\hat{x}(t) + k_1\dot{e}(t) + k_2 e(t)\right);\ k_1, k_2 > 0 \\ \dot{\hat{x}}(t) &= \mathbf{A}\hat{x}(t) + \mathbf{B}u(t) + \mathbf{L}\left(y(t) - \mathbf{C}\hat{x}(t)\right) \end{aligned} \tag{5.39}$$

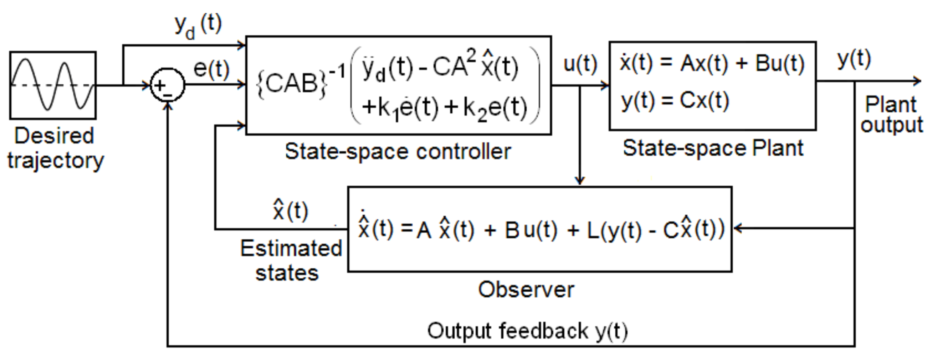

Figure 5.8. Integrated state-space controller/observer diagram for practical control of rod-type actuators.

Figure 5.8 demonstrates the block diagram of the control structure. As seen, the observer receives plant input and output, and feeds the estimated states back to the controller. Using this strategy, the simulations of tracking control for 1 kHz and 50 kHz desired trajectories studied in subsection 5.6.2 are repeated here. Results are depicted in Figure 5.9, where both transient and steady-state responses are about the same as those of the case when system exact state feedback is utilized. These simulations indicate the viability of the proposed controller/observer strategy.

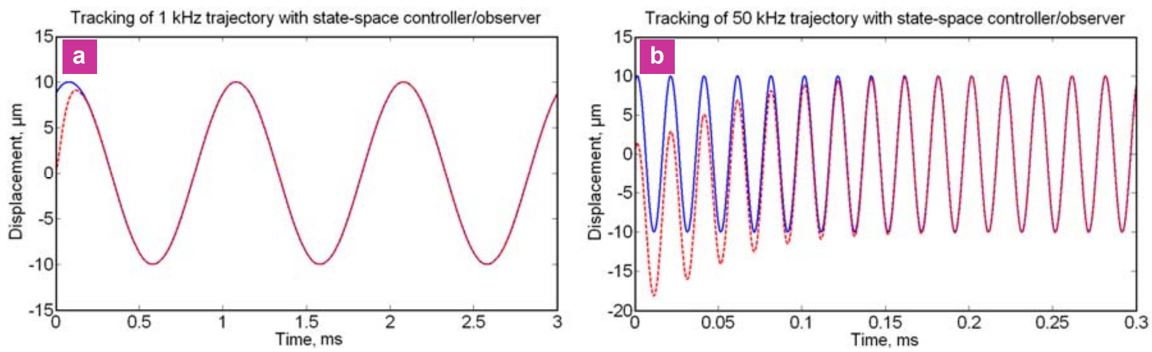

Figure 5.9. Tracking control of (a) 1 kHz and (b) 50 kHz sinusoidal trajectories using the combined controller/observer strategy.

The identical tracking results of state-space controller with exact state feedback (Figure 5.5) and with observed state feedback (Figure 5.9) is because of the identical initial conditions used for the plant and observer in the simulations. This is due to the fact that for most of rod-type solid-state actuators in real applications, the plant is initially at rest with zero initial conditions. However, one may also argue that the effects of state feedback can be negligible compared to other terms in the control law. To clarify this issue, the state observer is disconnected from controller and the simulations are repeated. As seen from Figure 5.10, poor tracking results prove the importance of the state observer integration in achieving high-performance tracking.

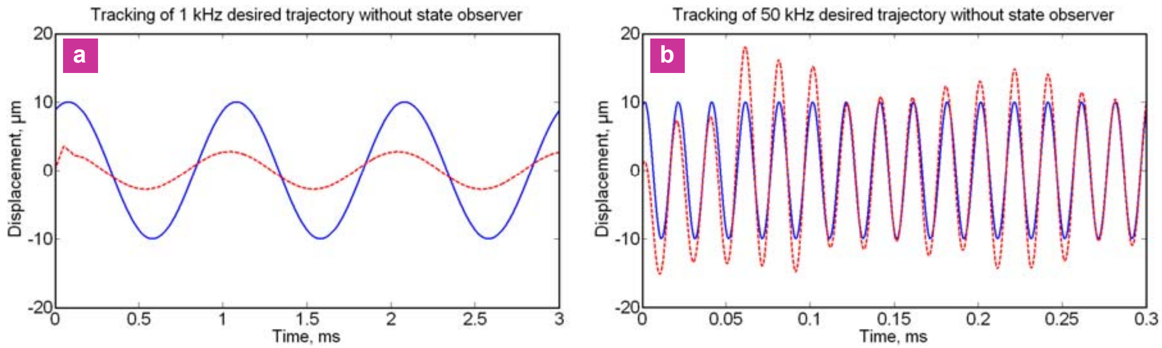

Figure 5.10. Tracking control of (a) 1 kHz and (b) 50 kHz sinusoidal trajectories without using the state feedback.

5.8. Assessment of Controller Bandwidth

One of the main objectives of this work is to achieve a high bandwidth tracking controller for rod-type solid-state actuators for any desired frequency ranges. In the present framework and because of the practical limitations, the effects of higher modes are neglected. Hence, a truncated model has been proposed based on which the controller is formulated. However, a real actuator has infinite number of modes and the truncation may lead to considerable tracking errors. In this section, we study how the modes truncation affects the controller performance and bandwidth.

A four-mode rod-type actuator model with configuration $C3$ is assumed here to represent an actual plant. Four different controllers are formed based on one, two, three, and four modes approximation of the plant, respectively. It is expected that the controllers with higher number of modes offer better tracking bandwidth. A 10 μm amplitude desired trajectory is applied to the system with its frequency incrementally changed from 1 to 80 kHz to cover all the plant resonant frequencies. The steady-state tracking error amplitude is plotted versus frequency to continuously demonstrate the performance of the proposed controller/observer over the frequency range of interest. Plant limited-mode approximations as well as their corresponding tracking results are depicted in Figure 5.11. It is seen that the controller is able to only subside the tracking error for the included modes. For instance, the controller with one mode approximation is able to precisely track the desired trajectory only below the second resonance; except for the first resonance, tracking error suffers from the unexpected large peaks of the higher modes. As the number of included modes in the controller increases, the tracking bandwidth increases as well. For the controller with full four modes approximation, the tracking error demonstrates smooth and small variations in the entire frequency range. Hence, it can be concluded that for a real rod-type actuator with infinite modes, the tracking bandwidth of the proposed controller dependents on the number of included modes. For any desired bandwidth, accurate tracking can be guaranteed provided that all the modes up to the frequency of interest have been included in the controller.

There are, however, small peaks within the covered frequencies due to the truncation of higher modes. These peaks can be flattened by increasing the control gains. This has been demonstrated in Figure 5.12, where the error level as well as its small unwanted peak at around 20 kHz has been attenuated by choosing larger control gains. In general, for a plant with uncertainties, larger control gains lead to lower tracking error amplitude. The most limiting factor in practice could be the chatter phenomenon for the controllers with very large gain values.

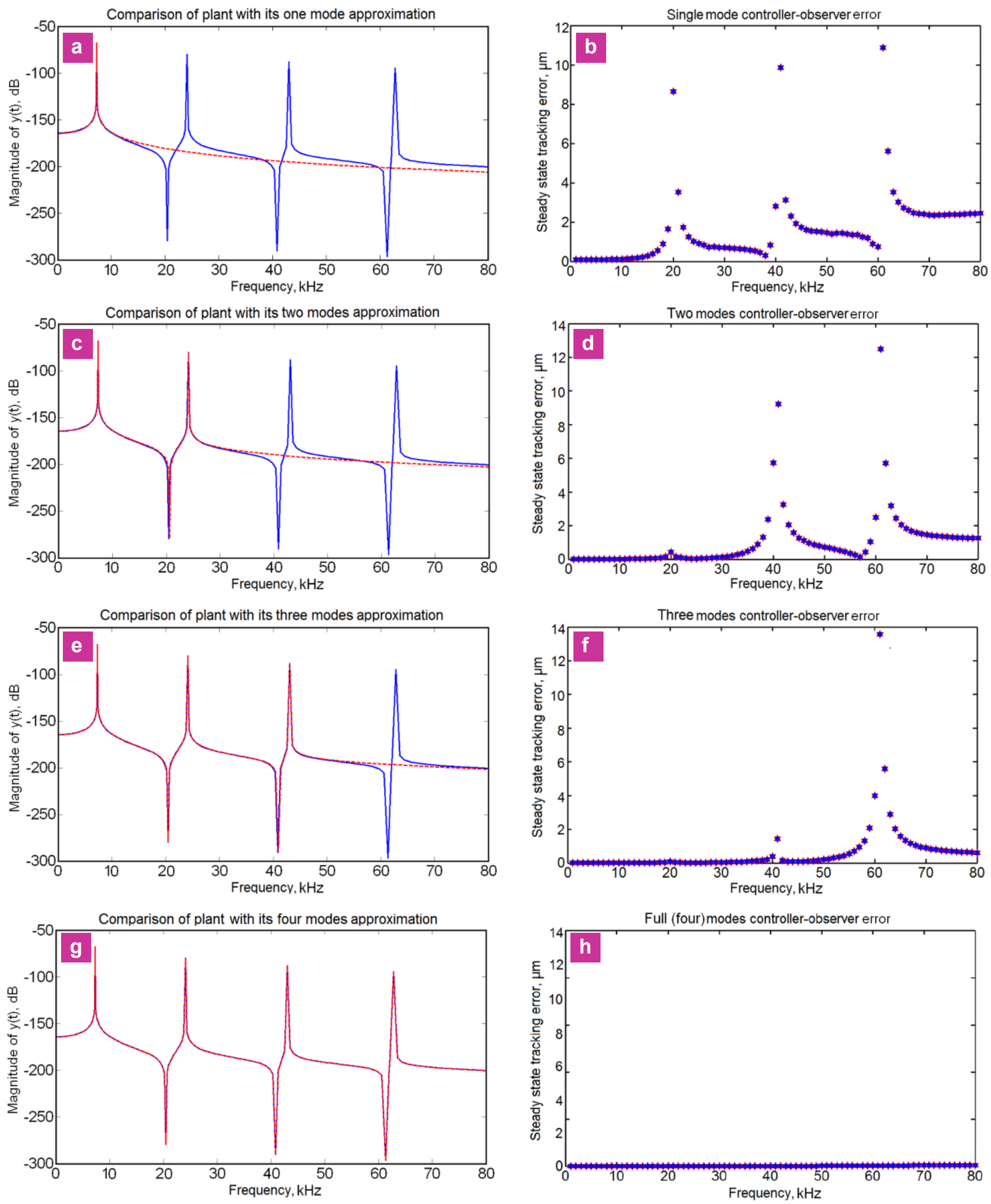

Figure 5.11. Different approximations and tracking control results for a 4-mode plant model. (a), (b) 1 mode, (c), (d) 2 modes, (e), (f), 3 modes and (g), (h) 4 (full) modes approximations and tracking control results.

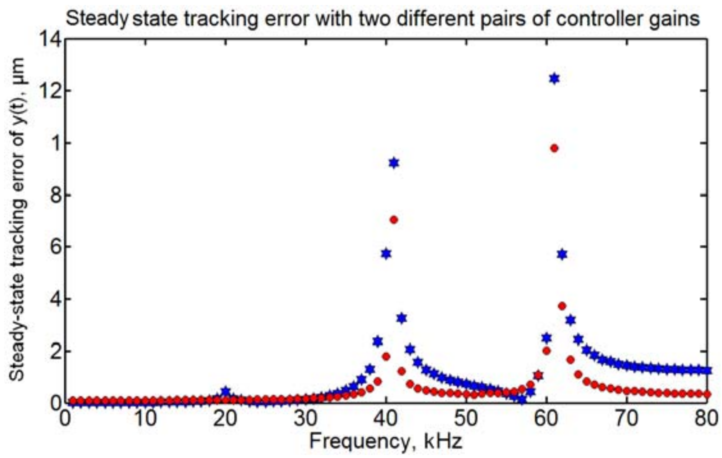

Figure 5.12. Steady-state tracking error comparisons for two sets of gains for controller/observer based on two modes approximation (data with the circle legend correspond to the controller with larger gain values).

5.9. Robust Tracking Control

Uncertainties are unavoidable in practice. The effects of neglected and unmodeled dynamics, external disturbances, system nonlinearities, parametric uncertainties and the environmental changes would affect the closed-loop system performance. Hence, the controller must be made robust with respect to these effects to result is high-performance tracking. In this section, a Lyapunov-based robust variable structure control is developed for the present state-space system to reduce the degrading effects of uncertainties on the system performance. Variable structure (sliding mode) control has been widely used in variety of control applications since its invention [71]. Here, its continuous-time state-space formulation is presented for the proposed rode-like actuator model.

The modified state-space equations of system by including a disturbance terms is given by:

$$\begin{aligned} \dot{x}(t) &= \mathbf{A}x(t) + \mathbf{B}u(t) + \mathbf{G}d(t) \\ y(t) &= \mathbf{C}x(t) \end{aligned} \tag{5.40}$$

where $\boldsymbol{G}_{2k\times 1}$ is the disturbance matrix and $d(t)$ is a bounded time-varying term representing the collective effects of disturbances on the system. The objective of robust control is to force the system output to track desired trajectories despite the effects of unknown disturbances on the system. The first order time derivative of Eq. (5.31) for the system described by Eq. (5.40) becomes:

$$\begin{aligned} \dot{e}(t) &= \dot{y}_d(t) - \dot{y}(t) \\ &= \dot{y}_d(t) - \mathbf{C}\dot{x}(t) \\ &= \dot{y}_d(t) - \mathbf{CA}x(t) - \mathbf{CB}u(t) - \mathbf{CG}d(t) \end{aligned} \tag{5.41}$$

As discussed earlier, term ***CB*** becomes zero for the present system. Therefore, the first order state-space controller cannot be used for the tracking of actuator tip displacement. It can also be shown that the term ***CG*** becomes zero in many cases such as the presence of parametric uncertainties and external disturbances. However, to develop a more general strategy, we assume a nonzero value for this term. The second order time derivative of the tracking error represented in Eq. (5.41) is then given by:

$$\ddot{e}(t) = \ddot{y}_d(t) - \mathbf{CA}^2x(t) - \mathbf{CAB}u(t) - \mathbf{CAG}d(t) - \mathbf{CG}\dot{d}(t) \tag{5.42}$$

To achieve both robustness and tracking control of system simultaneously, the sliding manifold is defined as:

$$s(t) = \dot{e}(t) + \sigma\, e(t) \tag{5.43}$$

with σ being a positive constant representing the slope of the sliding line. Now, consider the following control law:

$$u(t) = \{\mathbf{CAB}\}^{-1}\left(\ddot{y}_d(t) - \mathbf{CA}^2 x(t) + \sigma\dot{e}(t) + \eta_1 s(t) + \eta_2\,\mathrm{sgn}\left(s(t)\right)\right);\ 0 < \eta_1,\, \eta_2 \tag{5.44}$$

where η_1 and η_2 are the control gains, and η_2 satisfies the robustness condition given by:

$$\left\|\mathbf{CG}\dot{d}(t) + \mathbf{CAG}d(t)\right\| \le \eta_2 \tag{5.45}$$

which requires $\mathbf{CG}\dot{d}(t)$ to be bounded, meaning either ***CG*** is zero or $d\,(t)$ is one time continuously differentiable.

Theorem 5.2. For the plant given by Eq. (5.40), the control law (5.44) guarantees the asymptotic convergence of sliding trajectory $s(t)$, tracking error $e(t)$, and its time derivative $\dot{e}(t)$, i.e., $s(t), e(t), \dot{e}(t) \to 0$ as $t \to \infty$, in the sense that all signals are bounded.

Proof: Substitution of the control law (5.44) into the second order error dynamics, Eq. (5.42), yields:

$$\ddot{e}(t) + \sigma\dot{e}(t) + \eta_1 s(t) + \eta_2\,\mathrm{sgn}\left(s(t)\right) + \mathbf{CAG}d(t) + \mathbf{CG}\dot{d}(t) = 0 \tag{5.46}$$

We now define a positive definite Lyapunov function V as:

$$V = \frac{1}{2}s^2(t) \tag{5.47}$$

Its first order time derivative is obtained as:

$$\dot{V}(t) = s(t)\dot{s}(t) = s(t)\left(\ddot{e}(t) + \sigma\dot{e}(t)\right) \tag{5.48}$$

Substituting the second order time derivative of tracking error from Eq. (5.46) into Eq. (5.48) yields:

$$\begin{aligned}\dot{V}(t) &= -\eta_1 s^2(t) - \eta_2 s(t)\,\mathrm{sgn}\left(s(t)\right) - \left(\mathbf{CAG}d(t) + \mathbf{CG}\dot{d}(t)\right)s(t) \\ &= -\eta_1 s^2(t) - \eta_2 \left|s(t)\right| - \left(\mathbf{CAG}d(t) + \mathbf{CG}\dot{d}(t)\right)s(t)\end{aligned} \tag{5.49}$$

If the controller gains are chosen in such a way that the robustness condition given by Eq. (5.40) is satisfied, then the time derivative of the Lyapunov function given by Eq. (5.49) results in:

$$\dot{V}(t) \le -\eta_1 s^2(t) \le 0 \tag{5.50}$$

This ensures the asymptotic convergence of $s(t)$ yielding asymptotic convergence of $e(t)$ and $\dot{e}(t)$ as well.

It is well known that the sliding trajectory $s(t)$ of the sliding mode control has finite-time convergence property. That is, after a finite time, the sliding trajectory intersects with the sliding line corresponding to $\dot{e}(t) + \sigma e(t) = 0$, and slides along it towards the origin. In the reaching phase, there is a smooth transition of the sliding trajectory toward the sliding line; however, in the sliding phase, where the input switches between two values with infinite frequency, system suffers from the chatter effect. Chatter has been recognized to derive the system to instability in practice and needs to be reduced or eliminated. One of the widely-used methods to reduce the chatter is to replace the hard-switching *signum* function in the control law with a soft switching *saturation* function as:

$$u(t) = \left\{\mathbf{CAB}\right\}^{-1}\left(\ddot{y}_d(t) - \mathbf{CA}^2 x(t) + \sigma\dot{e}(t) + \eta_1 s(t) + \eta_2 \mathrm{sat}\left(s(t)/\varepsilon\right)\right) \tag{5.51}$$

where $\varepsilon > 0$ is a small parameter determining the switching rate of the saturation function defined as:

$$\text{sat}\left(s/\varepsilon\right) = \begin{cases} s/\varepsilon\,; & |s| < \varepsilon \\ \text{sgn}(s); & |s| \geq \varepsilon \end{cases} \tag{5.52}$$

Utilizing the proposed modification, the chatter effect can be eliminated; accordingly, the asymptotic convergence property of the controller is degraded as well. However, a globally uniformly ultimately bounded response is achieved with the steady-state error amplitude being bounded by a combination of control gains given by [72]:

$$\left|e_{ss}(t)\right| \leq \frac{\eta_2 \varepsilon}{\sigma(\eta_1 \varepsilon + \eta_2)} \tag{5.53}$$

The smaller the ε is chosen the smaller becomes the error amplitude, and the more likely chatter occures in practice. There should be a tradeoff between the chatter and the tracking performance to effectively tune this parameter.

Two simulations are performed here to demonstrate the performance of the proposed variable structure controller with both signum and saturation functions. The nominal parameters for the controller are perturbed by 5% from the actual plant parameters to induce uncertainties in the closed-loops system. Figure 5.13 demonstrates the tracking results for a 5 μm amplitude desired trajectory with frequency of 50 kHz. Both controllers are able to effectively track the desired trajectory. The control input of the sliding mode control with the signum function demonstrates the chatter effect in the sliding phase (Figure 5.13-b,) while this effect is not seen in Figure 5.13-d where the saturation function is used. Figure 5.14 demonstrates the phase portrait of the controllers, in which both portraits demonstrate similar responses with differences being the small error cycles around the origin but removal of the chatter effect using the soft switching controller.

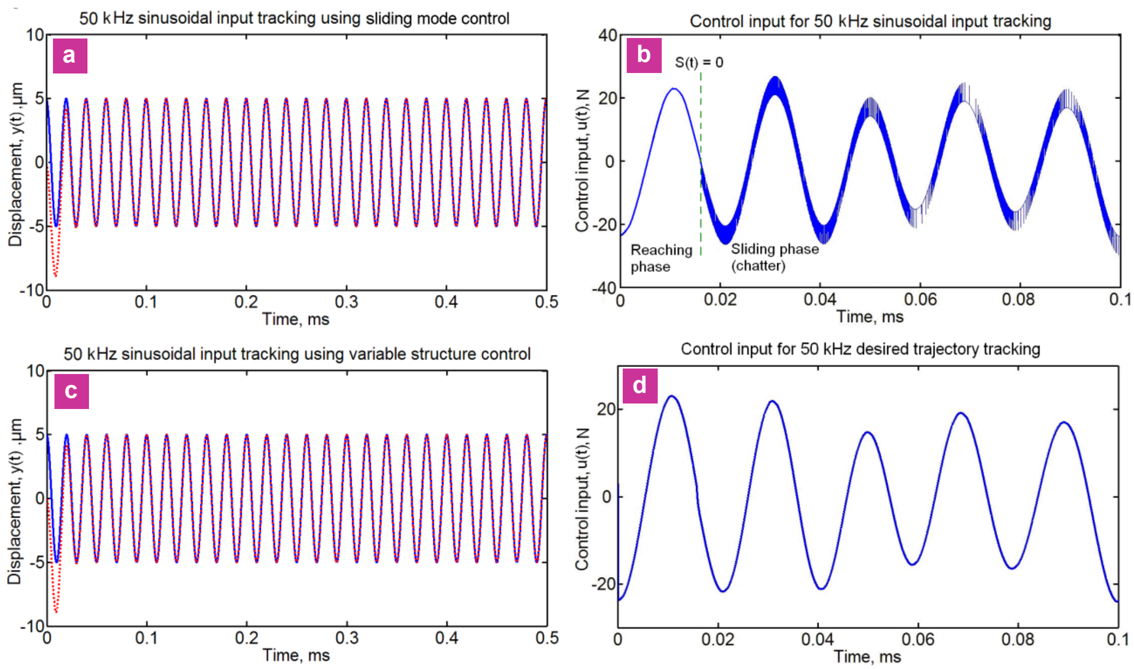

Figure 5.13. Robust tracking control of 50 kHz desired trajectory using sliding mode control: (a) tracking and (b) control input; and using soft-switching mode control: (c) tracking and (d) control input.

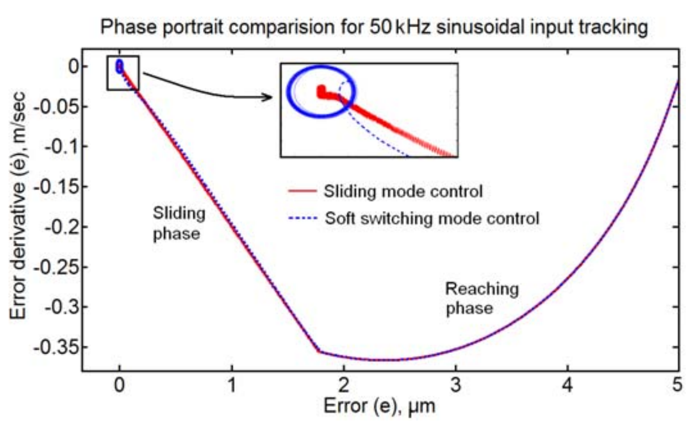

Figure 5.14. Phase portrait comparison of sliding mode and soft switching mode variable structure controllers.

Chapter Summary

A state-space representation has been proposed for multiple-mode modeling and high bandwidth tracking control of rod-type solid-state actuators. Using the extended Hamilton's principle, partial differential equation of motion and the associated boundary conditions were derived. Standard vibration analysis techniques were carried out for the modal and forced motion analyses of system to obtain truncated finite-mode state-space representation. A novel control law was proposed for asymptotic output tracking of system. The control law, however, requires full state feedback which is not available in practice. To avoid this problem and ensure practicability of the proposed control framework, design and integration of an optimal state-observer was proposed. Numerical simulations were provided for trajectories with different frequencies. It was demonstrated that the controller/observer pair can effectively suppress the initial tracking error and maintain a low amplitude response for its steady-state phase. Moreover, it was shown that to achieve a higher control bandwidth, more number of system modes must be included in the controller. Eventually, a Lyapunov-based variable structure controller was derived for the robust output tracking of state-space system in the presence of bounded disturbances. Simulation results indicated effective tracking control of a rod-type actuator model with 5% parametric uncertainties. The present framework is expected to attract considerable attention in control of rod-type solid-state actuators with moving to next generation digital signal processing systems with ultra-high frequency sampling rates.

CHAPTER SIX

MODELING AND VIBRATION ANALYSIS OF NANOMECHANICAL CANTILEVER ACTIVE PROBES FOR ULTRA-SMALL MASS DETECTION*

6.1. Introduction

Nanomechanical cantilever (NMC) beams with their structural flexibility, sensitivity to atomic and molecular forces, and ultra-fast responsiveness have recently attracted widespread attention in variety of applications including atomic force and friction microscopy [75-78], biomass sensing [79-84], thermal scanning microscopy [85-90], and MEMS switches [91, 92]. For instance, in the Atomic Force Microscopy (AFM), the NMC oscillates at or near its resonant frequency. The shift in the natural frequency due to the tip-sample interaction is used to quantitatively characterize the topography of the surface [75 and 93]. In the biosensing applications, the NMC surface is functionalized to adsorb desired biological species which induce surface stress on the NMC. In this application, the added mass of species is estimated from the shift in the resonant frequency of the system away from that of the original NMC [94, 95].

In recent years, a new generation of NMC beams so-called "Active Probes" have been developed for AFM imaging [9, 10] and received great attention due to their unique design (see Figure 6.1). Typically, an Active Probe can be used as an actuator, sensor and actuator-sensor, simultaneously. When it is used as an actuator, it offers broader actuation

* The contents of this chapter may have come directly or indirectly from our joint publications [73, 74].

bandwidth than that of conventional piezotube [96]. This advantage of Active Probes over commonly used bulky piezotube actuators makes them promising candidates to be utilized in high speed imaging AFM. On the other hand, when Active Probes are used for sensing, they offer the sensitivity as much magnitude as of optical sensors [10]. This way, they can be used as alternative sensors for the bulky laser system in AFM which show some disadvantages in terms of laser alignment in the liquid environment, laser expense, and space required for the laser operation. Additionally, it has recently been shown that utilizing a self-sensing strategy, it is possible to use Active Probes for ultra small tip mass and gas detection purpose [97, 98].

Typically, an Active Probe is covered by a piezoelectric layer on the top surface. This layer is utilized as a potential source of actuation, or as an alternative transduction for the laser interferometer in the next-generation laser-free AFMs. In typical configuration of Active Probe, body of the NMC is designed wider due to the presence of piezoelectric layer, while the tip zone is made narrower in order to improve tip deflection measurement. Hence, the NMC has two steps in the cross-section; one small step where the piezoelectric layer ends, and one larger step where the NMC cross-sectional area decreases suddenly. These discontinuities can significantly affect the modal characteristics of the system, and consequently the level of measurement precision in different scenarios. For example, when piezoelectric layer is used as a sensor, the generated voltage can be utilized to detect the vertical deflection of NMC. In this case, the magnitude of output voltage is proportional to the slope difference of the deflection at two ends of the attached piezoelectric layer [34, 99]. This voltage can be expressed in terms of NMC mode shapes and generalized coordinates. On the other hand, if the piezoelectric layer is used as a source of actuation, the modal frequency response of the system depends on the mode shapes as well. Along this line of reasoning, developing an accurate dynamic model for NMCs with jump discontinuities in cross-section is important and can have significant impact on sensing and imaging enhancement of NMC Active Probes.

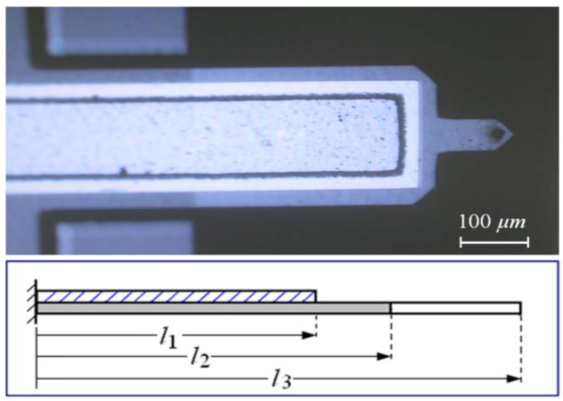

Figure 6.1. Piezoelectrically-driven NMC beam with cross-sectional discontinuity.

The present study is aimed at acquiring a precise model for modal characterization and dynamic analysis of the aforementioned NMC Active Probes with geometrical discontinuities. To this end, we have developed a framework for modeling and analysis of Euler-Bernoulli beams with cross-sectional discontinuities. The entire length of NMC is divided into three uniform segments consisting of a composite beam with the piezoelectric layer and two segments of simple beams with different cross-sectional areas. The governing equation of motion is consequently divided into three partial differential equations with two sets of continuity conditions applied to the points of discontinuity. The eigenvalue problem associated with the cantilever configuration is then solved to obtain NMC mode shapes and natural frequencies. The induced electromechanical stress in the piezoelectric layer is replaced with a concentrated moment at the free end of attachment. Moreover, applying the expansion theorem and method of assumed modes, the governing equations reduce to ordinary differential equations to arrive at the state-space representation of the system. Results from the proposed model are compared with those obtained from experiment and commonly used theory for the uniform beams. It is clearly demonstrated that the proposed model provides good agreement with the experimental results. Furthermore, it is shown that assuming uniform geometry and configuration for the dynamic analysis of the current NMC Active Probes is not a valid strategy since it creates significant error in measurements.

6.2. Experimental Setup and Procedure

In this section, a commercial NMC Active Probe, the DMASP manufactured by Veeco Instruments Inc., is used to study the dynamic response of the probe. For this purpose, an experimental set-up is built using a state-of-the-art microsystem analyzer, the MSA-400 manufactured by Polytec Inc. MSA-400 employs the laser Doppler vibrometry and stroboscopic video microscopy to measure the 3D dynamic response of MEMS and NEMS (see Figure 6.2). It features picometer displacement resolution for out-of-plane measurement, as well as measures frequencies as high as 20 MHz.

The NMC, shown in Figure 6.3(a), is covered by a piezoelectric layer containing a stack of 0.25 μm Ti/Au, 3.5 μm ZnO, and 0.25 μm Ti/Au. The Ti/Au layers on the top and beneath ZnO layer act as electrodes which, along with the silicon cantilever, construct a bimorph actuator. As the input voltage is applied to the pads at the fixed end of the beam, the expansion and contraction of the ZnO layer results in the transversal vibration of the NMC.

The NMC assembled on a chip is mounted on a *XYZ* stage to be adjusted within the laser light focus for measuring beam motion (Figure 6.3(b)). Using an optical microscope, the desired points on the surface of NMC are precisely chosen to be scanned. When the electrical signals are applied to the system, the laser Doppler vibrometer measures the beam velocity at any given points through collecting and processing of backscattered laser light. In this study, a 10 Volt AC chirp signal with 500 kHz bandwidth is applied to the piezoelectric layer as the source of excitation.

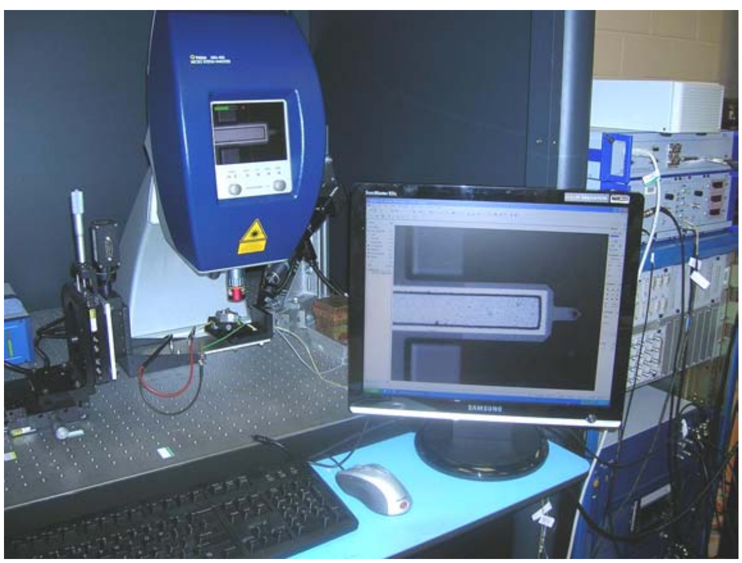

Figure 6.2. Experimental setup for NMC characterization under Micro System Analyzer (MSA-400) at Clemson University SSNEMS Laboratory.

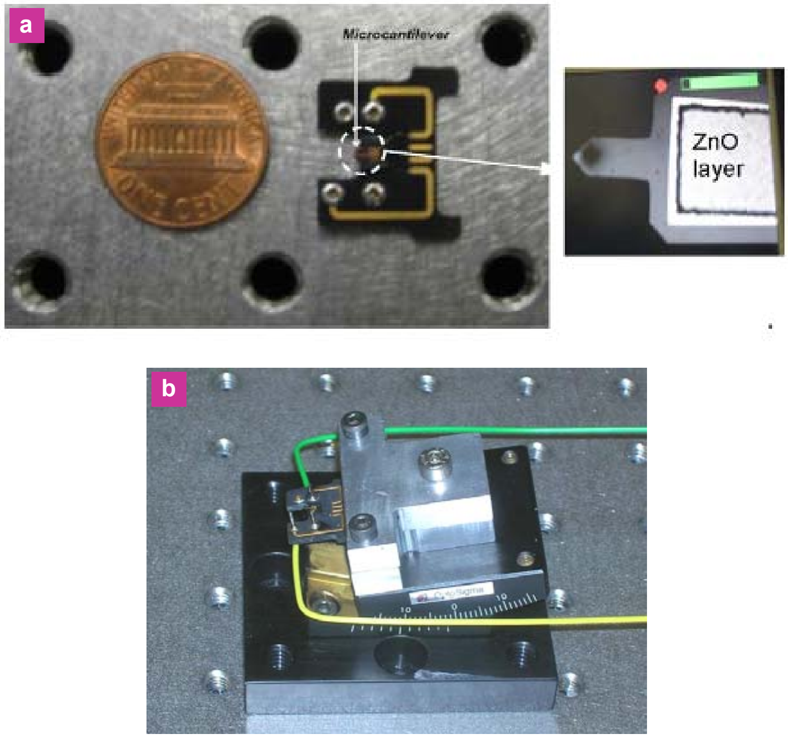

Figure 6.3. (a) Comparison of the Veeco DMASP NMC beam size with a US penny, (b) *XYZ* microstage for adjusting laser light reflecting form NMC tip.

Figure 6.4 demonstrates modal frequency response of the NMC. As seen, the first three resonant frequencies of the probe are located within the applied frequency bandwidth with the values of 52.3, 203.0, and 382.5 kHz, respectively. Furthermore, the corresponding mode shapes of Active Probe are obtained by exciting the system in its resonant frequencies as depicted in Figure 6.5.

In the following section, a dynamic model is developed for the NMC Active Probe taking into account system discontinuities for precise modal analysis. Results will be compared with those obtained from a uniform beam theory for the validation of the proposed modeling framework.

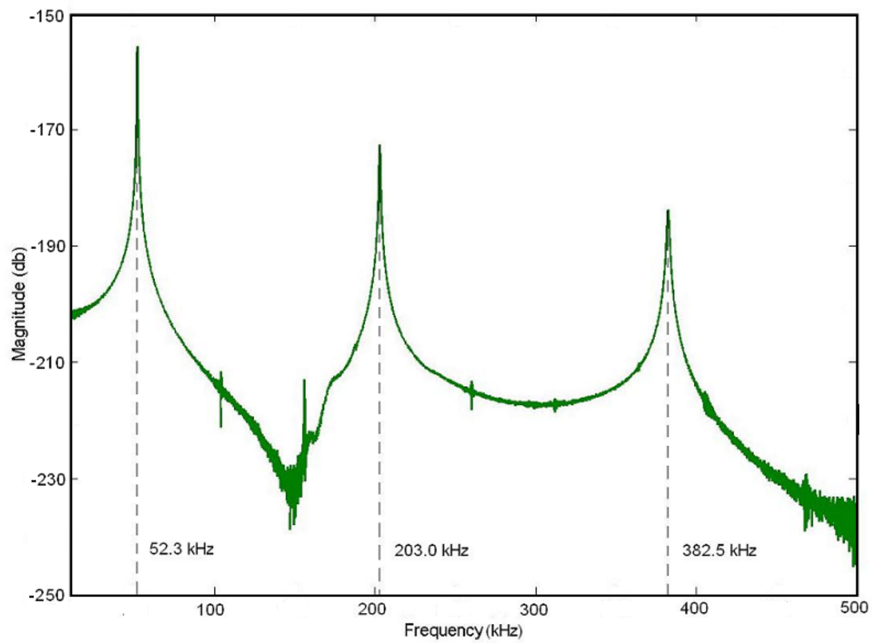

Figure 6.4. Modal frequency response of NMC Active Probes tip transversal vibration.

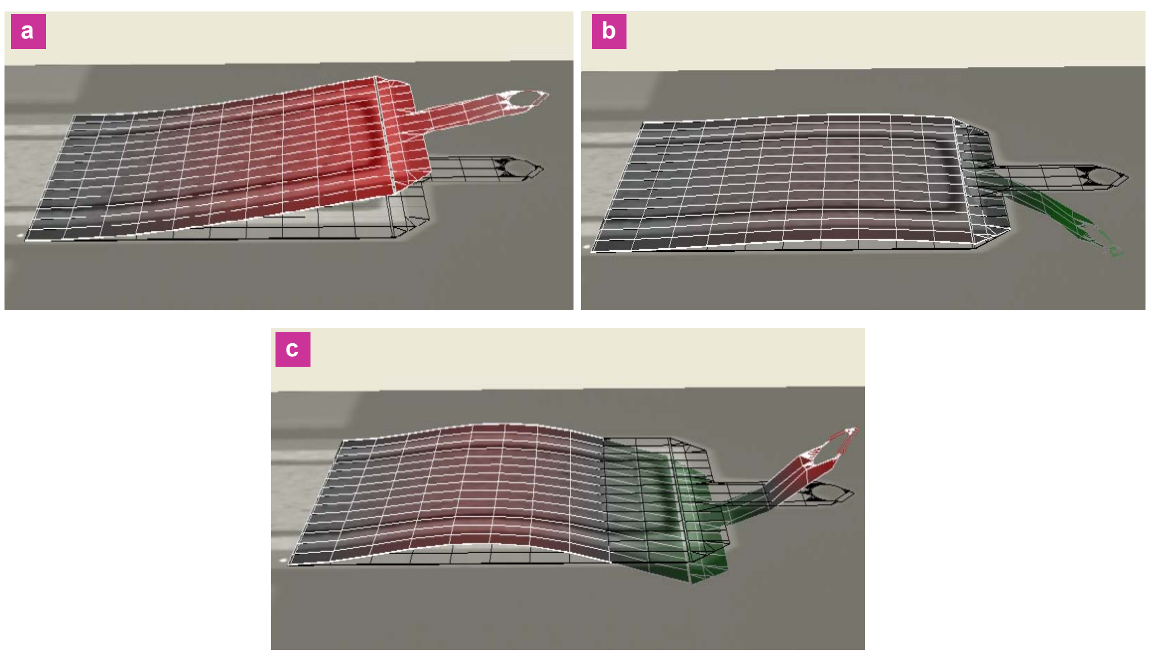

Figure 6.5. 3D motion of NMC at; (*a*) first, (*b*) second, and (*c*) third resonant frequency (only motion of the right most portion of the NMC shown in girds has been measured and animated experimentally).

6.3. Development of a Dynamic Model for NMC Active Probes

Consider a piezoelectrically-driven discontinuous NMC beam with its geometrical parameters depicted in Figure 6.6. The piezoelectric layer is assumed to be a mechanical part of the structure which can induce an electromechanical stress as a result of the applied voltage. This stress can then be replaced with an equivalent moment for the forced vibration analysis of the system. In this respect, the piezoelectric constitutive equations, assuming one dimensional deformation for the piezoelectric layer, can be expressed as [34]:

$$\sigma_x^p = E_p \varepsilon_x^p - E_p d_{31} \frac{v(t)}{t_p} \tag{6.1}$$

where σ_x^p, ε_x^p and E_p are the induced stress, mechanical strain, and the Young's modulus of the piezoelectric layer, respectively; d_{31} is the coefficient of the converse piezoelectric effect, t_p is the piezoelectric layer thickness depicted in Figure 6.6, and $v(t)$ is the applied voltage. Eq. (6.1) demonstrates that the corresponding induced stress can be divided into a passive and an active term. The passive term (the first term in the right hand side of Eq. 6.1) is treated as the internal energy of layer, while the active term (the second expression) is the source of electromechanical excitation which is considered as the external energy. Taking the active part of Eq. (6.1), the equivalent cross-sectional electromechanical moment acting at distance x from the clamped end of the NMC can be expressed as [34]:

$$M_p(x,t) = -\int \left(\sigma_x^p\right)_a y dA = -\int_{t_b/2}^{t_p+t_b/2} \left(\sigma_x^p\right)_a w_p y dy = \frac{1}{2} w_p E_p d_{31}(t_b + t_p) v(t), \quad 0 < x < l_1 \quad (6.2)$$

where $\left(\sigma_x^p\right)_a = -E_p d_{31} \, v(t) / t_p$ is the active induced stress. Eq. (6.2) can be extended to the entire length of the cantilever by multiplying a Heaviside function as follows:

$$M_p(x,t) = \frac{1}{2} w_p E_p d_{31}(t_b + t_p) v(t) S(x) = M_{p0}(t) S(x), \quad 0 < x < L \quad (6.3)$$

with $S(x) = 1 - H(x - l_1)$ and $H(x)$ being the unit Heaviside (Step) function.

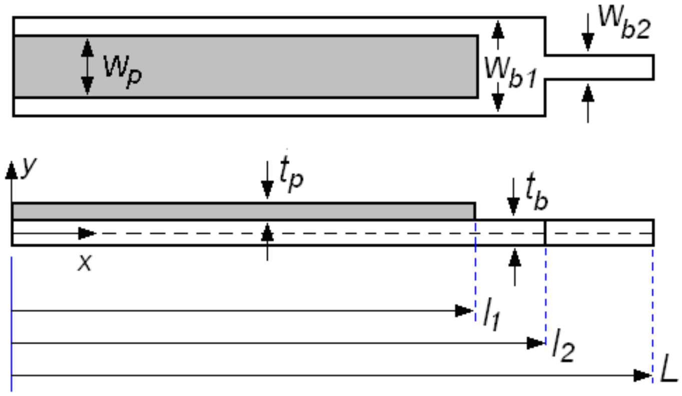

Figure 6.6. Schematic representation of NMC with an attached piezoelectric layer on its top surface.

Eq. (6.3) implies that the cross-sectional moment induced by the piezoelectric excitation can be replaced by a concentrate external moment ($M_{p0}(t)$) acting at the free end of piezoelectric layer, as demonstrated in Figure 6.7. Once the electromechanical excitation is pulled out from the mechanical structure, the problem is reduced to carry out the vibration analysis of a discontinuous beam under an external concentrate moment applied at the free end of the piezoelectric layer.

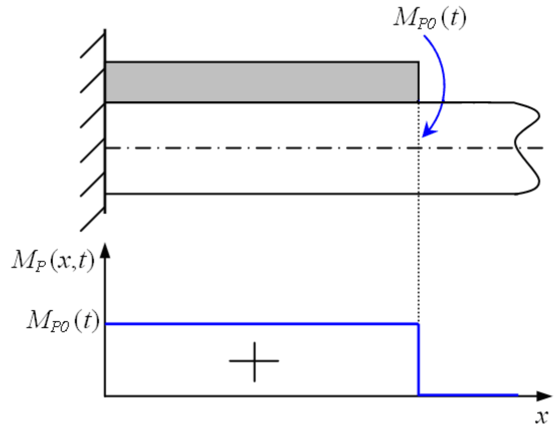

Figure 6.7. Equivalent electromechanical moment due to piezoelectric excitation (top), and uniform distribution of internal moment along the NMC length (bottom).

For the current configuration of Active Probe with the high length to thickness ratio (around 100) and small transversal deflection, assuming the Euler-Bernoulli conditions can be a valid strategy. The governing equation of motion for the beam with variable parameters under the distributed cross-sectional moment, $M_p(x,t)$, is given by:

$$\frac{\partial^2}{\partial x^2}\left(E(x)I(x)\frac{\partial^2 w}{\partial x^2}\right)+c(x)\frac{\partial w}{\partial t}+m(x)\frac{\partial^2 w}{\partial t^2}=\frac{\partial^2 M_p(x,t)}{\partial x^2} \tag{6.4}$$

where $c(x)$, $m(x)$, $E(x)$, and $I(x)$ are variable damping coefficient, mass per unit length, stiffness and moment of inertia, respectively. More especially, for the present Active Probe we have:

$$E(x)I(x)=\begin{cases}(EI)_1=E_b\left(I_p+I_{b1}\right), & 0<x\le l_1\\ (EI)_2=E_bI_{b1}, & l_1<x\le l_2\\ (EI)_3=E_bI_{b2}, & l_2<x\le L\end{cases} \tag{6.5}$$

where:

$$
\begin{aligned}
&I_p = y_n^2\left(t_b w_{b1} + \eta t_p w_p\right) + \eta w_p\left[\frac{1}{3}t_p^3 + \frac{1}{2}t_b t_p^2 + \frac{1}{4}t_b^2 t_p - \left(t_p^2 + t_b t_p\right)y_n\right] \\
&I_{b1} = \frac{w_{b1}t_b^3}{12}, \quad I_{b2} = \frac{w_{b2}t_b^3}{12}; \qquad y_n = \frac{E_p t_p w_p (t_p + t_b)}{2\left(E_p t_p w_p + E_b t_b w_{b1}\right)}, \quad \eta = \frac{E_p}{E_b}
\end{aligned}
\tag{6.6}
$$

and

$$
m(x) = \begin{cases} m_1 = \rho_p w_p t_p + \rho_b w_{b1} t_b, & 0 < x \le l_1 \\ m_2 = \rho_b w_{b1} t_b, & l_1 < x \le l_2 \\ m_3 = \rho_b w_{b2} t_b, & l_2 < x \le L \end{cases}
\tag{6.7}
$$

where $y = y_n$ is the neutral axis of the beam on the composite portion, E_b is the Young's modulus of the beam, and ρ_b and ρ_p are the density of the beam and piezoelectric layer, respectively. Moreover, from the experimental frequency response (shown in Figure 6.4), it is observed that the system is lightly damped. Hence, the distribution of damping can be safely assumed to be uniform in the entire length of the cantilever.

Following the modeling framework presented in Appendix (B) for the beams with multiple cross-sectional discontinuities, the system can be presented in the standard state-space form. For this, the characteristics matrix **J** for the present configuration of Active Probe can be formed using Eqs. (B.27)-(B.31) as follows:

$$\mathbf{J}_{12\times 12} = \begin{bmatrix} 0 & 1 & 0 & 1 & 0 & 0 & 0 & 0 & 0 & 0 & 0 & 0 \\ 1 & 0 & 1 & 0 & 0 & 0 & 0 & 0 & 0 & 0 & 0 & 0 \\ \sin\beta l_1 & \cos\beta l_1 & \sinh\beta l_1 & \cosh\beta l_1 & -\sin\alpha_2\beta l_1 & -\cos\alpha_2\beta l_1 & -\sinh\alpha_2\beta l_1 & -\cosh\alpha_2\beta l_1 & 0 & 0 & 0 & 0 \\ \beta\cos\beta l_1 & -\beta\sin\beta l_1 & \beta\cosh\beta l_1 & \beta\sinh\beta l_1 & -\alpha_2\beta\cos\alpha_2\beta l_1 & \alpha_2\beta\sin\alpha_2\beta l_1 & -\alpha_2\beta\cosh\alpha_2\beta l_1 & -\alpha_2\beta\sinh\alpha_2\beta l_1 & 0 & 0 & 0 & 0 \\ -\gamma_1\beta^2\sin\beta l_1 & -\gamma_1\beta^2\cos\beta l_1 & \gamma_1\beta^2\sinh\beta l_1 & \gamma_1\beta^2\cosh\beta l_1 & \alpha_2^2\beta^2\sin\alpha_2\beta l_1 & \alpha_2^2\beta^2\cos\alpha_2\beta l_1 & -\alpha_2^2\beta^2\sinh\alpha_2\beta l_1 & -\alpha_2^2\beta^2\cosh\alpha_2\beta l_1 & 0 & 0 & 0 & 0 \\ -\gamma_1\beta^3\cos\beta l_1 & \gamma_1\beta^3\sin\beta l_1 & \gamma_1\beta^3\cosh\beta l_1 & \gamma_1\beta^3\sinh\beta l_1 & \alpha_2^3\beta^3\cos\alpha_2\beta l_1 & -\alpha_2^3\beta^3\sin\alpha_2\beta l_1 & -\alpha_2^3\beta^3\cosh\alpha_2\beta l_1 & -\alpha_2^3\beta^3\sinh\alpha_2\beta l_1 & 0 & 0 & 0 & 0 \\ 0 & 0 & 0 & 0 & \sin\alpha_2\beta l_2 & \cos\alpha_2\beta l_2 & \sinh\alpha_2\beta l_2 & \cosh\alpha_2\beta l_2 & -\sin\alpha_3\beta l_2 & -\cos\alpha_3\beta l_2 & -\sinh\alpha_3\beta l_2 & -\cosh\alpha_3\beta l_2 \\ 0 & 0 & 0 & 0 & \alpha_2\beta\cos\alpha_2\beta l_2 & -\alpha_2\beta\sin\alpha_2\beta l_2 & \alpha_2\beta\cosh\alpha_2\beta l_2 & \alpha_2\beta\sinh\alpha_2\beta l_2 & -\alpha_3\beta\cos\alpha_3\beta l_2 & \alpha_3\beta\sin\alpha_3\beta l_2 & -\alpha_3\beta\cosh\alpha_3\beta l_2 & -\alpha_3\beta\sinh\alpha_3\beta l_2 \\ 0 & 0 & 0 & 0 & -\gamma_2\alpha_2^2\beta^2\sin\alpha_2\beta l_2 & -\gamma_2\alpha_2^2\beta^2\cos\alpha_2\beta l_2 & \gamma_2\alpha_2^2\beta^2\sinh\alpha_2\beta l_2 & \gamma_2\alpha_2^2\beta^2\cosh\alpha_2\beta l_2 & \alpha_3^2\beta^2\sin\alpha_3\beta l_2 & \alpha_3^2\beta^2\cos\alpha_3\beta l_2 & -\alpha_3^2\beta^2\sinh\alpha_2\beta l_2 & -\alpha_3^2\beta^2\cosh\alpha_3\beta l_2 \\ 0 & 0 & 0 & 0 & -\gamma_2\alpha_2^3\beta^3\cos\alpha_2\beta l_2 & \gamma_2\alpha_2^3\beta^3\sin\alpha_2\beta l_2 & \gamma_2\alpha_2^3\beta^3\cosh\alpha_2\beta l_2 & \gamma_2\alpha_2^3\beta^3\sinh\alpha_2\beta l_2 & \alpha_3^3\beta^3\cos\alpha_3\beta l_2 & -\alpha_3^3\beta^3\sin\alpha_3\beta l_2 & -\alpha_3^3\beta^3\cosh\alpha_3\beta l_2 & -\alpha_3^3\beta^3\sinh\alpha_3\beta l_2 \\ 0 & 0 & 0 & 0 & 0 & 0 & 0 & 0 & -\alpha_3^2\beta^2\sin\alpha_3\beta L & -\alpha_3^2\beta^2\cos\alpha_3\beta L & \alpha_3^2\beta^2\sinh\alpha_3\beta L & \alpha_3^2\beta^2\cosh\alpha_3\beta L \\ 0 & 0 & 0 & 0 & 0 & 0 & 0 & 0 & -\alpha_3^3\beta^3\cos\alpha_3\beta L & \alpha_3^3\beta^3\sin\alpha_3\beta L & \alpha_3^3\beta^3\cosh\alpha_3\beta L & \alpha_3^3\beta^3\sinh\alpha_3\beta L \end{bmatrix} \tag{6.8}$$

Varying parameter β with small steps over a desired range, and finding the zeros of determinant of **J**, leads to determination of the natural frequencies of the beam using Eq. (B.33). The coefficients of the mode shapes can be obtained through Eqs. (B.32) and (B.34). The $(r)^{\text{th}}$ mode shape of the beam can be written as:

$$\phi^{(r)}(x) = \begin{cases} \phi_1^{(r)}(x) = A_1^{(r)}\sin\beta_1^{(r)}x + B_1^{(r)}\cos\beta_1^{(r)}x + C_1^{(r)}\sinh\beta_1^{(r)}x + D_1^{(r)}\cosh\beta_1^{(r)}x, & 0 \le x \le l_1 \\ \phi_2^{(r)}(x) = A_2^{(r)}\sin\beta_2^{(r)}x + B_2^{(r)}\cos\beta_2^{(r)}x + C_2^{(r)}\sinh\beta_2^{(r)}x + D_2^{(r)}\cosh\beta_2^{(r)}x, & l_1 < x \le l_2 \\ \phi_3^{(r)}(x) = A_3^{(r)}\sin\beta_3^{(r)}x + B_3^{(r)}\cos\beta_3^{(r)}x + C_3^{(r)}\sinh\beta_3^{(r)}x + D_3^{(r)}\cosh\beta_3^{(r)}x, & l_2 < x \le L \end{cases} \tag{6.9}$$

To derive the equations of motion, the elements of Eq. (B.46) must be calculated first. Let's assume that the damping coefficient of the beam remains constant for the entire length of beam (i.e. $c(x) = c$). Consequently, this yields:

$$c_{rs} = \int_{l_0}^{l_N} c(x)\phi^{(r)}(x)\phi^{(s)}(x)dx = c\left\{\int_0^{l_1}\phi_1^{(r)}(x)\phi_1^{(s)}(x)dx + \int_{l_1}^{l_2}\phi_2^{(r)}(x)\phi_2^{(s)}(x)dx + \int_{l_2}^{L}\phi_3^{(r)}(x)\phi_3^{(s)}(x)dx\right\} \tag{6.10}$$

Moreover, the input of the NMC Active Probe can be obtained from:

$$f^{(r)}(t) = \int_0^L \frac{\partial^2 M_p(x,t)}{\partial x^2}\phi^{(r)}(x)dx \tag{6.11}$$

Substituting Eq. (6.3) into Eq. (6.11) yields:

$$\begin{aligned} f^{(r)}(t) &= \frac{1}{2}w_p E_p d_{31}(t_b + t_p)v(t)\int_0^L S''(x)\phi^{(r)}(x)dx \\ &= -\frac{1}{2}w_p E_p d_{31}(t_b + t_p)v(t)\int_0^L H''(x - l_1)\phi^{(r)}(x)dx \end{aligned} \tag{6.12}$$

For the second distributional derivative of the Heaviside function we have:

$$\int_0^L H''(x - l_1)\phi^{(r)}(x)dx = \int_0^L \delta'(x - l_1)\phi^{(r)}(x)dx = -\frac{d}{dx}\left(\phi^{(r)}(l_1)\right) \tag{6.13}$$

where $\delta(\cdot)$ represents the Dirac delta function. Substituting Eq. (6.13) into Eq. (6.12) yields:

$$f^{(r)}(t) = \overline{f}^{(r)}v(t) \quad \text{where} \quad \overline{f}^{(r)} = \frac{1}{2}\frac{d}{dx}\left(\phi^{(r)}(l_1)\right)w_p E_p d_{31}(t_b + t_p) \tag{6.14}$$

Thus, the equation of motion and its state-space representation can be formed based on Eqs. (B.43)-(B.48). Once the system is represented in state-space, the frequency response of the system can be plotted to demonstrate the behavior of system within a desired frequency range. Here, the displacement of microcantilever tip at $x = L$ is taken as the system output:

$$\mathbf{Y}(t) = w(L,t) = \sum_{r=1}^{k} \phi^{(r)}(L) q^{(r)}(t) = [\phi^{(1)}(L), \phi^{(2)}(L), ..., \phi^{(k)}(L), 0, ..., 0]_{1\times 2k} \mathbf{X}(t) \qquad (6.15)$$

The standard form of the state-space representation of the system can then be written as:

$$\begin{aligned} \dot{\mathbf{X}} &= \mathbf{AX} + \mathbf{Bu} \\ \mathbf{Y} &= \mathbf{CX} \end{aligned} \qquad (6.16)$$

where

$$\mathbf{C} = [\phi^{(1)}(L), \phi^{(2)}(L), ..., \phi^{(k)}(L), 0, ..., 0]_{1\times 2k} \qquad (6.17)$$

The frequency response of the system can now be plotted using beam's transfer function obtained through the Laplace transformation of its state-space model as follows:

$$G(s) = \frac{Y(s)}{U(s)} = \mathbf{C}(sI - \mathbf{A})^{-1}\mathbf{B} \qquad (6.18)$$

6.4. Experimental Verification

To compare the experimental mode shapes and natural frequencies with those obtained from the proposed model, exact values of system parameters are required. Although some of the parameters are given in the product catalogue, and some others can be measured through precision measurement devices such as our MSA-400, the presence of uncertainties associated with the parameters may drastically degrade model accuracy. Therefore, a system identification procedure is carried out here to fine-tune the parameter values for precise comparison with the experimentally obtained data.

The objective of system identification here is to minimize a constructed error function between the model and the actual system mode shapes and natural frequencies, simultaneously. The optimization variables comprise of NMC parameters and a set of scaling factors. In this regard, a number of points are selected along the NMC for comparison of the mode shapes. The error function utilized for the system identification calculates the percentage of the average weighted error between the measured and evaluated natural frequencies and mode shapes at each selected point for a finite number of modes as follows:

$$E = \frac{1}{K}\left\{ W\sum_{r=1}^{K}\left(\frac{1}{P}\sum_{j=1}^{P}\left| \frac{\mu_r w_{\max}^{(r)E}(x_j) - \phi^{(r)T}(x_j)}{\mu_r w_{\max}^{(r)E}(x_j)} \right| \right) + (1-W)\sum_{r=1}^{K}\left| \frac{\omega_r^E - \omega_r^T}{\omega_r^E} \right| \right\} \times 100 \qquad (6.19)$$

where K is the number of modes, P represents the number of selected points on the NMC length, $0 < W < 1$ is the weighing factor space, $\phi^{(r)T}(x_j)$ stands for the r^{th} theoretical mode shape evaluated at point x_j, $w_{\max}^{(r)E}(x_j)$ indicates the experimental amplitude of point x_j at r^{th} resonant frequency, and μ_r is an scaling optimization variable used to match r^{th} experimental resonant amplitude with the corresponding theoretical mode shape. Other optimization variables including parameters associated with NMC property and geometry (as listed in Table 6.1) are constrained within a limited range around the approximate values. The upper and lower bounds for the variables are selected in accordance with best guesses on the maximum possible amount of uncertainties in the approximate values.

To demonstrate the expected improvements through the proposed modeling framework, both uniform and discontinuous beam models are considered for the system identification. Optimization is carried out by selecting the first three modes of the system ($K = 3$), choosing 16 points on the cantilever length ($P = 16$), and setting the weighing factor $W = 0.5$ to equate the importance between the mode shapes and the resonant frequencies. A random optimization algorithm is then implemented for the parameters estimation using MATLAB programming software. Random optimization is a class of heuristic algorithms which usually converges to the global solution within the search domain [70]. It is expected that the optimization does not converge to a desirable tolerance for the uniform beam model due to large discontinuities of the actual system.

Table 6.1 demonstrates the initial (approximate) values of optimization variables, their imposed upper and lower bounds, and optimal values for the uniform and discontinuous NMC models, respectively. Figure 6.8 depicts the first three mode shapes of the actual NMC beam along with those of the theoretical models. As seen from Figure 8, the mode shapes of the proposed discontinuous model match with the experimental data vary closely when compared to those of the uniform model. Furthermore, the modal frequency responses show more accurate estimation of the system natural frequencies using the discontinuous beam theory (see Figure 6.9). Since the uniform beam assumption fails to accurately model the actual response of the NMC Active Probe for a multiple-mode operation, the discontinuous beam assumptions must be taken into account for the sake of modeling precision.

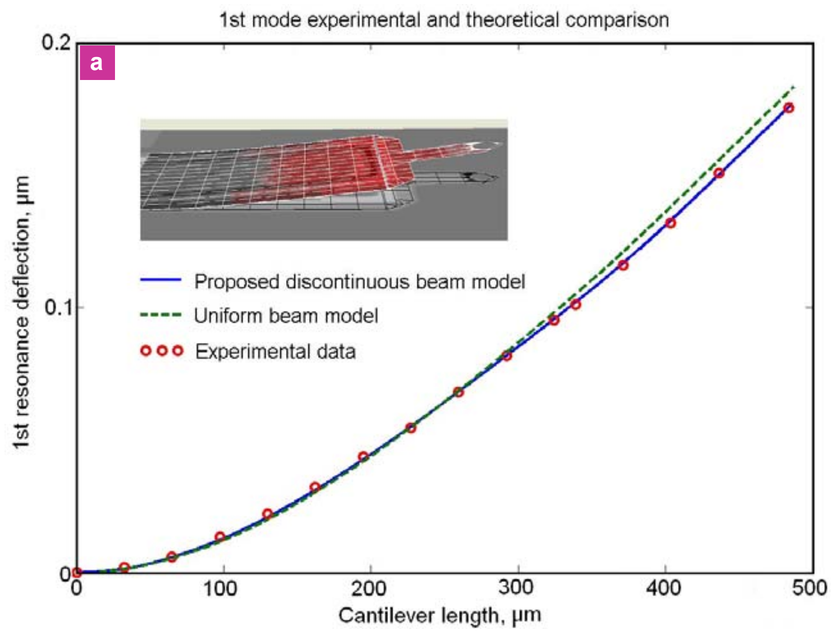

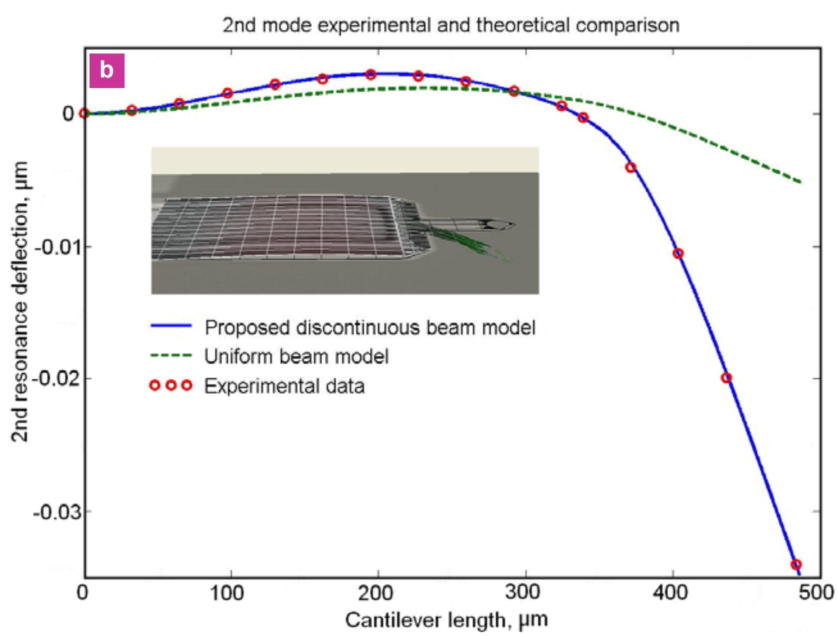

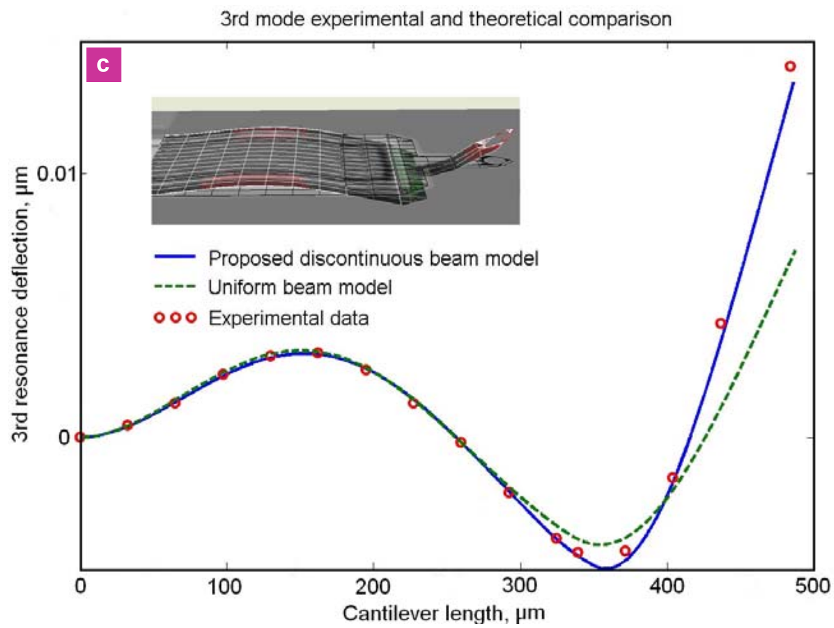

Figure 6.8. Active Probe experimental and theoretical modal comparisons for both uniform and discontinuous beam models: (a)1st , (b) 2nd, and (c) 3rd mode shapes.

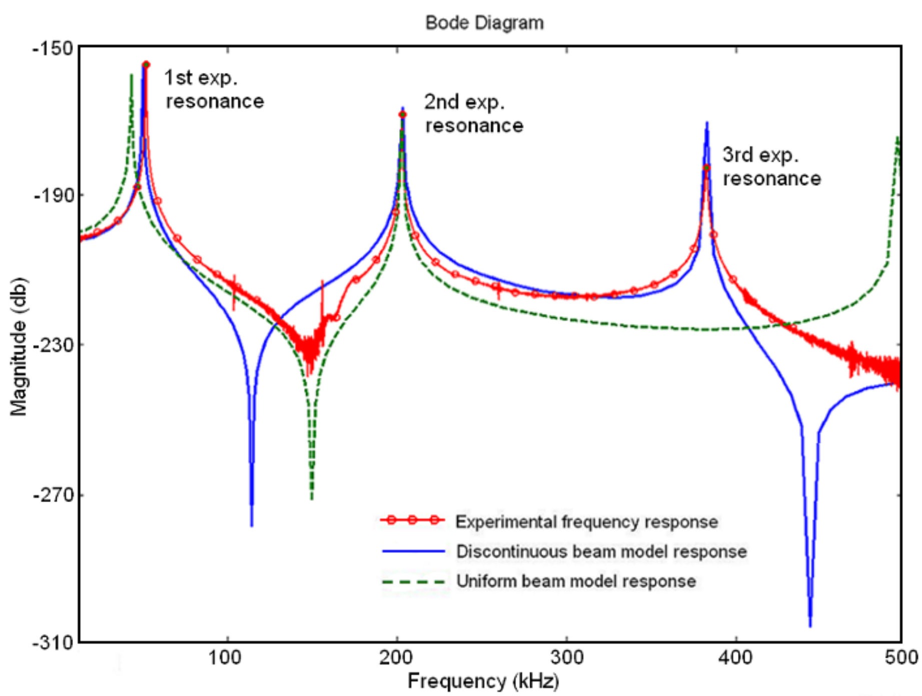

Figure 6.9. Active probe frequency response comparisons (solid line: proposed model, dashed line: uniform model, the circled line: actual response obtained experimentally).

Table 6.1. Independent physical and numerical parameters used in system identification; approximate parameter values, upper and lower bounds, and the optimal solution for uniform and discontinuous NMC beam models.

	Uniform beam model				**Proposed discontinuous beam model**			
Parameters	Lower bound	Upper bound	Initial value	Optimal solution	Lower bound	Upper bound	Initial value	Optimal solution
$L\,(\mu m)$	485	487	486	**486.7**	485	487	486	**485.9**
$L_1\,(\mu m)$	-	-	-	**-**	315	330	325	**315.0**
$L_2\,(\mu m)$	-	-	-	**-**	350	370	360	**350.0**
$m_1(EI)_1^{-1}\left(kg\left(N.m^3\right)^{-1}\right)$	5000	15000	10000	**5294.1**	5000	15000	10000	**7914.5**
$m_2(EI)_2^{-1}\left(kg\left(N.m^3\right)^{-1}\right)$	-	-	-	**-**	10000	30000	20000	**23130.4**
$m_3(EI)_3^{-1}\left(kg\left(N.m^3\right)^{-1}\right)$	-	-	-	**-**	10000	30000	20000	**13461.5**
$(EI)_2(EI)_1^{-1}$	-	-	-	**-**	0.05	0.5	0.25	**0.1966**
$(EI)_3(EI)_2^{-1}$	-	-	-	**-**	0.05	0.5	0.25	**0.2260**
$\mu_1\left(\mu m^{-1}\right)$	0.2	1	0.5	**0.279**	0.2	1	0.5	**0.455**
$\mu_2\left(\mu m^{-1}\right)$	5	20	10	**12.967**	5	20	10	**6.595**
$\mu_3\left(\mu m^{-1}\right)$	5	20	10	**8.5364**	5	20	10	**10.029**

6.5. Application in Ultra Small Mass Detection

The objective of this section is to employ Active Probes for end-loaded (tip) mass detection purposes. To this end, using focused ion beam deposition technique, a small mass in the order of pico-gram is added at the tip of probe. To detect the amount of added mass, this study undertakes the frequency analysis of the system obtained from experiment and theory. Then, the amount of added mass is detected by relating the experimental resonant frequency shifts of system to the amount of added mass.

Small amount of material at defined position and geometry can be deposited by means of focused ion beam (see Figure 6.10), [100]. Here, a FIB (FEI Nova 600, Netherlands) that allows imaging the deposited structures by scanning electron microscopy is utilized. Furthermore, the deposited material can be analyzed by energy-dispersive X-ray spectroscopy (EDX). The NMC cantilever was mounted onto a FIB holder and was grounded by conductive tape to prevent charging of the cantilever during focused ion beam deposition. The FIB chamber was evacuated to a pressure of 10^{-5} mbar. For the deposition of material on the cantilever, the chemical vapor gas injection needle was placed close to the desired area (CVD injection needle). Then, the precursor gas (Methylcyclopentadienyl[Trimethyl]Platinum) was released in the chamber. The precursor gas is decomposed under the Ga^+-ion beam (30 kV, 0.5 nA) on the surface leading to the formation of a material mainly composed of Pt and C (red area in Figure 6.11(b)). EDX revealed a content of 69 % Pt, 15 C, 10 % Ga and 6 % Si. A deposition area of 50 μm by 2 μm was selected. By controlling the ion exposure time (310 seconds), 500 *nm* thick elements were fabricated on the cantilever. Afterwards, the deposited element was imaged by the integrated SEM as shown in Figure 6.11.

Figure 6.12 depicts the first three resonant frequencies of Active Probe before and after mass deposition. It is remarked that a different probe from the one shown in Figure 6.1 has been utilized but with the same configuration. It is seen that these frequencies before mass deposition are 54.257, 222.812, and 380.742 kHz; while after mass deposition they change to 54.218, 220.781, and 380.078 kHz with the maximum shift of 2.031 kHz at the second resonant frequency. Moreover, the sharp peaks in Figure 6.12

indicate that the system is lightly damped, and hence the natural frequencies of the system can be safely considered equal to its resonant frequencies.

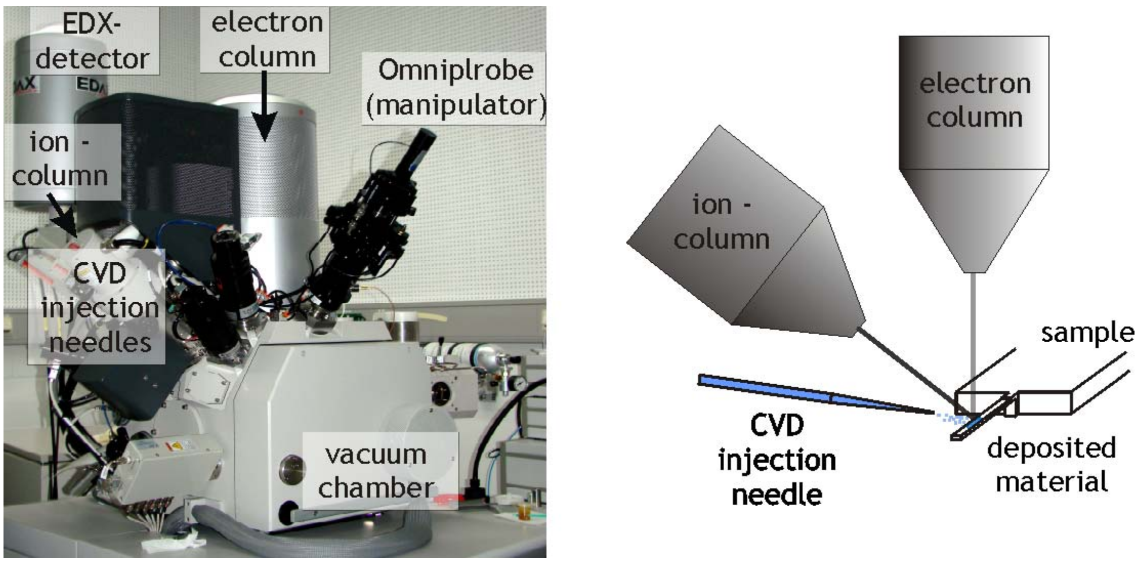

Figure 6.10. Combination of focused ion beam and scanning electron microscopy for the deposition of defined mass on nanomechanical cantilever samples.

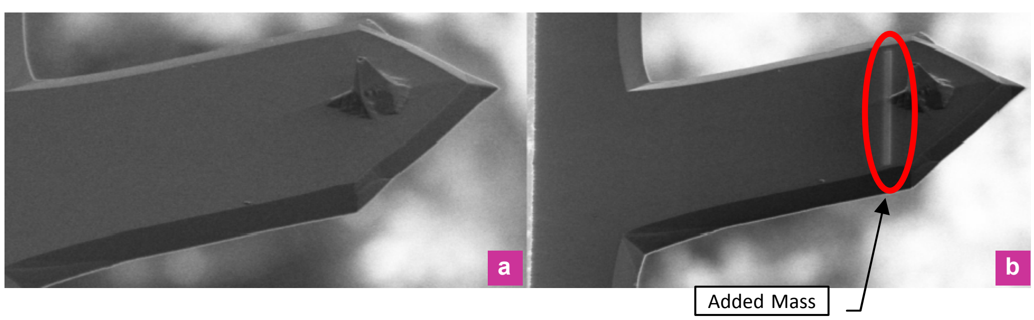

Figure 6.11. Before (a) and after (b) SEM images of Active Probe cantilevers with tip mass added.

Utilizing the proposed NMC cantilever modeling framework, a modification is applied to the system formulation to take into account the effect of tip mass. It can be shown that the orthonormality condition used for obtaining system mode shape coefficients (given by Eq. (B.41)) is modified to:

$$\int_{l_0}^{l_N} m(x)\phi^{(r)}(x)\phi^{(s)}(x)dx + m_e\phi^{(r)}(L)\phi^{(s)}(L) = \delta_{rs} \tag{6.20}$$

And, the characteristics matrix (given by 6.8) is modified to:

$$\mathbf{J}_{12\times 12} = \begin{bmatrix}
0 & 1 & 0 & 1 & 0 & 0 & 0 & 0 & 0 & 0 & 0 & 0 \\
1 & 0 & 1 & 0 & 0 & 0 & 0 & 0 & 0 & 0 & 0 & 0 \\
\sin\beta l_1 & \cos\beta l_1 & \sinh\beta l_1 & \cosh\beta l_1 & -\sin\alpha_2\beta l_1 & -\cos\alpha_2\beta l_1 & -\sinh\alpha_2\beta l_1 & -\cosh\alpha_2\beta l_1 & 0 & 0 & 0 & 0 \\
\cos\beta l_1 & -\sin\beta l_1 & \cosh\beta l_1 & \sinh\beta l_1 & -\alpha_2\cos\alpha_2\beta l_1 & \alpha_2\sin\alpha_2\beta l_1 & -\alpha_2\cosh\alpha_2\beta l_1 & -\alpha_2\sinh\alpha_2\beta l_1 & 0 & 0 & 0 & 0 \\
-\gamma_1\sin\beta l_1 & -\gamma_1\cos\beta l_1 & \gamma_1\sinh\beta l_1 & \gamma_1\cosh\beta l_1 & \alpha_2^2\sin\alpha_2\beta l_1 & \alpha_2^2\cos\alpha_2\beta l_1 & -\alpha_2^2\sinh\alpha_2\beta l_1 & -\alpha_2^2\cosh\alpha_2\beta l_1 & 0 & 0 & 0 & 0 \\
-\gamma_1\cos\beta l_1 & \gamma_1\sin\beta l_1 & \gamma_1\cosh\beta l_1 & \gamma_1\sinh\beta l_1 & \alpha_2^3\cos\alpha_2\beta l_1 & -\alpha_2^3\sin\alpha_2\beta l_1 & -\alpha_2^3\cosh\alpha_2\beta l_1 & -\alpha_2^3\sinh\alpha_2\beta l_1 & 0 & 0 & 0 & 0 \\
0 & 0 & 0 & 0 & \sin\alpha_2\beta l_2 & \cos\alpha_2\beta l_2 & \sinh\alpha_2\beta l_2 & \cosh\alpha_2\beta l_2 & -\sin\alpha_3\beta l_2 & -\cos\alpha_3\beta l_2 & -\sinh\alpha_3\beta l_2 & -\cosh\alpha_3\beta l_2 \\
0 & 0 & 0 & 0 & \alpha_2\cos\alpha_2\beta l_2 & -\alpha_2\sin\alpha_2\beta l_2 & \alpha_2\cosh\alpha_2\beta l_2 & \alpha_2\sinh\alpha_2\beta l_2 & -\alpha_3\cos\alpha_3\beta l_2 & \alpha_3\sin\alpha_3\beta l_2 & -\alpha_3\cosh\alpha_3\beta l_2 & -\alpha_3\sinh\alpha_3\beta l_2 \\
0 & 0 & 0 & 0 & -\gamma_2\alpha_2^2\sin\alpha_2\beta l_2 & -\gamma_2\alpha_2^2\cos\alpha_2\beta l_2 & \gamma_2\alpha_2^2\sinh\alpha_2\beta l_2 & \gamma_2\alpha_2^2\cosh\alpha_2\beta l_2 & \alpha_3^2\sin\alpha_3\beta l_2 & \alpha_3^2\cos\alpha_3\beta l_2 & -\alpha_3^2\sinh\alpha_2\beta l_2 & -\alpha_3^2\cosh\alpha_3\beta l_2 \\
0 & 0 & 0 & 0 & -\gamma_2\alpha_2^3\cos\alpha_2\beta l_2 & \gamma_2\alpha_2^3\sin\alpha_2\beta l_2 & \gamma_2\alpha_2^3\cosh\alpha_2\beta l_2 & \gamma_2\alpha_2^3\sinh\alpha_2\beta l_2 & \alpha_3^3\cos\alpha_3\beta l_2 & -\alpha_3^3\sin\alpha_3\beta l_2 & -\alpha_3^3\cosh\alpha_3\beta l_2 & -\alpha_3^3\sinh\alpha_3\beta l_2 \\
0 & 0 & 0 & 0 & 0 & 0 & 0 & 0 & -\sin\alpha_3\beta L & -\cos\alpha_3\beta L & \sinh\alpha_3\beta L & \cosh\alpha_3\beta L \\
0 & 0 & 0 & 0 & 0 & 0 & 0 & 0 & -\cos\alpha_3\beta L + M_1 & \sin\alpha_3\beta L + M_2 & \cosh\alpha_3\beta L + M_3 & \sinh\alpha_3\beta L + M_4
\end{bmatrix} \tag{6.21}$$

where M_1, M_2, M_3 and M_4 are the boundary conditions associated with the tip mass at the free end of the probe given by

$$\begin{aligned} M_1 &= \frac{m_e}{m_3}\beta\alpha_3 \sin\alpha_3\beta L, \quad M_2 = \frac{m_e}{m_3}\beta\alpha_3 \cos\alpha_3\beta L \\ M_3 &= \frac{m_e}{m_3}\beta\alpha_3 \sinh\alpha_3\beta L, \quad M_4 = \frac{m_e}{m_3}\beta\alpha_3 \cosh\alpha_3\beta L \end{aligned} \tag{6.22}$$

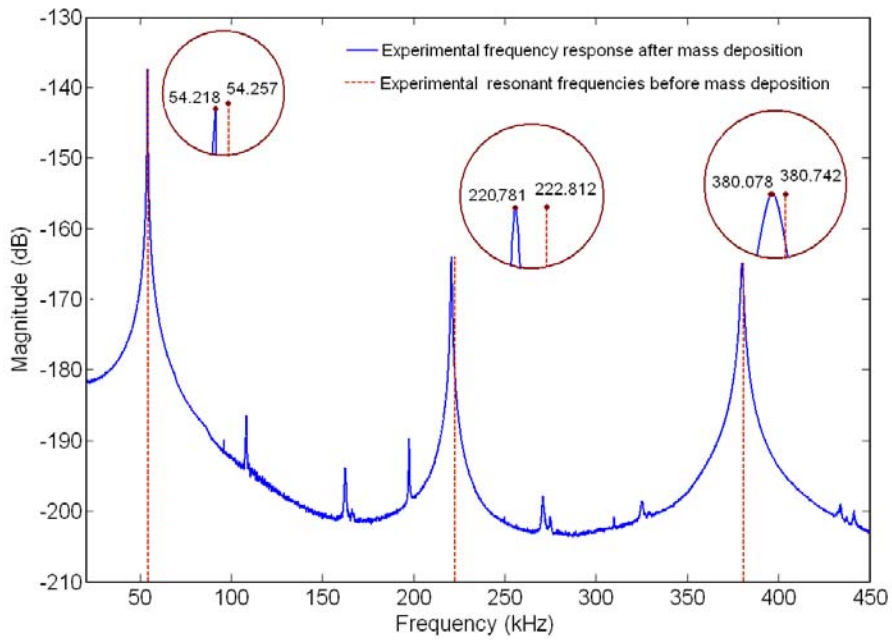

Figure 6.12. Experimental resonant frequency of Active Probes before and after mass deposition.

Having the system with the identified parameters, the shift in the resonant frequencies obtained from theory and experiment can then be utilized to detect the amount of deposit mass. In this respect, the added tip mass can be stated by the gradual increase of the tip mass in the identification procedure such that the theoretical shifts in the resonant frequencies could meet those of experiment. procedure such that the theoretical shifts in the resonant frequencies could meet those of experiment. In an alternative approach, the aforementioned system parameters including an unstated tip mass plus added mass are identified after mass deposition. The added tip mass can then be detected by the gradual decrease of the unstated mass in the identification procedure such that the theoretical shifts in the resonant frequencies could match those of experiment. In this approach, the amount of deposited mass at the end of probe is equal to removal mass in identification procedure.

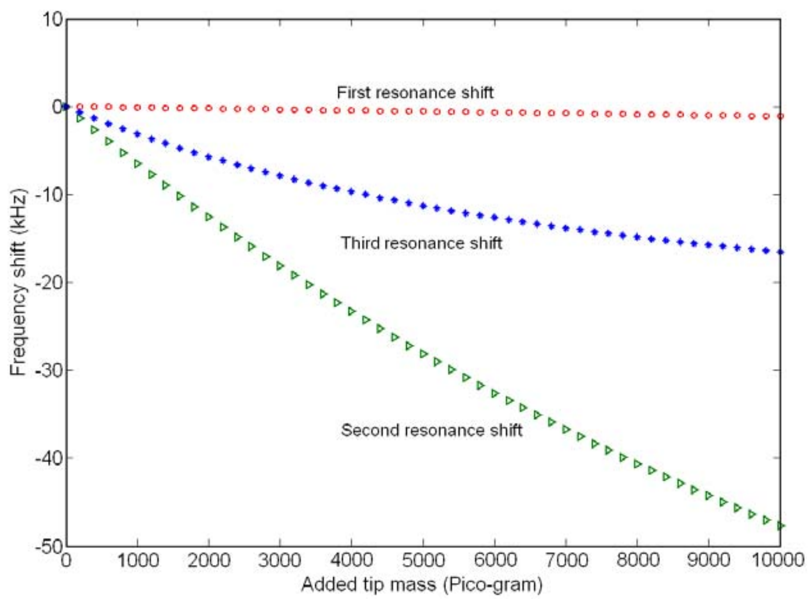

Figure 6.13. Sensitivity of each mode to the added mass.

It is seen that in the second mode of NMC Active Probe, free end of the probe displays much sensitive motion compared to that of its main body. However, in the first and third modes, this sensitivity decreases. Moreover the added mass generates more resonance shift in the second mode compared to the first and the third mode (Figure 6.13 depicts a simulation study of the sensitivity of different modes to the added mass). Hence, the second mode is more reliable to be utilized for estimating the amount of added mass. By means of these considerations and based on the aforementioned procedure, for the 2.031 kHz shift in the second resonant frequency, the amount of added tip mass is estimated to be ***310*** *pico-gram.*

Chapter Summary

Active probes were introduced as advantageous devices for ultra small mass detection due to their embedded piezoelectric actuation capability. A precise vibration model was developed for modal analysis of Active Probe considering the intentional jumped discontinuities associated with the piezoelectric layer and sudden change of cross-section at the tip zone. It was shown that the actual modal displacements of probe had good consistency with those obtained from proposed model. Using focus ion beam technique, an ultra small mass in the order of a few hundred pico-grams was deposited at the free end of Active Probe. A frequency analysis was carried out to measure the amount of the added mass on the probe. It was demonstrated that the second mode is the most sensitive mode to the added mass with its larger frequency shift compared to the other modes.

CHAPTER SEVEN

CONCLUSIONS AND FUTURE WORKS

7.1. Conclusions

Piezoactive systems from the modeling, dynamic analysis and control perspectives were studied in this dissertation. It was shown that hysteresis is the most degrading phenomenon in low-rate feedforward control of piezoactive systems. A novel modeling framework based on the memory-dominant properties of hysteresis was proposed to achieve an accurate and computationally efficient methodology compared to the widely-used classical methods such as Preisach and Prandtl-Ishlinskii operators. At high-frequency operations, however, the disturbing effects of system dynamics becomes larger, and hence, reduces the control performance if not thoughtfully taken into account. Despite the distributed-parameters nature of piezoactive stages and due to their relatively high resonances, a lumped-parameters model can accurately predict the dynamic behavior of system in a wide frequency range. It was shown that a feedforward controller consisting of both hysteresis and dynamic compensators can effectively control the system in tracking of low and high frequency trajectories.

In practice, system parametric uncertainties and unmodeled dynamics necessitates the use of feedback strategies. Along this line, a Lypunov-based robust adaptive controller was proposed to accurately track desired trajectories despite the ever-present uncertainties and disturbances. Moreover, the controller demonstrated robust tracking performance with respect to the hysteresis effect; that is, without including any complex hysteresis model, highly accurate tracking results were achieved. Implementation of the proposed controller on a laser-free AFM setup was then investigated. It was shown that the frequency of raster scanning can be increased up to 30 Hz, where a PID controller yields significant errors. Hence, the proposed robust adaptive controller can be effectively utilized in high-speed SPM systems.

To track time-varying trajectories with frequent stepped discontinuities, a supervisory controller was developed. It was shown that two separate control modes are required for high-performance tracking of such trajectories. The supervisory controller switches between the controllers, one of which tuned for stepped trajectory tracking while the other one tuned for continuous trajectory tracking. Switching conditions and control input compatibility conditions at the switching instances which play important roles in effective and stable switching were derived and analyzed. Such a compound controller can be utilized in closed-loop SPM systems in imaging of surfaces with both smooth and jumped topographies.

To achieve precise ultra-high frequency tracking control of piezoactive nanopositioning systems, distributed-parameters modeling and control was shown to be inevitable. Taking a rod-like configuration for the stack piezoactive stages, the partial differential equation of motion and boundary conditions were obtained using the extended Hamilton's principle. Standard vibration analysis was carried out to derive the truncated finite-mode state-space representation of system. A new state-space controller was then proposed for asymptotic output tracking control of system. Integration of an optimal state-observer and a Lyapunov-based robust strategy were proposed to improve the practicability of the state-space controller. Simulation results demonstrated that distributed-parameters modeling and control is inevitable for ultra-high bandwidth tracking control of system.

Development of a state-space modeling framework for piezoelectrically-driven Nanomehcnical Cantilever (NMC) Active Probes with cross-sectional discontinuities was carried out at the last part of this dissertation utilizing the standard vibration analysis methods associated with the Euler-Bernoulli beams with stepped discontinuities. It was shown that modeling cross-sectional jumps is an essential factor for acquiring accurate results in a broad frequency range. The proposed framework was successfully utilized in a pico-gram scale mass detection application using the frequency-shift method. It was shown that the second mode of the current configuration of Active Probe is the most sensitive mode for ultra-small mass detection application since it demonstrates the largest shift in the frequency due to the added tip mass. This approach can benefit the measurement of gas densities and characterization of chemicals and biological species in various applications.

7.2. Future Works

Several directions are open for future investigations including:

- Generalization of memory-based hysteresis modeling framework for other smart materials and systems such as magnetostrictive actuators and shape memory alloys

- Experimental implementation of proposed distributed-parameters modeling and control framework in actual rod-type solid-state actuators for high-bandwidth tracking control
- Implementation of the supervisory switching controller for closed-loop control of AFM for constant force imaging of soft materials and samples
- Utilization of Active Probes for mass detection of biological species

APPENDICES

APPENDIX A

Derivation of Equation of Motion and Orthonormality Conditions for Rod-Type Solid-State Actuators*

A.1. Derivation of Equation of Motion using Hamilton's Principle

The partial deferential equation of motion representing the longitudinal vibrations of the actuator is derived here. The kinetic energy of the actuator having length L, mass per unit length ρ and the boundary mass m is given by:

$$T = \frac{1}{2}\int_0^L \rho\left(\frac{\partial u(x,t)}{\partial t}\right)^2 dx + \frac{1}{2}m\left(\frac{\partial u(L,t)}{\partial t}\right)^2 \tag{A.1}$$

The potential energy of the actuator with fixed stiffness E and cross-sectional area A is given by:

$$V = \frac{1}{2}\int_0^L EA\left(\frac{\partial u(x,t)}{\partial x}\right)^2 dx + \frac{1}{2}ku^2(L,t) \tag{A.2}$$

The external work done by the excitation force $f(t)$, the uniformly distributed damping force, and the damping force in the boundary are represented as:

$$\delta W_{ext} = f(t)\delta u(L,t) - \int_0^L B\left(\partial u(x,t)/\partial t\right)\delta u(x,t)dx - C\left(\partial u(L,t)/\partial t\right)\delta u(L,t) \tag{A.3}$$

---

* The contents of this chapter may have come directly or indirectly from our joint publication [62].

The extended Hamiltonian principle to find the equation of motion of system states:

$$\int_{t_1}^{t_2} \left(\delta\left(T - V\right) + \delta W_{ext} \right) dt = 0 \tag{A.4}$$

Substituting the kinetic energy, potential energy, and the external work, applying variation principle and rearranging all the terms, Eq. (A.4) becomes:

$$\begin{aligned} &\int_0^L \int_{t_1}^{t_2} \left\{ -\rho\left(\frac{\partial^2 u(x,t)}{\partial t^2}\right) + EA\left(\frac{\partial^2 u(x,t)}{\partial x^2}\right) - B\left(\frac{\partial u(x,t)}{\partial t}\right) \right\} \delta u(x,t) dx dt + \\ &\int_{t_1}^{t_2} \left\{ -m\left(\frac{\partial^2 u(L,t)}{\partial t^2}\right) - EA\left(\frac{\partial u(L,t)}{\partial x}\right) - C\left(\frac{\partial u(L,t)}{\partial t}\right) - ku(L,t) + f(t) \right\} \delta u(L,t) dt = 0 \end{aligned} \tag{A.5}$$

Since the integral of Hamiltonian from t_1 to t_2 must be zero, the integrant must vanish. Hence, Eq. (A.5) is recast as:

$$\begin{aligned} &\left\{ -\rho\left(\frac{\partial^2 u(x,t)}{\partial t^2}\right) + EA\left(\frac{\partial^2 u(x,t)}{\partial x^2}\right) - B\left(\frac{\partial u(x,t)}{\partial t}\right) \right\} \delta u(x,t) + \\ &\left\{ -m\left(\frac{\partial^2 u(L,t)}{\partial t^2}\right) - EA\left(\frac{\partial u(L,t)}{\partial x}\right) - C\left(\frac{\partial u(L,t)}{\partial t}\right) - ku(L,t) + f(t) \right\} \delta u(L,t) = 0 \end{aligned} \tag{A.6}$$

Since $\delta u(x,t)$ and $\delta u(L,t)$ can take any arbitrary values, for Eq. (A.6) to hold we must have:

$$\rho\left(\frac{\partial^2 u(x,t)}{\partial t^2}\right) - EA\left(\frac{\partial^2 u(x,t)}{\partial x^2}\right) + B\left(\frac{\partial u(x,t)}{\partial t}\right) = 0 \tag{A.7}$$

and

$$m\left(\frac{\partial^2 u(L,t)}{\partial t^2}\right) + EA\left(\frac{\partial u(L,t)}{\partial x}\right) + C\left(\frac{\partial u(L,t)}{\partial t}\right) + ku(L,t) = f(t) \tag{A.8}$$

Eq. (A.7) and Eq. (A.8), respectively, represent the equation of motion for system and boundary condition at $x = L$.

A.2. Derivation of Orthonormality Conditions

Applying separation of variable to un-damped free boundary condition of system yields:

$$m\phi_r(L)\ddot{q}_r(t) + EA\phi_r'(L)q_r(t) + k\phi_r(L)q_r(t) = 0 \tag{A.9}$$

Substituting Eq. (5.7) and rearranging the terms, Eq. (A.9) yields:

$$\phi_r'(L) = \gamma_r\phi_r(L);\ \ \gamma_r = (m\omega_r^2 - k)\big/EA \tag{A.10}$$

The equation of motion in the spatial domain for r^{th} and s^{th} mode of the actuator can be represented as:

$$\phi_r''(x) = -\beta_r^2\phi_r(x),\ \ \phi_s''(x) = -\beta_s^2\phi_s(x) \tag{A.11}$$

Multiplying the first equation in (A.11) by $\phi_s(x)$ and the second equation by $\phi_r(x)$, integrating over the rod length and performing integral by parts, it follows that:

$$\phi_r'(L)\phi_s(L) - \int_0^L \phi_r'(x)\phi_s'(x)dx = -\beta_r^2\int_0^L \phi_r(x)\phi_s(x)dx \tag{A.12}$$

$$\phi_s'(L)\phi_r(L) - \int_0^L \phi_s'(x)\phi_r'(x)dx = -\beta_s^2\int_0^L \phi_s(x)\phi_r(x)dx \tag{A.13}$$

Subtracting Eq. (A.12) from Eq. (A.13) and using Eq. (A.10) yields:

$$(\beta_r^2 - \beta_s^2)\left\{\rho\int_0^L \phi_r(x)\phi_s(x)dx + m\phi_r(L)\phi_s(L)\right\} = 0 \tag{A.14}$$

Since $\beta_r \neq \beta_s$ (or $\omega_r \neq \omega_s$) for two different modes (i.e. $r \neq s$), $\beta_r^2 - \beta_s^2 \neq 0$ and hence, Eq. (A.14) results in:

$$\rho\int_0^L \phi_r(x)\phi_s(x)dx + m\phi_r(L)\phi_s(L) = \delta_{rs} \tag{A.15}$$

Eq. (A.15) represents the orthonormality condition for the longitudinal vibrations of the actuator with respect to mass.

In order to obtain the orthogonality condition with respect to stiffness, we substitute Eq. (A.10) into Eq. (A.12), use Eq. (A.15) and rearrange the required terms to get:

$$EA\int_0^L \phi_r'(x)\phi_s'(x)dx + k\phi_r(L)\phi_s(L) = \omega_r^2\delta_{rs} \tag{A.16}$$

Eq. (A.16) represents the orthogonality condition of mode shapes with respect to stiffness.

APPENDIX B

Modeling and Vibration Analysis of Stepped Euler-Bernoulli Beams with Application to Piezoelectric Active Probes*

Consider an initially straight non-uniform Euler Bernoulli beam of length L, with variable cross section $A = A(x)$, variable stiffness $E = E(x)$, and variable moment of inertia $I = I(x)$. Let $x \in [0, L]$ and $t \in [0, \infty)$ be the spatial and time variables, respectively. The governing equation for transverse vibration of beam with variable mass per unit length $m(x)$ and damping coefficient of $c(x)$ subjected to a vertical time varying distributed load $P(x,t)$ is a fourth-order partial differential equation expressed as:

$$\frac{\partial^2}{\partial x^2}\left(E(x)I(x)\frac{\partial^2 w(x,t)}{\partial x^2} \right) + c(x)\frac{\partial w(x,t)}{\partial t} + m(x)\frac{\partial^2 w(x,t)}{\partial t^2} = P(x,t) \tag{B.1}$$

with $w(x,t)$ being the beam transversal displacement. In order to obtain natural frequencies and eigenfunctions (mode shapes) of this system, the eigenvalue problem associated with the transversal vibration of beam is obtained by applying free and un-damped conditions to Eq. (B.1) as follows:

$$\frac{\partial^2}{\partial x^2}\left(E(x)I(x)\frac{\partial^2 w(x,t)}{\partial x^2} \right) = -m(x)\frac{\partial^2 w(x,t)}{\partial t^2} \tag{B.2}$$

Let's assume that the solution of Eq. (B.2) is separable in time and space domains,

* The contents of this chapter may have come directly or indirectly from our joint publication [101].

$$w(x,t) = \phi(x)q(t) \tag{B.3}$$

where $\phi(x)$ denotes the spatial shape function and $q(t)$ represents the generalized time-dependent coordinate. Substituting Eq. (B.3) into Eq. (B.2), the eigenvalue equation can be written in the following form of separated time and space equations:

$$\frac{d^2}{dx^2}\left(E(x)I(x)\frac{d^2\phi(x)}{dx^2} \right) / \left(m(x)\phi(x) \right) = -\ddot{q}(t)/q(t) = \omega^2 \tag{B.4}$$

where ω is a constant parameter. The mode shapes are obtained by solving the spatial part of Eq. (B.4) written as:

$$\frac{d^2}{dx^2}\left(E(x)I(x)\frac{d^2\phi(x)}{dx^2} \right) = \omega^2 m(x)\phi(x) \tag{B.5}$$

For a beam with parametric discontinuities (e.g., jump in the moment of inertia or mass distribution), Eq. (B.5) cannot be solved using conventional approaches. An alternative method is to partition the beam into uniform segments between any two successive stepped points and apply the continuity conditions at these points. Therefore, the non-uniform beam is converted to a set of uniform segments constrained through the continuity conditions.

B.1. Modal analysis of stepped Euler Bernoulli beam

Figure B.1 illustrates a straight Euler Bernoulli beam with arbitrary boundary conditions and N jumped discontinuities in its spatial span. The beam considered in this study has a uniform cross-section at each segment. Hence, Eq. (B.5) can be divided into N uniform equations expressed as:

$$(EI)_n \frac{d^4\phi_n(x)}{dx^4} = \omega^2 m_n \phi_n(x)\,, \quad l_{n\text{-}1} < x < l_n;\;\; n = 1,2,3,\ldots,N;\;\; l_0=0 \tag{B.6}$$

where $\phi_n(x)$, $(EI)_n$, and m_n are mode shapes, flexural stiffness, and mass per unit length of beam at the n^{th} segment, respectively[†]. Let,

$$\beta_n^4 = \omega^2 \frac{m_n}{(EI)_n} \tag{B.7}$$

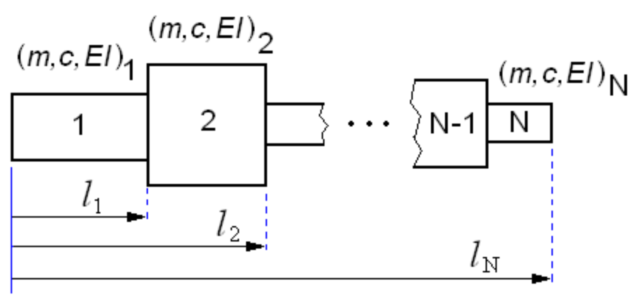

Figure B.1. EB beam configuration with N jumped discontinuities.

Eq. (B.6) can be rewritten in a more recognizable form

$$\frac{d^4\phi_n(x)}{dx^4} - \beta_n^4 \phi_n(x) = 0 \tag{B.8}$$

with the following general solution

$$\phi_n(x) = A_n \sin\beta_n x + B_n \cos\beta_n x + C_n \sinh\beta_n x + D_n \cosh\beta_n x \tag{B.9}$$

[†] $(\;)_n$ denotes the mode shape or parameter value for the n^{th} cross-section, while $(\;)^{(r)}$, which will be used later in the paper, denotes the mode shape or parameter value of the r^{th} mode; though, ω_r which represents the r^{th} natural frequency is an exception.

where A_n, B_n, C_n, and D_n are the constants of integration determined by suitable boundary and continuity conditions. It is to be noted that any conventional boundary conditions can be applied to the beam; however, without the loss of generality, the clamped-free conditions are chosen here for the boundaries. Applying the clamped condition at $x = 0$ requires[‡]:

$$\phi_1(0) = \frac{d\phi_1(0)}{dx} = 0 \tag{B.10}$$

Substituting Eq. (B.10) into Eq. (B.9) yields:

$$B_1 + D_1 = 0 \quad \text{and} \quad A_1 + C_1 = 0 \tag{B.11}$$

On the other hand, the continuity conditions for displacement, slope, bending moment, and shear force of beam at discontinuity locations are given by:

$$\phi_n(l_n) = \phi_{n+1}(l_n) \tag{B.12}$$

$$\frac{d\phi_n(l_n)}{dx} = \frac{d\phi_{n+1}(l_n)}{dx} \tag{B.13}$$

$$(EI)_n \frac{d^2\phi_n(l_n)}{dx^2} = (EI)_{n+1} \frac{d^2\phi_{n+1}(l_n)}{dx^2} \tag{B.14}$$

$$(EI)_n \frac{d^3\phi_n(l_n)}{dx^3} = (EI)_{n+1} \frac{d^3\phi_{n+1}(l_n)}{dx^3} \tag{B.15}$$

‡ $\frac{d^q\phi(l_n)}{dx^q} \equiv \left.\frac{d^q\phi(x)}{dx^q}\right|_{x=l_n}$.

Indeed, these conditions are applied at the boundaries of adjacent segments to satisfy the continuity and equilibrium conditions immediately before and after stepped points. Applying conditions (B.12)-(B.15) to Eq. (B.9) results in:

$$\begin{aligned}&A_n \sin\beta_n l_n + B_n \cos\beta_n l_n + C_n \sinh\beta_n l_n + D_n \cosh\beta_n l_n = \\ &A_{n+1} \sin\beta_{n+1} l_n + B_{n+1} \cos\beta_{n+1} l_n + C_{n+1} \sinh\beta_{n+1} l_n + D_{n+1} \cosh\beta_{n+1} l_n\end{aligned} \tag{B.16}$$

$$\begin{aligned}&\beta_n (A_n \cos\beta_n l_n - B_n \sin\beta_n l_n + C_n \cosh\beta_n l_n + D_n \sinh\beta_n l_n) = \\ &\beta_{n+1} (A_{n+1} \cos\beta_{n+1} l_n - B_{n+1} \sin\beta_{n+1} l_n + C_{n+1} \cosh\beta_{n+1} l_n + D_{n+1} \sinh\beta_{n+1} l_n)\end{aligned} \tag{B.17}$$

$$\begin{aligned}&\gamma_n \beta_n^2 (-A_n \sin\beta_n l_n - B_n \cos\beta_n l_n + C_n \sinh\beta_n l_n + D_n \cosh\beta_n l_n) = \\ &\beta_{n+1}^2 (-A_{n+1} \sin\beta_{n+1} l_n - B_{n+1} \cos\beta_{n+1} l_n + C_{n+1} \sinh\beta_{n+1} l_n + D_{n+1} \cosh\beta_{n+1} l_n)\end{aligned} \tag{B.18}$$

$$\begin{aligned}&\gamma_n \beta_n^3 (-A_n \cos\beta_n l_n + B_n \sin\beta_n l_n + C_n \cosh\beta_n l_n + D_n \sinh\beta_n l_n) = \\ &\beta_{n+1}^2 (-A_{n+1} \cos\beta_{n+1} l_n + B_{n+1} \sin\beta_{n+1} l_n + C_{n+1} \cosh\beta_{n+1} l_n + D_{n+1} \sinh\beta_{n+1} l_n)\end{aligned} \tag{B.19}$$

where $\gamma_n = \dfrac{(EI)_n}{(EI)_{n+1}}$.

Finally, the free boundary condition at $x = L$ requires:

$$\frac{d^2\phi_N(l_N)}{dx^2} = \frac{d^3\phi_N(l_N)}{dx^3} = 0 \tag{B.20}$$

Substituting Eq. (B.20) into Eq. (B.9) yields:

$$\beta_N^2 (-A_N \sin\beta_N l_N - B_N \cos\beta_N l_N + C_N \sinh\beta_N l_N + D_N \cosh\beta_N l_N) = 0 \tag{B.21}$$

$$\beta_N^3 (-A_N \cos\beta_N l_N + B_N \sin\beta_N l_N + C_N \cosh\beta_N l_N + D_N \sinh\beta_N l_N) = 0 \tag{B.22}$$

Note that β_n 's are functions of beam natural frequency with an explicit expression given in Eq. (B.7). Since the natural frequency is independent of segments indices and is considered for the entire length of beam, β_n 's of different segments can be interrelated in terms of a single parameter β using Eq. (B.7):

$$\beta_n = \beta\alpha_n \tag{B.23}$$

where

$$\alpha_n = \left(\frac{m_n (EI)_1}{m_1 (EI)_n}\right)^{1/4} \tag{B.24}$$

Note that $\alpha_1 = 1$, and thus $\beta = \beta_1$.

Eqs. (B.11), (B.21), and (B.22), derived from boundary conditions, together with Eqs. (B.16)-(B.19), obtained from the continuity conditions, will form the characteristics matrix equation as:

$$\mathbf{J}_{4N\times 4N}\mathbf{P}_{4N\times 1} = \mathbf{0} \tag{B.25}$$

where **J** is the characteristics matrix and **P** is the vector of mode shape coefficients

$$\mathbf{P} = [A_1\ B_1\ C_1\ D_1\ A_2\ B_2\ C_2\ D_2\ \cdots\ A_N\ B_N\ C_N\ D_N]^{\mathrm{T}}_{1\times 4\mathrm{N}} \tag{B.26}$$

Matrix **J** is constructed based on three sets of equations. The first two rows and last two rows represent the boundary conditions at $x = 0$ and $x = L$, respectively, and the middle part of matrix demonstrates the continuity conditions at the singularity points. Matrix **J** can be divided into three parts as:

$$
\mathbf{J} = \begin{bmatrix} \left[\mathbf{J_1}\right]_{2\times 4N} \\ \left[\mathbf{J_2}\right]_{4(N-1)\times 4N} \\ \left[\mathbf{J_3}\right]_{2\times 4N} \end{bmatrix}_{4N\times 4N} \tag{B.27}
$$

where

$$
\mathbf{J}_1 = \begin{bmatrix} 0 & 1 & 0 & 1 & 0 & \cdots & 0 \\ 1 & 0 & 1 & 0 & 0 & \cdots & 0 \end{bmatrix}_{2\times 4N} \tag{B.28}
$$

represents the clamed boundary condition at $x = 0$ given by Eq. (B.11),

$$
\mathbf{J_2} = \begin{bmatrix} \overset{1}{[} \quad J_2^{(1)} \quad \overset{8}{]}_{4\times 8} & & & \\ & \overset{5}{[} \quad J_2^{(2)} \quad \overset{12}{]}_{4\times 8} & & \mathbf{0} \\ & & \ddots & \\ \mathbf{0} & & & \overset{4(N-2)}{[} \quad J_2^{(N-1)} \quad \overset{4N}{]}_{4\times 8} \end{bmatrix}_{4(N-1)\times 4N} \tag{B.29}
$$

includes the continuity conditions given by Eqs. (B.16)-(B.19) at (N-1) points of discontinuity with

$$
J_2^{(n)} = \left[\begin{matrix} \sin\alpha_n\beta l_n & \cos\alpha_n\beta l_n & \sinh\alpha_n\beta l_n & \cosh\alpha_n\beta l_n \\ \alpha_n\beta \;\cos\alpha_n\beta l_n & -\alpha_n\beta \;\sin\alpha_n\beta l_n & \alpha_n\beta \;\cosh\alpha_n\beta l_n & \alpha_n\beta \;\sinh\alpha_n\beta l_n \\ -\gamma_n\alpha_n^2\beta^2\sin\alpha_n\beta l_n & -\gamma_n\alpha_n^2\beta^2\cos\alpha_n\beta l_n & \gamma_n\alpha_n^2\beta^2\sinh\alpha_n\beta l_n & \gamma_n\alpha_n^2\beta^2\cosh\alpha_n\beta l_n \\ -\gamma_n\alpha_n^3\beta^3\cos\alpha_n\beta l_n & \gamma_n\alpha_n^3\beta^3\sin\alpha_n\beta l_n & \gamma_n\alpha_n^3\beta^3\cosh\alpha_n\beta l_n & \gamma_n\alpha_n^3\beta^3\sinh\alpha_n\beta l_n \end{matrix}\right.
$$

$$
\left.\begin{matrix} -\sin\alpha_{n+1}\beta l_n & -\cos\alpha_{n+1}\beta l_n & -\sinh\alpha_{n+1}\beta l_n & -\cosh\alpha_{n+1}\beta l_n \\ -\alpha_{n+1}\beta \;\cos\alpha_{n+1}\beta l_n & \alpha_{n+1}\beta \;\sin\alpha_{n+1}\beta l_n & -\alpha_{n+1}\beta \;\cosh\alpha_{n+1}\beta l_n & -\alpha_{n+1}\beta \;\sinh\alpha_{n+1}\beta l_n \\ \alpha_{n+1}^2\beta^2\sin\alpha_{n+1}\beta l_n & \alpha_{n+1}^2\beta^2\cos\alpha_{n+1}\beta l_n & -\alpha_{n+1}^2\beta^2\sinh\alpha_{n+1}\beta l_n & -\alpha_{n+1}^2\beta^2\cosh\alpha_{n+1}\beta l_n \\ \alpha_{n+1}^3\beta^3\cos\alpha_{n+1}\beta l_n & -\alpha_{n+1}^3\beta^3\sin\alpha_{n+1}\beta l_n & -\alpha_{n+1}^3\beta^3\cosh\alpha_{n+1}\beta l_n & -\alpha_{n+1}^3\beta^3\sinh\alpha_{n+1}\beta l_n \end{matrix}\right]_{4\times 8} \tag{B.30}
$$

and

$$\mathbf{J}_3 = \begin{bmatrix} 0 & \cdots & 0 & -\alpha_N^2\beta^2 \sin\alpha_N\beta l_N & -\alpha_N^2\beta^2 \cos\alpha_N\beta l_N & \alpha_N^2\beta^2 \sinh\alpha_N\beta l_N & \alpha_N^2\beta^2 \cosh\alpha_N\beta l_N \\ 0 & \cdots & 0 & -\alpha_N^3\beta^3 \cos\alpha_N\beta l_N & \alpha_N^3\beta^3 \sin\alpha_N\beta l_N & \alpha_N^3\beta^3 \cosh\alpha_N\beta l_N & \alpha_N^3\beta^3 \sinh\alpha_N\beta l_N \end{bmatrix}_{2\times 4N} \tag{B.31}$$

represents the free boundary condition at $x = L$ given by Eqs. (B.21) and (B.22).

In order to obtain a non-trivial solution for Eq. (B.25) and find the natural frequencies and mode shapes, the determinant of matrix **J** must be set to zero,

$$\det\left[\mathbf{J}(\beta)\right] = 0 \tag{B.32}$$

Since this matrix is a function of only parameter $\beta \in (0, \infty)$, its determinant can be numerically evaluated for its zero values by continuously varying parameter β with a reasonably small step size within a range of interest starting from, but excluding, zero. The values of β which satisfy Eq. (B.32) lead to calculation of natural frequencies using a modified version of Eq. (B.7) as follows:

$$\omega_r^2 = \left(\beta^{(r)}\right)^4 \frac{(EI)_1}{m_1} = \left(\beta_n^{(r)}\right)^4 \frac{(EI)_n}{m_n} \tag{B.33}$$

where $\beta^{(r)}$s are solutions for Eq. (B.32) and ω_r is the corresponding r^{th} natural frequency. Since the determinant of matrix **J** has been set to zero for the selected values of β, the mode shape coefficients A_1 to D_N are linearly dependent. In order to obtain unique solution for these coefficients, orthogonality between mode shapes can be utilized. For the conventional boundary conditions considered here, this condition is stated as:

$$\int_{l_0}^{l_N} m(x)\phi^{(r)}(x)\phi^{(s)}(x)dx = \delta_{rs} \text{ or } \int_{l_0}^{l_N} m(x)\left(\phi^{(r)}(x)\right)^2 dx = 1 \tag{B.34}$$

where δ_{rs} is the Kronecker delta, and $\phi^{(r)}(x)$ is the r^{th} mode shape of beam expressed as:

$$\phi^{(r)}(x) = \begin{cases} \phi_1^{(r)}(x) = A_1^{(r)} \sin\beta_1^{(r)}x + B_1^{(r)}\cos\beta_1^{(r)}x + C_1^{(r)}\sinh\beta_1^{(r)}x + D_1^{(r)}\cosh\beta_1^{(r)}, & l_0 \le x \le l_1 \\ \phi_2^{(r)}(x) = A_2^{(r)} \sin\beta_2^{(r)}x + B_2^{(r)}\cos\beta_2^{(r)}x + C_2^{(r)}\sinh\beta_2^{(r)}x + D_2^{(r)}\cosh\beta_2^{(r)}x, & l_1 < x \le l_2 \\ \vdots \\ \phi_N^{(r)}(x) = A_N^{(r)} \sin\beta_N^{(r)}x + B_N^{(r)}\cos\beta_N^{(r)}x + C_N^{(r)}\sinh\beta_N^{(r)}x + D_N^{(r)}\cosh\beta_N^{(r)}x, & l_{N-1} < x \le l_N \end{cases} \tag{B.35}$$

The obtained mode shapes and natural frequencies are used to derive the equation of motion for a beam under distributed dynamic excitation as will be discussed next.

B.2. Forced motion analysis of stepped Euler Bernoulli beam

Using expansion theorem for the beam vibration analysis, the expression for the transverse displacement becomes:

$$w(x,t) = \sum_{r=1}^{\infty} \phi^{(r)}(x)q^{(r)}(t) \tag{B.36}$$

where $q^{(r)}(t)$ is the generalized time-dependent coordinate for the r^{th} mode. Substituting Eq. (B.36) into partial differential equation of motion, Eq. (B.1), yields:

$$\sum_{r=1}^{\infty}\left\{\frac{d^2}{dx^2}\left[E(x)I(x)\frac{d^2\phi^{(r)}(x)}{dx^2}\right]q^{(r)}(t) + c(x)\phi^{(r)}(x)\dot{q}^{(r)}(t) + m(x)\phi^{(r)}(x)\ddot{q}^{(r)}(t)\right\} = P(x,t) \tag{B.37}$$

To safely take the term $E(x)I(x)$ out of the bracket for the beam with multiple discontinuities, Eq. (B.37) is multiplied by s^{th} mode shape $\phi^{(s)}(x)$ and integrated over the beam length:

$$\int_{l_0}^{l_N}\left\{\sum_{r=1}^{\infty}\left(\frac{d^2}{dx^2}\left[E(x)I(x)\frac{d^2\phi^{(r)}(x)}{dx^2}\right]\phi^{(s)}(x)q^{(r)}(t)+c(x)\phi^{(r)}(x)\phi^{(s)}(x)\dot{q}^{(r)}(t)\right.\right.$$
$$\left.\left.+m(x)\phi^{(r)}(x)\phi^{(s)}(x)\ddot{q}^{(r)}(t)\right)\right\}dx=\int_{l_0}^{l_N}P(x,t)\phi^{(s)}(x)dx \tag{B.38}$$

Recall Eq. (B.6) which can be modified to

$$(EI)_n\frac{d^4\phi_n^{(r)}(x)}{dx^4}=\omega_r^2 m_n\phi_n^{(r)}(x) \tag{B.39}$$

Using Eq. (B.39) and dividing the spatial integral into N uniform segments, one can write:

$$\int_{l_0}^{l_N}\left(\frac{d^2}{dx^2}\left[E(x)I(x)\frac{d^2\phi^{(r)}(x)}{dx^2}\right]\phi^{(s)}(x)q^{(r)}(t)\right)dx=\sum_{n=1}^{N}\left[\int_{l_{n-1}}^{l_n}(EI)_n\frac{d^4\phi_n^{(r)}(x)}{dx^4}\phi_n^{(s)}(x)q^{(r)}(t)dx\right]=$$
$$\sum_{n=1}^{N}\left[\int_{l_{n-1}}^{l_n}\omega_r^2 m_n\phi_n^{(r)}(x)\phi_n^{(s)}(x)q^{(r)}(t)dx\right]=\omega_r^2 q^{(r)}(t)\int_{l_0}^{l_N}m(x)\phi^{(r)}(x)\phi^{(s)}(x)dx$$

(B.40)

Applying beam orthogonality conditions given by:

$$\int_{l_0}^{l_N}m(x)\phi^{(r)}(x)\phi^{(s)}(x)dx=\delta_{rs},\quad \int_{l_0}^{l_N}E(x)I(x)\phi^{(r)}(x)\phi^{(s)}(x)dx=\omega_r^2\delta_{rs} \tag{B.41}$$

and using Eq. (B.40), Eq. (B.38) can be recast as:

$$\ddot{q}^{(r)}(t) + \sum_{s=1}^{\infty}\left\{\dot{q}^{(s)}(t)\int_{l_0}^{l_N} c(x)\phi^{(r)}(x)\phi^{(s)}(x)dx\right\} + \omega_r^2 q^{(r)}(t) = \int_{l_0}^{l_N} P(x,t)\phi^{(r)}(x)dx \ , \ r = 1,2,...,\infty \tag{B.42}$$

which can be simplified to

$$\ddot{q}^{(r)}(t) + \sum_{s=1}^{\infty}\left\{c_{rs}\dot{q}^{(s)}(t)\right\} + \omega_r^2 q^{(r)}(t) = f^{(r)}(t), \ \ r = 1,2,...,\infty \tag{B.43}$$

where

$$c_{rs} = \int_{l_0}^{l_N} c(x)\phi^{(r)}(x)\phi^{(s)}(x)dx, \quad f^{(r)}(t) = \int_{l_0}^{l_N} P(x,t)\phi^{(r)}(x)dx \tag{B.44}$$

The truncated k-mode description of the beam Eq. (B.43) can now be presented in the following matrix form:

$$\mathbf{M}\ddot{\mathbf{q}} + \mathbf{C}\dot{\mathbf{q}} + \mathbf{K}\mathbf{q} = \mathbf{F} \tag{B.45}$$

where

$$\begin{aligned}&\mathbf{M} = I_{k\times k}, \mathbf{C} = [c_{rs}]_{k\times k}, \mathbf{K} = [\omega_r^2\delta_{rs}]_{k\times k}, \mathbf{q} = [q^{(1)}(t), q^{(2)}(t), \ldots, q^{(k)}(t)]_{k\times 1}^T, \\ &\mathbf{F} = [f^{(1)}(t), f^{(2)}(t), \ldots, f^{(k)}(t)]_{k\times 1}^T\end{aligned} \tag{B.46}$$

From the systems and control standpoint, Eq. (B.45) can be presented in the standard state-space form. This not only facilitates the control design procedure for the system, but also helps to characterize various properties of system, including stability, controllability and observability. The state-space representation of Eq. (B.45) is given by:

$$\dot{\mathbf{X}} = \mathbf{AX} + \mathbf{Bu} \tag{B.47}$$

where

$$\mathbf{A} = \begin{bmatrix} \mathbf{0} & \mathbf{I} \\ \mathbf{-M^{-1}K} & \mathbf{-M^{-1}C} \end{bmatrix}_{2k \times 2k},\ \mathbf{B} = \begin{bmatrix} \mathbf{0} \\ \mathbf{M^{-1}} \end{bmatrix}_{2k \times k},\ \mathbf{X} = \begin{Bmatrix} \mathbf{q} \\ \dot{\mathbf{q}} \end{Bmatrix}_{2k \times 1},\ \mathbf{u} = \mathbf{F}_{k \times 1} \tag{B.48}$$

REFERENCES

[1] Curie J. and Curie P., “Développement, par pression, de l’électricité polaire dans les cristaux hémièdres à faces inclinées,” *Comptes Rendus de l'Académie des Sciences, Paris*, **91**, pp. 294-295, 1880.

[2] Trainer M., “Kelvin and piezoelectricity,” *European Journal of Physics*, **24**, pp. 535-542, 2003.

[3] Mason W. P., “Piezoelectricity, its history and applications,” *Journal of Acoustical Society of America*, **70**, pp. 1561-1566, 1981.

[4] Berlincourt D., “Piezoelectric ceramics: characteristics and applications,” *Journal of Acoustical Society of America*, **70**, pp. 1586-1595, 1981.

[5] Damjanovic D., “Ferroelectric, dielectric and piezoelectric properties of ferroelectric thin films and ceramics,” *Reports on Progress in Physics*, **61**, pp. 1267-1324, 1998.

[6] Mele E. J. and Kral P., “Electric polarization of heteropolar nanotubes as a geometric phase,” *Physical Review Letters*, **88**, pp. 568031-568034, 2002.

[7] Jalili N., “Nanotube-based actuator and sensor paradigm: conceptual design and challenges,” *Proceedings of 2003 ASME International Mechanical Engineering Congress & Exposition,* Washington, DC, 2003.

[8] Tutorial: Piezoelectrics in positioning contents, Physik Instrumente manual, www.pi.ws.

[9] Gunev I., Varol A., Karaman S. and Basdogan C., “Adaptive Q control for tapping-mode nanoscanning using a piezoactuated bimorph probe,” *Review of Scientific Instruments*, **78**, 043707, 2007.

[10] Rogers B., Manning L., Sulchek T. and Adams J. D., “Improving tapping mode atomic force microscopy with piezoelectric antilevers,” *Ultramicroscopy*, **100**, pp. 267-276, 2004.

[11] Gurjar M. and Jalili N., "Toward ultrasmall mass detection using adaptive self-sensing piezoelectrically-driven microcantilevers", *IEEE/ASME Transaction on Mechatronics*, **12**, pp. 680-688, 2007.

[12] Mahmoodi S. N., and Jalili N., "Non-linear vibrations and frequency response analysis of piezoelectrically-driven microcantilevers", *International Journal of Non-Linear Mechanics*, **42**, pp. 577-587, 2007.

[13] Audigier D., Eyraud L., Eyraud P., Eyraud F., Glissa N., Gonnard P., Troccaz M. and Sprumont M., "Typical characteristics of a piezoelectric ceramic material for squeeze igniters," *IEEE International Symposium on Applications of Ferroelectrics*, pp. 383-386,1994.

[14] Sodano H. A., Inman D. J. and Park G., "Comparison of piezoelectric energy harvesting devices for recharging batteries," *Journal of Intelligent Material Systems and Structures*, **16**, pp. 799-807, 2005.

[15] Tomikawa Y. and Okada S., "Piezoelectric angular acceleration sensor," *Proceedings of the IEEE Ultrasonics Symposium*, **2**, pp. 1346-1349, 2003.

[16] Caliano G., Lamberti N., Iula A. and Pappalardo M., "Piezoelectric bimorph static pressure sensor," *Sensors and Actuators, A: Physical*, **46**, pp. 176-178, 1995.

[17] Matsunaka T., Tabuchi Y., Kasai C., Tachikawa K., Kyono H. and Ikeda H., "Porous piezoelectric ceramic transducer for medical ultrasonic applications," *Ultrasonics Symposium Proceedings*, **2**, pp. 681-684, 1988.

[18] Billson D. and Hutchins D., "Development of novel piezoelectric ultrasonic transducers for couplant-free non-destructive testing," *British Journal of Non-Destructive Testing*, **35**, pp. 705-709, 1993.

[19] Krasnosel'skii M. A. and Pokrovskii A. V., *Systems with hysteresis*, Springer-Verlag, NY, 1989.

[20] Bashash S. and Jalili N., "Underlying memory-dominant nature of hysteresis in piezoelectric materials," *Journal of Applied Physics*, **100**, pp. 014103, 2006.

[21] Bashash S. and Jalili N., "Intelligent rules of hysteresis in feedforward trajectory control of piezoelectrically-driven nanostages," *Journal of Micromechanics and Microengineering,* **17**, pp. 342-349, 2007.

[22] Bashash S. and Jalili N., "A polynomial-based linear mapping strategy for compensation of hysteresis in piezoelectric actuators," *ASME Transactions, Journal of Dynamic Systems, Measurements and Control*, **130**, pp. 031008 (1-10), 2008.

[23] Ping G. and Musa J., "Generalized Preisach model for hysteresis nonlinearity of piezoceramic actuators," *Precision Engineering*, **20**, pp. 99-111, 1997.

[24] Ping G. and Musa J., "Modeling hysteresis in piezoceramic actuators," *Precision Engineering*, **17**, pp. 211-221, 1995.

[25] Kuhnen K. and Janocha H., "Inverse feedforward controller for complex hysteretic nonlinearities in smart-material systems," *Control and Intelligent Systems*, **29**, pp. 74-83, 2001.

[26] Bashash S. and Jalili N., "Robust multiple-frequency trajectory tracking control of piezoelectrically-driven micro/nano positioning systems," *IEEE Transactions on Control Systems Technology*, **15**, pp. 867-878, 2007.

[27] Lining S., Changhai R., Weibin R., Liguo C. and Kong M., "Tracking control of piezoelectric actuator based on a new mathematical model," *Journal of Micromechanics and Microengineering,* **14**, pp. 1439-1444, 2004.

[28] Changhai R. and Lining S., "Improving positioning accuracy of piezoelectric actuators by feedforward hysteresis compensation based on a new mathematical model," *Review of Scientific Instruments*, **76**, pp. 095111-1:8, 2005.

[29] Aderiaens H., Koning W. and Baning R., "Modeling piezoelectric actuators," *IEEE/ASME Transactions on Mechatronics*, **5**, pp. 331-341, 2000.

[30] Smith R., *Smart material systems: Model developments*, SIAM, Philadelphia, PA.

[31] Chen B. M., Lee T. H., Hang C. C., Guo Y. and Weerasooriya S., "An H^{∞} almost disturbance decoupling robust controller design for a piezoelectric bimorph actuator with hyteresis," *IEEE Transactions on Control Systems Technology*, **7**, pp. 160-174, 1999.

[32] Hwang C. L., Chen Y. M. and Jan C., "Trajectory tracking of large displacement piezoelectric actuators using a nonlinear observer-based variable structure control," *IEEE Transactions on Control Systems Technology*, **13**, pp. 56-66, 2005.

[33] Bashash S. and Jalili N., "Real-time identification of piezoelectric actuator nonlinearities with application to precision trajectory control," *Proceedings of 2006 American Control Conference*, June 2006, Minneapolis, MN.

[34] Dadfarnia M., Jalili N., Xian B. and Dawson D. M., "A Lyapunov-Based Piezoelectric Controller for Flexible Cartesian Robot Manipulators", *ASME Journal of Dynamic Systems, Measurement, and Control*, **126**, pp. 347-358, 2004.

[35] Dadfarnia M., Jalili N., Liu Z. and Dawson D. M., "An observer-based piezoelectric control of flexible Cartesian robot arms: theory and experiment", *Control Engineering Practice*, **12**, pp. 1041–1053, 2004.

[36] Ogden J. W. and Grandhi R. V., "Optimal placement of a piezoelectric patch on plate structures for vibration suppression", Proceedings of *SPIE Annual Symposium on Smart Structures and Materials*, pp. 170-184, 1996.

[37] Xu Y. and Meckl P. H., "Time-optimal motion control of piezoelectric actuator: STM application," *Proceeding of the 2004 American Control Conference*, **5**, pp. 4849-4854, June 30-July 2, 2004, Boston, MA.

[38] Tzen J. J., Jeng S. L. and Chieng W. H., "Modeling of piezoelectric actuator for compensation and controller design," *Precision Engineering*, **27**, pp. 70-76, 2003.

[39] Bashash S. and Jalili N., "Trajectory control of piezoelectric actuators using nonlinear variable structure control," *Proceeding of International Symposium on Collaborative Research in Applied Science*, October 7-9, 2005, Vancouver, BC.

[40] Bashash S. and Jalili N., “A new hysteresis model for piezoelectric actuators with application to precision trajectory control,” *Proceeding of 2005 ASME International Mechanical Engineering Congress and Exposition*, Orlando, FL, Nov. 5-11, 2005.

[41] Tao G. and Kokotovic P. V., “Adaptive control of plants with unknown hysteresis,” *IEEE Transactions on Automatic Control*, **40,** pp. 200-212, 1995.

[42] Ku S. S., Pinsopon U., Cetinkunt S. and Nakjima S., “Design, fabrication, and real-time neural network of a three-degrees-of- freedom nanopositioner,” *IEEE/ASME Transactions on Mechatronics*, **5**, pp. 273-280, 2000.

[43] Goldfarb M. and Celanovic N., “A lumped parameter electromechanical model for describing the nonlinear behavior of piezoelectric actuators,” *ASME Journal of Dynamic Systems, Measurement and Control,* **119**, pp. 478–485, 1997.

[44] Ang W. T., Garmon F. A., Khosla P. K. and Riviere C. N., “Modeling rate-dependent hysteresis in piezoelectric actuators,” *Proceeding of IEEE International Conference on Intelligent Robots and Systems*, **2**, pp. 1975-1980, Las Vegas, NV, Oct. 2003.

[45] Newcomb C. and Filnn I., “Improving linearity of piezoelectric ceramic actuators,” *Electronics Letters*, **18**, pp. 442-444, 1982.

[46] Furutani K., Urushibata M. and Mohri N., “Displacement control of piezoelectric element by feedback of induced charge,” *Nanotechnology*, **9**, pp. 93-98, 1998.

[47] Salapaka S., Sebastian A., Cleveland J. P. and Salapaka M. V., “High bandwidth nano-positioner: a robust control approach,” *Review of Scientific Instruments*, **73**, pp. 3232-3241, 2002.

[48] Huang Y. C. and Cheng C. H., “Robust tracking control of a novel piezodriven monolithic flexure-hinge stage,” *Proceedings of IEEE International Conference on Control Applications*, **2**, pp. 977-982, Taipei, Taiwan, September 2004.

[49] Slotine J. J. and Sastry S. S., “Tracking control of non-linear systems using sliding surface with application to robot manipulators,” *International Journal of Control*, **38**, pp. 465-492, 1983.

[50] Sastry S. and Bodson M., Adaptive Control: Stability, Convergence, and Robustness, Englewood Cliffs, NJ, 1989.

[51] Zhou J., Wen C. and Zhang Y., “Adaptive backstepping control of a class of uncertain nonlinear systems with unknown backlash-like hysteresis”, *IEEE Transactions on Control Systems Technology*, **49**, pp. 1751-1757, 2004.

[52] Su C. Y., Stepanenko Y., Svoboda J. and Leung T. P., “Robust adaptive control of a class of nonlinear systems with unknown backlash-like hysteresis”, *IEEE Transactions on Automatic Control*, **45**, pp. 2427-2432, 2000.

[53] Narendra K. S. and Annaswamy A. M., *Stable Adaptive Systems*, Prentice-Hall, Englewood Cliffs, NJ, 2002.

[54] Saeidpourazar R. and Jalili N., “Towards microcantilever-based force sensing and manipulation: modeling, control development and implementation" in print, *International Journal of Robotics Research*, available online (May. 2008).

[55] Bashash S., Saeidpourazar R., and Jalili N., “Tracking control of time-varying discontinuous trajectories with application to probe-based imaging and nanopositioning, submitted to *Control Engineering Practice*, September 2008.

[56] Binnig G. and Rohrer H., “Surface imaging by scanning tunneling microscopy,” *Ultramicroscopy*, **11**, pp. 157-160, 1983.

[57] Julian C. C., “Origin of atomic resolution on metal surfaces in scanning tunneling microscopy,” *Physical Review Letters*, **65**, pp. 448-451, 1990.

[58] Oura K., Lifshits V. G. , Saranin A. A., Zotov A. V. and Katayama M., *Surface science: an introduction*, Springer Verlag, Berlin, 2003.

[59] Image Metrology A/S, http://www.imagemet.com.

[60] The A to Z of Nanotechnology, http://www.azonano.com/.

[61] The UCSF Computer Graphics Laboratory (CGL), http://www.cgl.ucsf.edu/chimera/ImagezGallery/entries/afm/stmv-afm.html.

[62] Bashash S., Vora K., Jalili N., "Distributed-parameters modeling and control of rod-type solid-state actuators," Submitted to *Journal of Vibration and Control*, October 2008.

[63] Mansour T., Konno A., and Uchiyama M., "Modified PID control of a single-link flexible robot", *Advanced Robotics*, **22**, pp. 433-449, 2008

[64] Fen W. and Yildizoglu S. E., "Distributed parameter-dependent modeling and control of flexible structures", *Transactions of the ASME, Journal of Dynamic Systems, Measurement, and Control*, **127**, pp. 230-239, 2005.

[65] Halim D., and Moheimani S. O. R., "Spatial H_2 control of a piezoelectric laminate beam: experimental implementation", *IEEE Transactions on Control Systems Technology*, **10**, pp. 533-546, 2002.

[66] Chyanbin H., Chang W. C., and Gai, H. S., "Vibration suppression of composite sandwich beams", *Journal of Sound and Vibration*, **272**, pp. 1-20, 2004.

[67] Olgac N. and Jalili N., "Modal analysis of flexible beams with delayed resonator vibration absorber: theory and experiments", *Journal of Sound and Vibration*, **218**, pp. 307-331, 1998.

[68] Meirovitch L., *Elements of Vibration Analysis*, 2nd ed., McGraw-Hill, Inc., New York, 1986.

[69] Ogata K., *Modern Control Engineering*, 4th ed., Prentice Hall, New Jersey, 2001.

[70] Matyas J., "Random optimization", *Automation and Remote Control*, **22**, pp. 246-253, 1965.

[71] Utkin V. I., "Variable structure systems with sliding modes," *IEEE Transactions on Automatic Control*, **22**, pp. 212-222, 1977.

[72] Bashash S. and Jalili N., "Robust adaptive control of coupled parallel piezo-flexural nano-positioning stages," *IEEE/ASME Transactions on Mechatronics*, accepted, September 2008.

[73] Salehi-Khojin A., Bashash S., and Jalili N., "Modeling and experimental vibration analysis of nanomechanical cantilever active probes", *Journal of Micromechanics and Microengineering,* **18**, pp. 085008, 2008.

[74] Salehi-Khojin A., Bashash S., Jalili N., and Berger R., "Nanomechanical cantilever Active Probes for ultra small mass detection", *Journal of Applied Physics,* accepted, November 2008.

[75] Jalili N., Dadfarnia M. and Dawson D. M., "A fresh insight in to the microcantilever-sample interaction problem in non-contact atomic force microscopy," *ASME Journal of Dynamic Systems, Measurement, and Control*, **126**, pp. 327-335, 2004.

[76] Nagashima N., Matsuoka S. and Miyahara K., "Nanoscopic hardness measurement by atomic force microscope," *JSME International Journal, Series A*, **39**, pp. 456-462, 1996.

[77] Gahlin R. and Jacobson S., "Novel method to map and quantify wear on a micro-scale," *Wear*, **222**, pp. 93–102, 1998.

[78] Miyahara K., Nagashima N., Ohmura T. and Matsuoka S., "Evaluation of mechanical properties in nanometer scale using AFM-based nanoindentation tester," Nanostructured Materials, **12**, pp. 1049–1052, 1999.

[79] Ziegler C., "Cantilever-based biosensors," *Analytical and Bioanalytical Chemistry*, **379**, pp. 946-959, 2004.

[80] Dareing D. W. and Thundat T., "Simulation of adsorption-induced stress of a microcantilever sensor," Journal of Applied Physics, **97**, 043526, 2005.

[81] McFarland A. W., Poggi M. A., Doyle M. J., Bottomley L. A. and Colton J. S., "Influence of surface stress on the resonance behavior of microcantilevers," *Applied Physics Letters*, **87**, 053505, 2005.

[82] Ren Q. and Zhao Y. P., "Influence of surface stress on frequency of microcantilever-based biosensors," *Microsystem Technologies*, **10**, pp. 307-314, 2004.

[83] Wu G., Ji H., Hansen K., Thundat T., Datar R., Cote R., Hagan M. F., Chakraborty A. K. and Majumdar A., "Origin of nanomechanical cantilever motion generated from biomolecular interactions," *Proceedings of the National Academy of Sciences of the United States of America*, pp. 1560-1564, 2001.

[84] Braun T., Barwich V., Ghatkesar M. K., Bredekamp A. H., Gerber C., Hegner M. and Lang H. P., "Micromechanical mass sensors for biomolecular detection in a physiological environment," *Physicals Review*, **72**, 031907, 2005.

[85] Thundat T., Warmack R. J., Chen G. Y. and Allison D. P., "Thermal and ambient-induced deflections of scanning force microscope cantilevers," *Applied Physics Letters*, **64**, pp. 2894-2898, 1994.

[86] Berger R., Gerber C. and Gimzewski J. K., "Thermal analysis using a micromechanical calorimeter," *Applied Physics Letters*, **69**, pp. 40-42, 1996.

[87] Grigorov A.V., Davis Z. J., Rasmussen P. A. and Boisen A., "A longitudinal thermal actuation principle for mass detection using a resonant microcantilever in a fluid medium," *Microelectronic Engineering*, **73**, 881-886, 2004.

[88] Susuki Y., "Novel microcantilever for scanning thermal imaging microscopy," *Japanese Journal of Applied Physics*, **35**, pp. L352-L354, 1996.

[89] Majumdar A., Lai J., Chandrachood M., Nakabeppu O., Wu Y. and Shi Z., "Thermal imaging by atomic force microscopy using thermocouple cantilever probes," *Review of Scientific Instruments*, **66**, pp. 3584-3592, 1995.

[90] Shi L., Plyasunov S., Bachtold A., McEuen P. L. and Majumdar A., "Scanning thermal microscopy of carbon nanotubes using batch-fabricated probes," *Applied Physics Letters*, **77**, 4295, 2000.

[91] Lee H. C., Park J. H. and Park Y. H., "Development of shunt type ohmic RF MEMS switches actuated by piezoelectric cantilever," *Sensors and Actuators A*, **136**, pp. 282–290, 2007.

[92] Chu C. H., Shih W. P., Chung S. Y., Tsai H. C., Shing T. K. and Chang P. Z., "A low actuation voltage electrostatic actuator for RF MEMS switch applications," *Journal of Micromechanics Microengineering*, **17**, pp. 1649–1656, 2007.

[93] Jalili N. and Laxminarayana K., "A review of atomic force microscopy imaging systems: application to molecular metrology and biological sciences," *Mechatronics*, **14**, pp. 907-945, 2007.

[94] Mahmoodi S. N., Afshari M. and Jalili N., "Nonlinear vibrations of piezoelectric microcantilevers for biologically-induced surface stress sensing," *Communications in Nonlinear Science and Numerical Simulation*, **13**, pp 1964-1977, 2008.

[95] Afshari M. and Jalili N, "Towards non-linear modeling of molecular interactions arising from adsorbed biological species on the microcantilever surface," *International Journal of Non-linear Mechanics*, **42**, pp. 588-595, 2007.

[96] Manalis S. R., Minne S. C. and Quate C. F., "Atomic force microscopy for high speed imaging using cantilever with an integrated actuator and sensor," *Applied Physics Letters*, **68**, 871, 1996.

[97] Adams J. D., Rogers B., Manning L., Hu Z., Thandat T., Cavazos H. and Minne S. C., "Piezoelectric self-sensing of adsorption-induced microcantilever bending," *Sensors and Actuators A*, **121**, pp. 457-461, 2005.

[98] Adams J. D., Parrott G., Bauer C., Sant T., Manning L., Jones M. and Rogers B., "Nanowatt chemical vapor detection with a self-sensing, piezoelectric microcantilever array," *Applied Physics Letters*, **83**, 3428, 2003.

[99] Dosch J. J., Inman D. J. and Garcia E., "A self-sensing piezoelectric actuator for collocated control," *Journal of Intelligent Material Systems and Structures*, **3**, pp. 166-185, 1992.

[100] Volkert, C. A. and Minor A. M., "Focused Ion Beam Microscopy and Micromachining", *MRS Bulletin*, **32**, pp. 389, 2007.

[101] Bashash S., Salehi-Khojin A. and Jalili N., "Dynamic modeling of Euler-Bernoulli beams with multiple cross-sectional discontinuities under arbitrary distributed loading", Submitted to *International Journal of Mechanical Sciences,* November 2008.

Major publications resulted from this dissertation:

1- Bashash S., Salehi-Khojin A. and Jalili N., "Dynamic modeling of Euler-Bernoulli beams with multiple cross-sectional discontinuities under arbitrary distributed loading", Submitted to *International Journal of Mechanical Sciences,* November 2008.

2- Bashash S., Vora K. and Jalili N., "Distributed-parameters modeling and control of rod-type solid-state actuators," Submitted to *Journal of Vibration and Control*, October 2008.

3- Bashash S., Saeidpourazar R. and Jalili N., "Tracking control of time-varying discontinuous trajectories with application to probe-based imaging and nanopositioning, submitted to *Control Engineering Practice*, September 2008.

4- Salehi-Khojin A., Bashash S., Jalili N., and Berger R., "Nanomechanical cantilever Active Probes for ultra small mass detection", *Journal of Applied Physics,* accepted, November 2008.

5- Bashash S. and Jalili N., "Robust adaptive control of coupled parallel piezo-flexural nano-positioning stages," *IEEE/ASME Transactions on Mechatronics*, accepted, September 2008.

6- Salehi-Khojin A., Bashash S., and Jalili N., "Modeling and experimental vibration analysis of nanomechanical cantilever active probes", *Journal of Micromechanics and Microengineering,* **18**, pp. 085008, 2008.

7- Bashash S. and Jalili N., "A polynomial-based linear mapping strategy for compensation of hysteresis in piezoelectric actuators," *ASME Transactions, Journal of Dynamic Systems, Measurements and Control*, **130**, pp. 031008 (1-10), 2008.

8- Bashash S. and Jalili N., "Robust multiple-frequency trajectory tracking control of piezoelectrically-driven micro/nano positioning systems," *IEEE Transactions on Control Systems Technology*, **15**, pp. 867-878, 2007.

9- Bashash S. and Jalili N., "Intelligent rules of hysteresis in feedforward trajectory control of piezoelectrically-driven nanostagers," *Journal of Micromechanics and Microengineering*, **17,** pp. 342-349, 2007.

10- Bashash S. and Jalili N., "Underlying memory-dominant nature of hysteresis in piezoelectric materials," *Journal of Applied Physics,* **100**, pp. 014103, 2006.